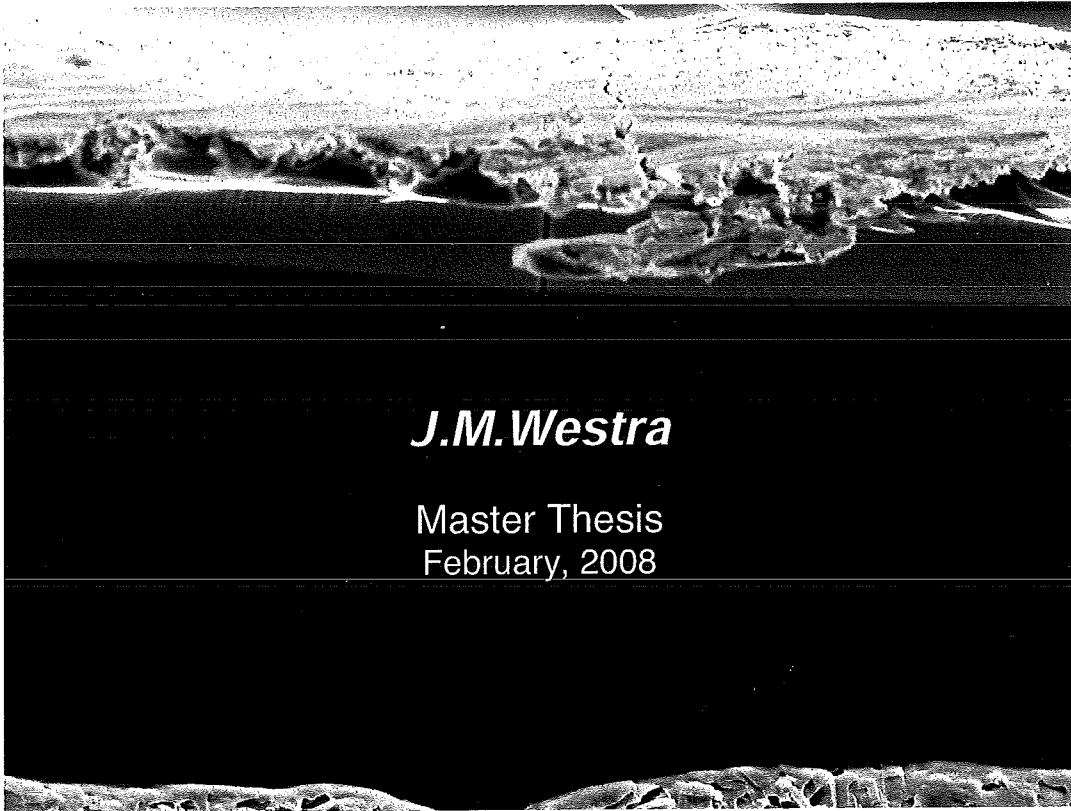


# Joining and mechanical behaviour of poly-crystalline silicon solar cells



**Delft University of Technology**  
Materials Science and Engineering  
Joining and Mechanical Behaviour  
Supervisors: Michael Janssen  
Ian Richardson



**Energy research Centre of the Netherlands**  
Solar Energy  
PV Module Technology  
Supervisor: Ian Bennett





# Preface

## Timeline of solar cells<sup>1</sup> and ECN

The concept of using sunlight to generate electricity goes back two centuries, to 1839 when French physicist Antoine-Cesar Becquerel observed that shining light on an electrode submerged in a conductive solution would create an electric current.

Millikan proved photoelectric effect experimentally in 1916. Albert Einstein received the Nobel Prize for explaining this effect in 1923.

In 1941, the American Russell Ohl invented a silicon solar cell, with an energy conversion efficiency below one percent. This changed when Pearson, Fuller and Chapin designed a silicon solar cell capable of a six percent energy conversion efficiency with direct sunlight in 1954.

The expensive solar power found its first applications in space. The first PV-powered satellite, Vanguard I, was launched in 1958. The satellite power system operated for 8 years. Hoffman Electronics started producing, 10% efficient, commercially PV cells. This started the use of solar cells outside of space application.

ECN started in 1955 with as a research centre for nuclear power. From around 1975 the research field of ECN was expanded to include wind turbines, solar power, and biomass energy. ECN is currently one of the major international players in solar cell research.

## Materials in solar cells

According to Goetzberger and Hebling<sup>2</sup> the most important material used in solar cells was and still is silicon. Crystalline silicon had a market share of 86% in 2000, which was almost equally distributed between single crystal and cast silicon. Amorphous silicon had another 13%. Although research into other materials, such as polymers is increasing, the production lines are still mainly concerned with silicon solar cells.

The source of highly purified silicon for solar cells, is somewhat uncertain. The cost of a solar cell is determined by the cost of processed silicon wafers for about 50%. In the past, reject material from the semiconductor industry, was available at low cost. This created a dependence that is only viable if both sectors grow at the same rate. Unfortunately the semiconductor market is characterized by violent cycles of boom and depression superimposed on a relatively steep growth curve. In 1998 such a boom caused even reject material to be in short supply and solar cell manufacturers were forced to buy regular semiconductor grade material at relatively high cost.<sup>3</sup>

One of the keys for cost reduction is to reduce the silicon content of the product. Present lines of approach are reduction of kerf loss by wire sawing and use of thinner wafers. The most advanced production lines use wafers of less than 0.2 mm thickness. This development is not without difficulties, and it is those difficulties that started this project.

## Abstract

The most advanced production lines for H-pattern poly-crystalline solar cells use wafers of less than 200 micron thickness. The reason for this development is the cost reduction that can be achieved by reducing the amount of silicon required. Unfortunately, the cells produced from thinner wafers suffer from bowing.

The extent of bowing and the delicacy of the cells are problems for the building of modules from cells thinner than 200 micron. In this report the origin and extent of bowing is examined for wafers and cells of different thicknesses, by analysis at several stages in the production cycle.

Not only the production of the cells is taken into account. A functioning solar panel requires cells that will have a good performance for 20 years. To realise such long lifetimes, the damage induced by the production process should be minimal. In several steps of the production, stress and possible damage is introduced. The presence of surface cracks at several stages was examined by microscopy for this purpose. The presence of microcracks in soldered solar cells was studied using acoustic emission monitoring. Four point bending experiments of cells taken from different stages of the production process were also monitored by acoustic emission.

Surface cracks have not been observed and the presence of microcracks after soldering could not be confirmed in this research, although acoustic emission measurements imply the possibility of their propagation or initiation during soldering. Losses in the production process did not occur during the soldering of the cells, but in production steps preceding soldering. The research shows that the bowing is caused primarily by the addition and more specifically the thermal contraction of the aluminium underside of the solar cells. Bowing increases as the thickness of the cell decreases and the experimental fracture strength of the cells and wafers reduces as the thickness reduces. The weakest area of the solar cells appears to be the transition between aluminium and silver on the rear of the cell.

This work reports on a preliminary research study, which will be followed-up by a more detailed graduate study. ECN is currently working on poly-crystalline cells with an open underside. These cells, even thinner ones, should have a higher fracture stress, than those with an aluminium layer.

# Contents

Preface	1
Timeline of solar cells and ECN	1
Materials in solar cells	1
Abstract	2
Contents	3
Vocabulary	5
<i>Chapter 1</i> Introduction	6
1.1 What makes a solar cell, solar cell principles	7
1.2 Solar cell construction: cell, module and panel	8
1.2.1 <i>H-pattern cell</i>	9
1.2.2 <i>Modules</i>	10
1.3 Producing the layered structure, processing steps	11
1.4 Soldering process	16
<i>Chapter 2</i> Formulation of problem and approach	18
2.1 Research strategy	18
2.1.1 <i>Samples</i>	18
2.1.2 <i>Composition and dimensions of Al-Si layer</i>	19
2.2 Research questions	22
2.3 Potential methods of stress measurements	22
2.3.1 <i>Stress measurements</i>	22
2.3.2 <i>X-ray diffraction</i>	23
2.3.3 <i>Raman spectroscopy</i>	26
2.3.4 <i>Conclusions on stress measurement methods</i>	27
<i>Chapter 3</i> Theory concerning stresses induced by processing steps	28
3.1 Material properties and dimensions	28
3.1.1 <i>Porosity</i>	29
3.2 Thermal stress calculations	30
3.3 Modelling	33
<i>Chapter 4</i> Experiments concerning stresses induced by processing steps	36
4.1 Curvature measurements	36
4.2 Modelling bowing and thermal stress	36
4.3 Local heat input influence	38
<i>Chapter 5</i> Results concerning stresses induced by processing steps	39
5.1 Curvatures	39
5.2 Calculations of properties	41
5.3 Calculations of thermal stress	42
5.4 Modelling	44
5.5 Discussion	46
<i>Chapter 6</i> Theory concerning fracture	48
6.1 Introduction	48

6.2	Fracture mechanics	48
6.2.1	<i>Griffith and Irwin</i>	49
6.3	Surface roughness	50
6.3.1	<i>Measurements</i>	51
6.3.2	<i>Results</i>	51
6.4	Acoustic emission	53
6.5	Brittle fracture, cleavage and fracture surfaces	54
 <i>Chapter 7</i> Experiments concerning fracture		 55
7.1	Four point bending	55
7.2	Acoustic emission	57
7.2.1	<i>Four point bending</i>	57
7.2.2	<i>Soldering</i>	58
 Chapter 8 Results concerning fracture		 59
8.1	Four point bending	59
8.2	Acoustic emission	66
8.2.1	<i>Four point bending</i>	66
8.2.2	<i>Soldering</i>	66
8.3	Fractures	67
8.4	Discussion	72
 <i>Chapter 9</i> Discussion and conclusions		 75
9.1	Discussion	75
9.1.1	<i>Soldering &amp; cells</i>	75
9.1.2	<i>Influence of metallisation and other process steps</i>	76
9.2	Conclusions	77
9.3	Recommendations	78
 Acknowledgments		 79
 References		 80
 Appendix I		 83

## Vocabulary

2D	Two dimensional
3D	Three dimensional
$\alpha$	Thermal expansion coefficient
$\epsilon$	Strain (no units)
$\nu$	Poisson's ratio (no units)
$\sigma$	Stress, units for stress are stated in the text, mostly MPa
$\rho$	Density kg/m <sup>3</sup>
AE	Acoustic Emission
Al-Si	Alloy of Aluminium and Silicon
BSF	Back Surface Field
cell	See: Solar cell
EBSD	Electron Backscatter Diffraction, measuring technique
EDS	Energy Dispersive Spectroscopy
Electron	Elementary particle
encapsulant	Material that is used to embed an object or structure
GS Improve BV	Glass Service, Inc. is a Czech based consulting company in the field of glass melting, conditioning and forming.
H-pattern	Silver pattern on the front of a solar cell, that collects electrons
hole	Negative electron or a vacancy in an energy band in which an electron should be present
metallisation	All metal attached to the solar cell to collect electrons
module	Built-up of solar cells, which protects the cells from external influences such as rain
mono-crystalline	Material structure that consists of only one crystal
multi crystalline	See: poly-crystalline
multi layer	Arrangement of more than one layers
poly-crystalline	Material structure that consists of more than one crystal
ppba	Parts per billion atomic relative to silicon
ppma	Parts per million atomic relative to silicon
Raman Spectroscopy	A measuring technique, measures (anti-) Stokes-Raman scattering
recombination	Elimination of an electron and a hole that occurs when these unite
SEM	Scanning Electron Microscopy
solar cell	Device to convert light into current, used in most of the text to indicate the poly-crystalline H-pattern solar cell.
soldering	Process to connect two materials by a solder substance
string	Collection of solar cells, connected by tabs
tab	Tin plated copper ribbon, used to set solar cells in series and transport the current from these solar cells.
WDS	Wavelength Dispersive Spectroscopy
XRD	X-Ray Diffraction

## **Chapter 1 Introduction**

This work is a contribution to an ongoing investigation concerning the electrical connections and durability of solar cells. The complete investigation is focussed on the material behaviour that occurs at the joining of electrical connections and is designed to assess the influence of the joining and other manufacturing processes on the long-term viability of silicon-wafer-based solar cells. This investigation has been initiated to reduce failure rates during manufacturing and to increase cell lifetimes.

The focus of this contribution is on reviewing existing knowledge and exploring the first steps of a complete investigation. The first steps include an examination of the cell surfaces by light and electron microscopy, evaluation of the cells under mechanical load and preliminary measurements of stresses in the cell. In addition some thermal-mechanical models assist the investigations.

The problem that was identified by the module-manufacturing department is concerned with deformation present in the strings of soldered cells. With decreasing wafer thickness this problem was found to become more severe, and is based on the deformation observed in the cells before the soldering process.

The main issue is the possible breakage of cells during the production of strings of cells. If one cell in the string is defective, the whole string is affected, resulting in relatively large financial losses.

Relevant questions are:

- In what condition do the cells arrive at the connection step?
  - What process steps precede the electrical connections step?
  - What stresses are present in the materials?
  - Are (surface) cracks present in the materials?
  - What roughness has the surface obtained?
- Which cells survive the soldering process?
- What are the differences between cells that survive the soldering process and those that do not?
- What is the minimum thickness required for the production method?

This work reports on a preliminary research study, which will be followed-up by a more detailed graduate study. The present research consists of many different aspects; for this reason, the structure of this report deviates somewhat from a normal masters thesis. The structure of this report attempts to present different research directions in a comprehensible order.

The introduction, chapter 1, introduces the main research interests and briefly describes solar cell principles. The construction and production of solar panels, modules and cells is presented. These sections include descriptions of the layers in a

solar cell from previous investigation. The introduction concludes with the soldering process that connects the solar cells.

A more detailed discussion of the research questions and strategy can be found in chapter 2. The dimensions and composition of the samples used during this research are presented before refining the research question. Possible techniques for stress measurements are evaluated in the second part of chapter 2.

Chapters 3 through 5 concern the effect of process steps on the stresses in the solar cells. The mechanical properties are introduced in chapter 3. This chapter continues with a description of the theory behind thermal stress calculations and modelling. Chapter 4 describes the experimental techniques used to measure the curvature of the cells. The modelling work is also introduced. The results from the calculations and experiments and modelling work are presented and discussed in chapter 5.

Chapters 6 through 8 discuss the behaviour of fracture. The basics of fracture mechanics are presented in Chapter 6 followed by the measurements of the surface roughness, which provide important data on initial crack size. The theory of acoustic emission and fracture surfaces conclude chapter 6. Chapter 7 describes the experimental arrangements used to solder the samples and to fracture the samples. The results of these experiments and the analysis of the fracture samples by microscope are presented in Chapter 8.

A general discussion is given in chapter 9 with reference to the research questions outlined in chapter 2. Conclusions are presented based on this work and recommendations are made for future consideration.

## 1.1 What makes a solar cell, solar cell principles

A solar cell is a device used to turn light into electricity. Only a few materials are suitable for such a device, they are referred to as photovoltaic materials. Photovoltaic materials are semiconductors, which means that the degree to which they conduct electrons can vary. Conduction is possible when electrons are free to move around in the atomic lattice. When an electron leaves its atom, it leaves a hole behind. A hole can simply be seen as the absence of the electron. A hole can also be seen as a new “particle” with the opposite of the charge of the electron (so a positive charge). The band gap of a semiconductor is the minimum energy required to move an electron from its bound state to a free state where it can participate in conduction.

To generate a current in such a material the free electrons must move away from the holes, this is achieved by joining semiconductors with different properties. *P-n* junctions are formed by joining *n*-type and *p*-type semiconductor materials. The *n*-type region has a high electron concentration and the *p*-type a high hole concentration. Electrons diffuse from the *n*-type side to the *p*-type side. When the electron meets up with a hole they will unite and cancel out their charge. Solymar and Walsh<sup>4</sup> describe this as soldiers going to war, when they meet up, they kill each other. This phenomenon is called recombination. If the recombination rate is equal to the rate at which holes are created by the incoming light, no current can be extracted from the material.

The diffusion of charge which is established across the  $p$ - $n$  junction, creates a diode that promotes current to flow in only one direction across the junction. Electrons may pass from the  $n$ -type side into the  $p$ -type side, and holes may pass from the  $p$ -type side to the  $n$ -type side. This region where electrons have diffused across the junction is called the depletion region because it no longer contains any mobile charge carriers. It is also known as the "space charge region".



Figure 1. Solar panels in the roofing of a greenhouse in Hoofddorp.

Silicon is the semiconductor used most often in solar cells. Solar applications require the material to be able to convert light into electricity and preferable be inexpensive and abundant in the world. Unfortunately the current requirements for silicon include a purity that keeps the recombination sites in the wafers low. This purity of silicon is defined as solar grade silicon. Solar grade silicon has less impurities than semiconductor grade. Silicon has the benefit that it is used in other semiconductor industries and is therefore available in fairly high purity compared to other photovoltaic materials, such as cadmium telluride and gallium arsenide. Solar grade silicon can be produced from semiconductor grade silicon by a chemical processing route. All impurities are reduced to below the 1 ppba level by this process.<sup>5</sup> Most solar cells require silicon with about 0.5 ppma boron. The interstitial oxygen and substitutional carbon concentrations should be below 10 ppma.

## 1.2 Solar cell construction: cell, module and panel

A solar panel is a power supplying device that is often placed on buildings or in green fields; figure 1 shows panels on the roofing of a greenhouse. This panel is built up of several components, some of which will be discussed here.

### 1.2.1 H-pattern cell

The smallest building block in the world of photovoltaic devices is the solar cell, shown in figure 2. In this case an H-pattern cell is considered, of 156 by 156 mm<sup>2</sup>. A series of cells is a solar panel or module. A common configuration of a module is 6 by 10 cells together.

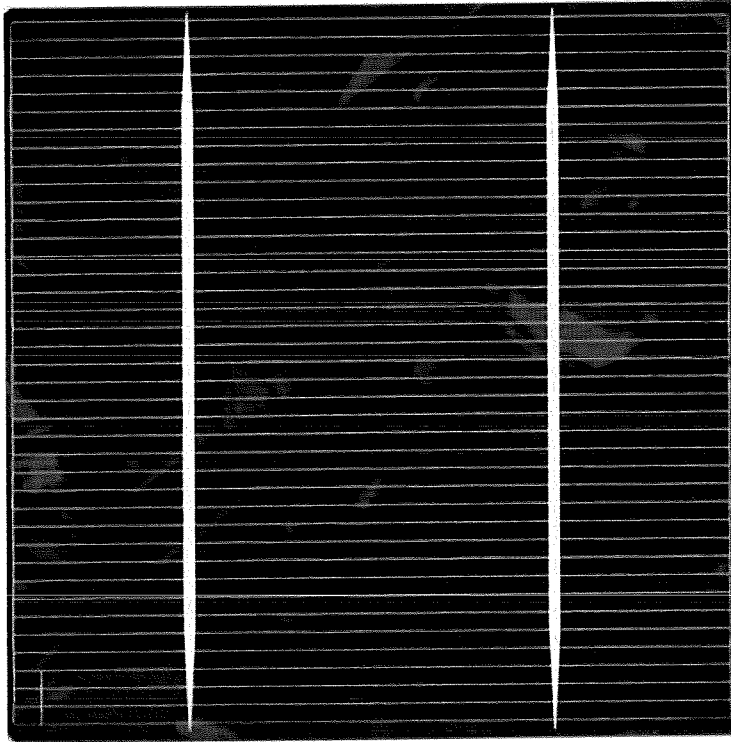


Figure 2. Top view of poly-crystalline silicon H-pattern cell. The vertical silver lines are called busbars, the horizontal lines are called fingers.

Within these criteria several types of silicon can be used for solar cells. Single crystal silicon gives the best results; unfortunately this is also expensive to produce. In H-pattern cells poly-crystalline silicon (doped with boron, p doped) is used. This material is produced by filling a crucible with solar grade silicon; this is heated and cooled at such a slow rate that large crystals are formed. The ingot is cut into smaller bricks that are cut into wafers (slices) of 200 to 300 microns. The surface properties of the cut wafers are not ideal. The condition of the surface determines the mechanical and light adsorbing properties of the wafer. For light adsorption surface texture is required. From a mechanical point of view, surface damage will result in weakening of the wafer. Reduction of surface damage and texturisation is achieved by the same etching process. The roughening of the surface is done by the same etching. In reports of ECN, this etching method is referred to as industrial etch T1.<sup>6</sup> The upper surface of the wafer is doped by diffusing a phosphorous *n*-type layer of a few hundred nanometres thickness. This layer is the emitter. The surface of the wafer is covered by an anti-reflective layer, this gives the wafer its blue colour, as is shown in figure 2.

The bottom surface is boron doped, this is the base of the  $p$ - $n$  junction. The bottom is covered by the back contact: an aluminium layer of about 40 microns<sup>7 a</sup> is applied by screen printing. In screen printing paste is pressed through a screen onto the wafer. A detail of this layer is shown in figure 3. A silver paste is screen printed on the front to form a contact.

The shape of the silver is visible in figure 2.: the “fingers” are the small horizontal lines and the “busbars” are the two broader vertical lines. After the printing process, the front and back contacts are fired to 900 °C, to make a solid electrical and mechanical connection. The back contact not only functions as a current collector, it also dopes the silicon to make a heavily doped layer ( $p^+$ ), which is called the back surface field (BSF). This causes the electrons to accelerate into the aluminium contact layer.

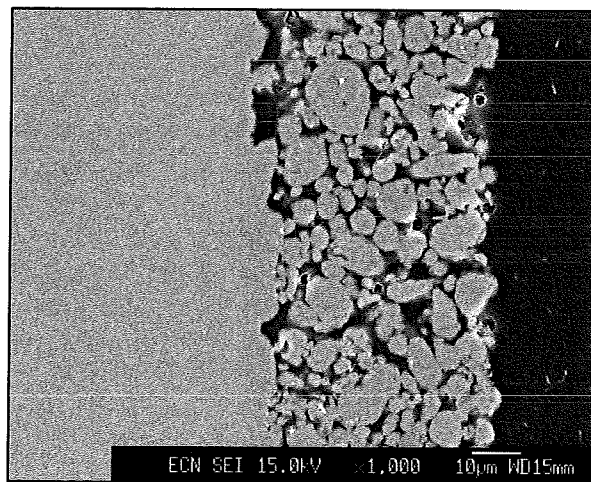


Figure 3. Secondary electron image of a cross section of the aluminium back layer. The light grey is silicon and the porous layer is aluminium.

### 1.2.2 Modules

The solar modules are made up of a series of solar cells, a minimum commercial configuration is 9 by 4 cells. Industry is currently looking at larger modules, generally up to 6 by 10 or 6 by 12 cells. The cells are connected to each other by tabs (tin plated copper) that are attached to the front of one cell and then to the back of the next. To prevent tension in the outer edge of the silicon wafer a stress-relief mechanism is built into the strings of cells. This system can be seen in figure 4. The cells are joined by soldering. This soldering introduces a thermal tension into the layered structure. In some cases this tension can lead to fracture of the wafer. Some alternatives for soldering are conducting adhesives and laser welding of the tabs to the cell.<sup>8</sup> These techniques are currently being examined by ECN. For future research these techniques should be included in the research.

<sup>a</sup> For aluminium from 3 baseline samples, the average thickness is 41,5 +/- 1,1 microns.<sup>3</sup>

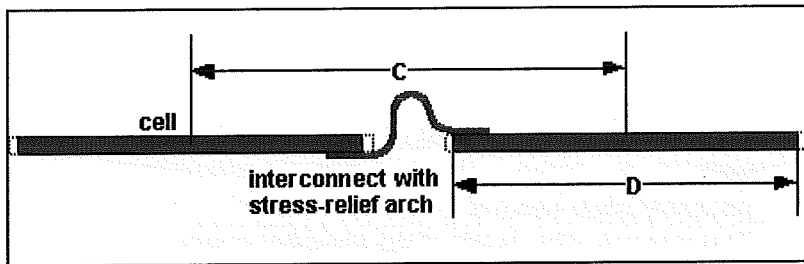


Figure 4. Example of a stress-relief arch between H-cells in solar modules.

In figure 5 the construction of a module is displayed. The top is made of a glass sheet (low Fe glass). A layer of EVA (ethylene vinyl acetate) is applied to the bottom and top as an encapsulant (polymerized at 150°C); it is stable at elevated temperatures and under UV exposure. The bottom plate, often made of Tedlar (a vinyl fluoride polymer manufactured by Dupont<sup>9</sup>), must prevent the ingress of water and water vapour and is required to have high thermal conductivity, like the encapsulant. The high thermal conductivity is needed to prevent damage caused by local heating of the module.<sup>10</sup>

### 1.3 Producing the layered structure, processing steps

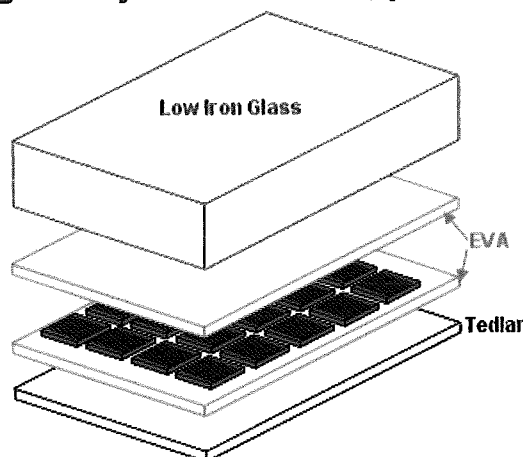


Figure 5. The construction of a solar module, including 4 x 5 solar cells.

In the previous sections the structure of solar cells was introduced. In this section a more complete list of the processing steps will be described, with a small explanation.

The process used to produce solar cells can be divided into several steps:

1. *cutting of poly-crystalline silicon wafers*  
Wafers are cut from ingots of silicon using a diamond-coated wire. In this step the thickness of the wafers is determined. The surfaces of these wafers are rough due to the sawing process.
2. *saw damage removal*  
This step, also known as the ECN-clean, removes the damage of the previous step and leaves a texture on the surface that increases the absorption of light.

3. *phosphor source application*  
This provides the phosphor for diffusion.
4. *phosphor diffusion*  
By diffusion an *n*-type semiconductor layer is created on the top of the wafer.
5. *phosphor glass removal*  
This removes what is left of the phosphor source.
6. *silicon nitride (SiNx:H) deposition*  
In a PECVD (plasma enhanced chemical vapour deposition) process a blue anti-reflective layer is created.
7. *metallisation*  
Silver paste is applied on top of the silicon nitride layer by screen printing, the screen has a negative H-pattern through which the silver paste is pressed. The cell is then dried by infrared lamps, for at least 10 seconds. For connection purposes silver spots are printed on the back. The rear side aluminium paste is deposited in the same way as the silver, but using a different screen, which leaves openings around the silver spots. After printing, the cells are dried again.
8. *firing of metallisation*  
The firing consists of two parts, the burn-out and the peak firing. The burn out is done to remove the organic materials in the metal paste and to sinter the deposited metal so that it makes good contact with the silicon. During the firing peak the back surface field is formed at the back of the cell. (see figure 6)
9. *edge isolation*  
This is done to prevent a short circuit in the device.

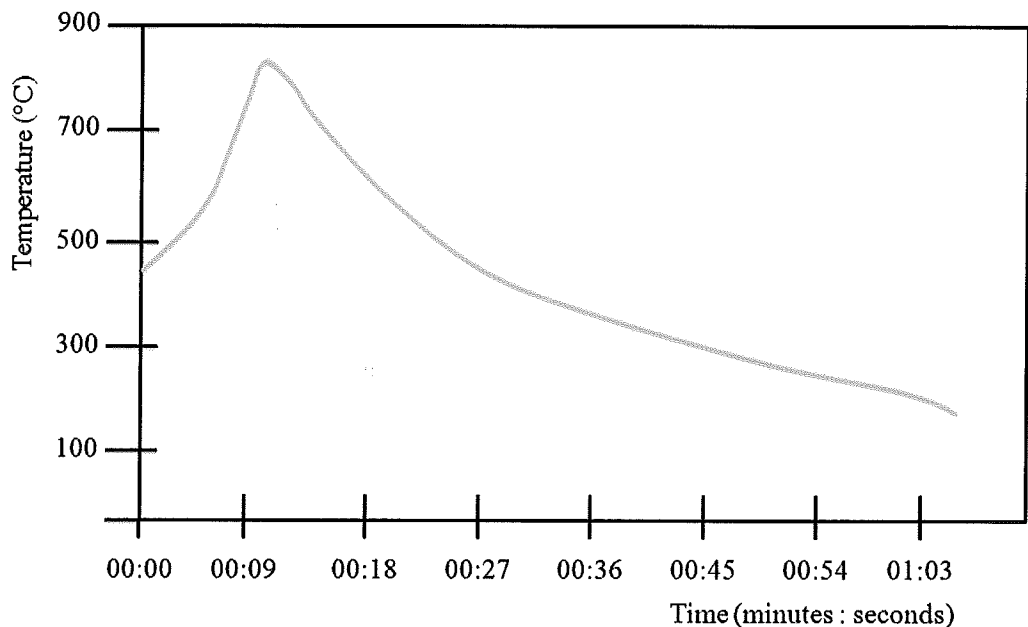


Figure 6. Cell temperature profile for the firing peak, the graph is based on oven measurements for cells made in 2004.<sup>11</sup>

During the production process, the silicon will be subjected to treatments like heating and etching. These are treatments that are likely to influence the internal stress in the silicon. Thermal steps above 100 °C will be discussed further<sup>11</sup> because these could have a large influence. The numbers used below are related to those on the previous page. They indicate in which process step the described treatment is used.

3. NaOH boiling at 120 °C for 1 minute (removes approximately 26 microns of silicon).
4. Phosphor is diffused into the silicon using an infrared lamp heated belt furnace, giving a heating rate of 12,8 °C/s up to 890 °C. The dwell time at 890 °C is 6,5 minutes after which the wafer is cooled at 5 °C/s from 890 to 300 °C and approximately 1 °C/s below 300 °C.
6. The silicon nitride deposition onto the wafer is performed at 375 °C. This temperature is needed for a period of 8 to 19 milliseconds.
7. The pressure of the print screening process is dependent on the force exerted by the press (ECN average is 50 N for the H-pattern cells).
8. The temperature profile for the firing of the *metallisation* consists of two parts. The burn-out profile (for removal of the organics) has a ramp up of at least 60 °C/s to a temperature of 400 °C where it is held constant for 30 seconds. From 400 °C the temperature increases again at more than 60 °C/s to the firing peak temperature with a maximum between 800 and 950 °C. The dwell time above 800 °C is between 5 and 10 seconds. After the firing peak the temperature ramps down at 30 °C/s or more, to 400 °C. Details of the firing profile can be seen in figure 6.<sup>11</sup> Below 400 °C, the cells are left to cool down.

The metallisation step is of great importance. It is the largest temperature step that involves the (permanent) connection of layers to the silicon. The application and thermo-mechanical behaviour of Ag and Al could have a significant effect on the stresses in the silicon substrate.

The temperature profile shown in figure 6 has to be considered as an estimate. The location and type of thermocouple used is important in measuring any temperature profile. When the measured object is much thinner than the measuring device, the values measured reveal the heating of the measuring device rather than the object of interest. Also the location of the thermocouple can be important if the heating is not homogeneous. These measurements were done with rather small thermocouples, unfortunately the wafers are also very thin, so the values might not be completely accurate.<sup>12</sup> It is interesting to note that although the melting temperature of silicon is much higher, approximately 1414 °C,<sup>13</sup> there is a change in the mechanical behaviour at elevated temperatures from brittle to ductile. For *p*-type silicon this change occurs around 700 °C and for *n*-type around 650 °C.<sup>14</sup>

The melting temperature of silver is 962 °C (which is lowered by alloying), this means that the process temperature is very close to the melting temperature. Silver is applied as a paste (Ferro 33-212) to form the contacts on the front of the wafer. The organic binding agents are burned out and the metal is sintered (screen printed and fired) onto the silicon, which leaves a porous structure. Line-scans have been made by ECN,<sup>b</sup> in which the compositions of several points on a straight line are measured. The results

---

<sup>b</sup> The measurements, which are part of the crystal clear project, were acquired in November 2005.

are shown in figure 7, the porosity is visible, but there are no signs of alloying between the silicon and silver.

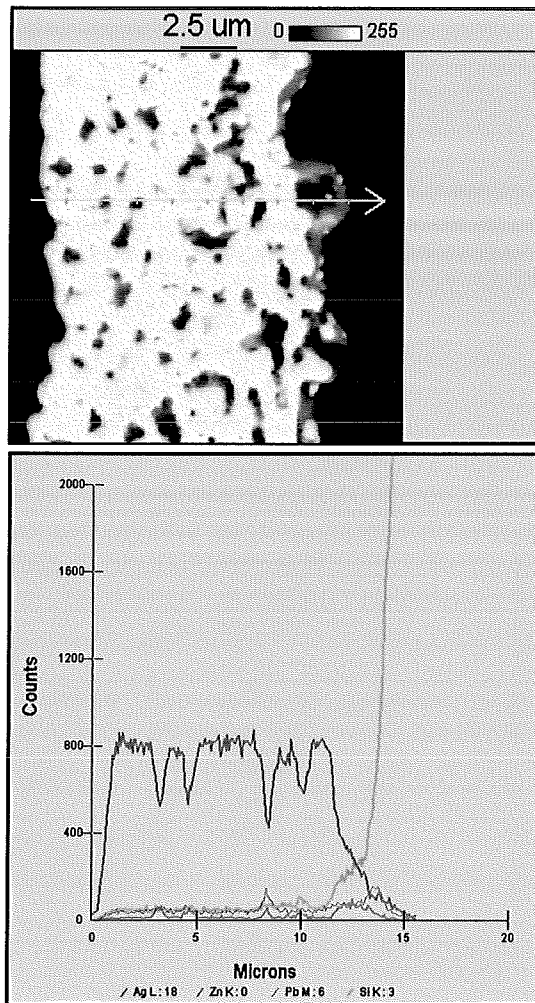


Figure 7. a) SEM picture of a cross section of a silver busbar, on a 200 micron cell and b) an EDS scan showing the composition qualitatively.

The back contact of the cell is made of aluminium (Ferro 53-086) with electrical contact areas of silver. The aluminium has a melting temperature of approximately 660 °C. The paste should melt completely during metallisation and is likely to alloy with the silicon. ECN has measurements of this layer, which is shown in figure 8. In the SEM pictures, figures 3 and 8, this alloy can be seen as a slightly darker grey than the silicon, and there is considerable porosity in the aluminium layer. No in-depth research into this phenomenon has been done, but theories have been made, one of which suggests that the oxide layer, present around the aluminium particles in the paste, is responsible for the porosity of the aluminium layer. Figure 8 is similar to figure 7, a SEM picture and EDS scan have been made of the Al and Al-Si. Unlike the silver tabs, there is a strong gradient of Al in the outside of the silicon layer. In the aluminium quite a few silicon peaks can be observed in the measurement.

Schneider *et al.*<sup>15</sup> have also observed this alloy and considered different paste compositions to reduce the bowing of a cell due to rear metallisation. Huster<sup>16</sup> attempted to make a model to predict the bowing behaviour of solar cells. In this model the assumption was made that the SiAl alloy is homogeneous and the eutectic composition (aluminium + 12 at% silicon), referred to as Al-Si. The BSF is considered to be silicon, doped with 0.1 % Al but it is not included in the mechanical model. In this assumption, the composition gradient of Al and silicon is neglected, which might not be sensible. Al-alloys with a higher than 12 at% content of silicon are not used industrially because these alloys have a strongly reduced strength, which is presumably caused by the precipitation of primary silicon.<sup>17</sup> To make the model predict reality better, a lower Young's modulus has to be assumed, which suggests that the model might be inadequate for the prediction of bowing. This could be due to an oversimplification of the Al-Si alloy, but also to the neglecting of compression of the silicon due to thermal contraction of the aluminium and silver layers. Although it was not stated in the text, the photographs suggest that the silver front pattern was also printed, but it was not taken into account in the model.

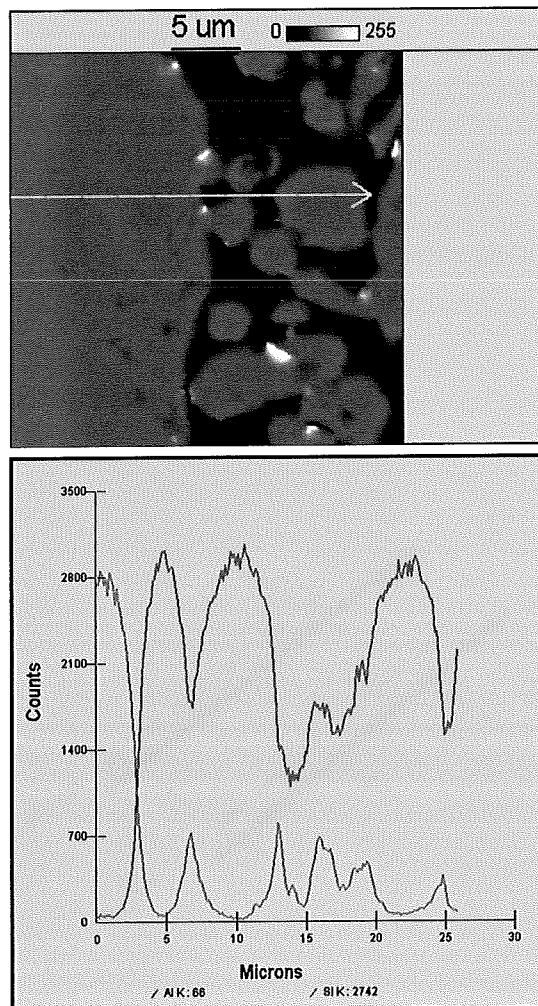


Figure 8. a) SEM picture of a cross section of the aluminium backside on a 200 micron cell and b) an EDS line scan showing the composition qualitatively.

## 1.4 Soldering process

Soldering is an established interconnection technique. Traditionally the solder is heated until it melts and by capillary effects it is drawn between the materials that should be connected. In this case the copper tabs are first coated with a tin solder. The solder is heated from the top of the tab to the bottom through the tin solder and the copper tab.

The soldering process consists of seven solder points per tab. At ECN, soldering is a manual process, but several tools are available for semi-automatic soldering. Each cell in a module is soldered one point at a time. The strings that result from this process are brought together in a module.

In industry, the only connections made by hand, are those that connect the strings to the entire module. The solder process is as follows. First the solder tip presses down on the tab and cell. The tip heats up to 320 °C, cools down and is lifted from the tab. Per tab seven equally spaced connections are made. The tabs are connected in a specific order: first the back contacts are made, then the front contacts, as shown in figure 9. During the soldering process, the heat is applied by a soldering iron and therefore the cell is not only subject to the heat input, but also to a pressure due to the heating element. The pressure of this method varies greatly, but is expected to be in the same range as for a soldering machine. The pressure applied by an industrial machine is in the order of 2 MPa. The machine gives a force of 9.33 N and the solder tip has diameter of 2.5 mm.

The consecutive steps in soldering are: place the first tab on the under side, the second tab on the under side, the first tab on the front side (opposite to the first tab on the rear) and the second tab on the front side. All tabs are soldered at seven points, these seven points are derived from the number of contacts required for electronic conduction, applying an additional safety factor.<sup>c</sup>

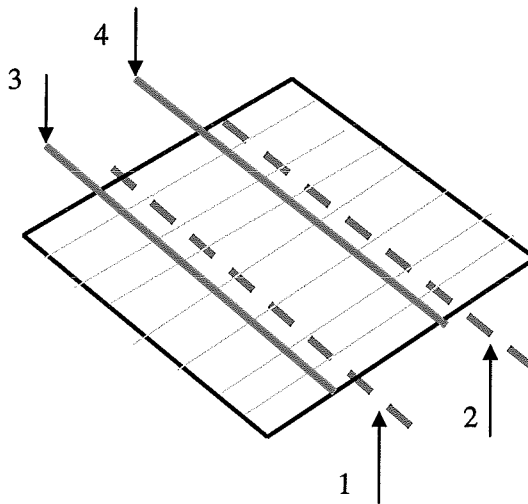


Figure 9. Representation of soldering of the tabs (indicated by red and blue), the order of connection of tabs is 1,2,3,4.

<sup>c</sup> Within ECN this factor is based on agreements between the soldering personnel and the module makers.

First observations suggest that the soldering of the cells does not (greatly) increase its deformation. The deformation is already present before the interconnection processes play any part.

## Chapter 2 Formulation of problem and approach

### 2.1 Research strategy

The stresses present in the material might be fatal for the cells or wafers. The alternative occurs if the layers add strength. Of course the different process steps themselves could be the cause of localised stress peaks. Because of the many process steps preceding the soldering process, certain steps will be isolated to examine the stress distribution and the influence of those particular steps on the mechanical behaviour. The selection of relevant steps is a choice based on the thermal input and alteration of surface properties induced by those steps.

#### 2.1.1 Samples

In order to evaluate the effect of the different process steps for wafers with different thicknesses, wafers entered the production process with thicknesses of: 120, 160 and 200  $\mu\text{m}$ . These cells came from different producers, PV silicon, Scanwafer and Pillar, respectively.

The wafers were selected from a single block, which was cut from the ingot. Due to the casting structure, properties of the wafers vary over the cast ingot. By selecting one block only, the properties can be assumed equal for the wafers. The local cast-structure can be of importance for the behaviour, which is why neighbouring wafers are used to compare the effect of the process steps. The wafers are taken out after the following process steps (for details, please see step description, section 1.3):

- 2 Saw-damage etch (roughness etch)
- 3-5 Emitter completion
- 6 Deposition of anti-reflective coating
- 7-8 Printing, firing

Firing is performed at 900°C. At this temperature the properties of the silicon, aluminium and silver are different from those at room temperature. The aluminium is above its melting temperature which is 660 °C. Silver is around its melting temperature, 962°C for pure silver. Silicon has a melting temperature of approximately 1414 °C,<sup>13</sup> so it is still stable at 900 °C. At high temperatures the normally brittle behaviour of silicon becomes ductile. This DBTT, ductile brittle transition temperature, is around 625 °C for *n*-type silicon (and 645 °C for *p*-type). This means that the development of stresses in the cell during the firing process is complex, even when ignoring the alloying aspects of this process. So far ECN has no experimental data on the differences between fracture of *n*-type versus *p*-type material, nor any data beyond the step of acid etching.

The production steps took place successfully until the printing step. Unfortunately this failed, leaving only useful samples from the following process steps: saw-damage etch (roughness etch), emitter and phosphor glass removal and PECVD. Therefore a second batch was made. This batch consisted of a reference-group (after saw-damage

etch) and fully processed solar cells. Half of the finished solar cells were used for soldering and are not used in experiments described in section 7.2.2.

### ***2.1.2 Composition and dimensions of Al-Si layer***

Determinations of the Al-Si layer and the BSF compositions have been performed in the past, but the data could be somewhat outdated. To verify if the previous measurements are applicable to the cell examined in this study, SEM pictures and EDS measurements have been performed.

In a scanning electron microscope (SEM) electrons are emitted from a cathode and accelerated towards an anode using field emission. The electron beam is focused to small spot. This spot is used to scan (in a grid) over a sample surface. This primary electron beam interacts with the sample. The volume in which interaction takes place is teardrop-shaped due to repeated scattering and absorption of the electrons (which lose their energy). The size of the interaction volume depends on the beam accelerating voltage, the examined material and the specimen's density. Imaging is most often done by detection of secondary electrons. The number of electrons reaching the detector determines the brightness of the image. As the angle of incidence increases, more secondary electrons will be emitted. Steep surfaces and edges tend to be brighter than flat surfaces, which results in images with a well-defined, three-dimensional appearance.<sup>18</sup> The suggestion of three dimensions makes this technique well suited for fracture surface examinations.

Apart from making beautiful secondary electron images, X-rays are generated in the material. If the incident electron energy exceeds the energy required to eject an electron from an atom in the specimen, this material is ionized. The energy of the atom can then decay by an electron transition into the created vacant state. Such a transition will be accompanied by the emission of a photon, which has an energy in the X-ray region. This phenomenon can be used in wavelength dispersive spectrometry (WDS) and in energy dispersive spectrometry (EDS). Both detectors “count” X-rays and are limited by the rate at which they are able to accept photons.<sup>18</sup>

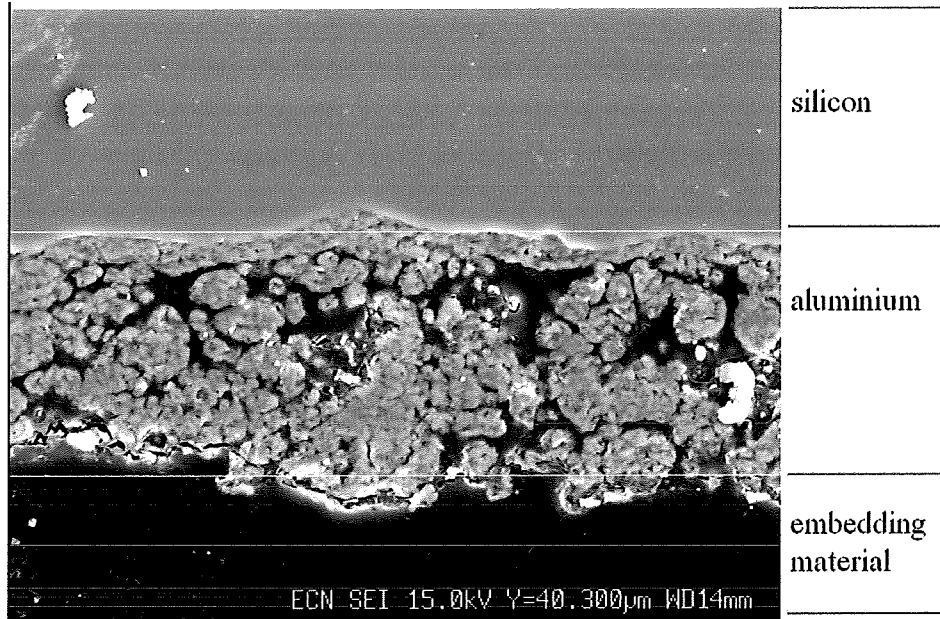


Figure 10. A SEM picture from a cross section of the aluminium layer on a solar cell, the distance between the white lines is  $40.3 \mu\text{m}$ , this indicates the thickness of the aluminium layer.

The SEM pictures indicate that the aluminium layer is approximately  $40 \mu\text{m}$  thick and the silver layer approximately  $10 \mu\text{m}$ , as shown in figure 10 and 11.

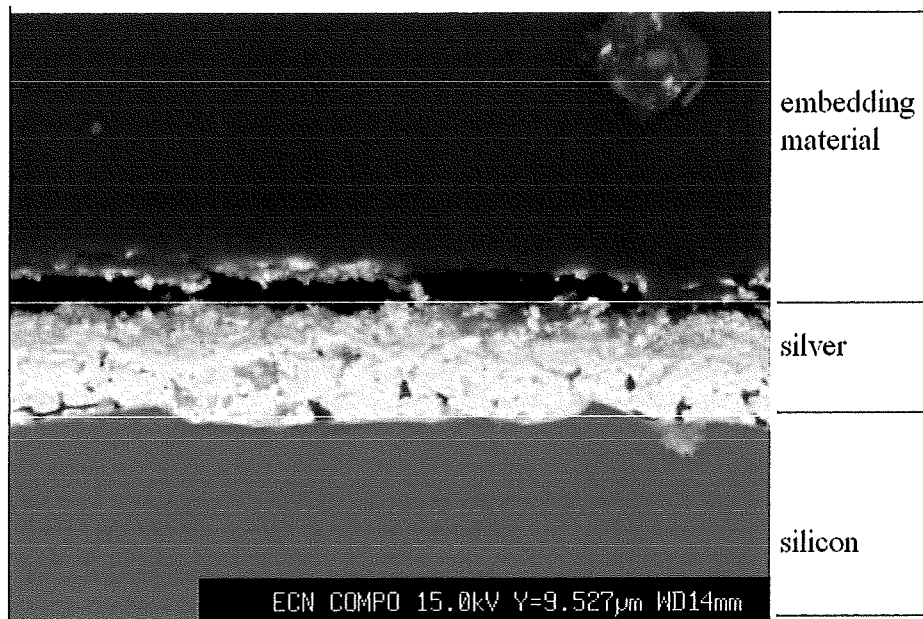


Figure 11. A SEM picture from a cross section of the silver layer on a solar cell, the distance between the white lines indicates the thickness of the silver layer and is  $9.5 \mu\text{m}$ . The dark area is delamination between the silver and the embedding material.

Four EDS measurements were done, moving the measuring position. The measuring point was a small square ( $1 \times 1 \mu\text{m}$ ), to even out the composition on that area. The scan started in the silicon and moved into the aluminium. Results are presented in table 1. The second and third measurements are taken from the Al-Si layer. In

agreement with previous measurements the silicon content of the Al-Si alloy is beyond 12 wt%.

	wt% of silicon, wt% error	wt% of Aluminium, wt% error
1	99.38 +/- 0.83	0.62 +/- 0.03
2	23.93 +/- 0.21	76.07 +/- 0.34
3	18.22 +/- 0.16	81.78 +/- 0.34
4	11.45 +/- 0.13	88.55 +/- 0.36

Table 1. Composition data of measuring points 1 through 4, 1 being in the silicon and 4 being completely in the aluminium area.

In the SEM pictures, no sign of alloying between the silver and the silicon (or silicon nitride) is visible in figure 11. This is not the case for the aluminium. The aluminium alloys with the silicon, creating a concentration gradient. This gradient makes an estimate of the mechanical properties, especially Young's modulus, of this layer extremely difficult. Data on the properties of Al-Si alloys are limited to engineering alloys with a silicon content below 12 wt%, in agreement with the eutecticum shown in the phase diagram (figure 12). This is definitely not the case in the gradient layer. If the silicon content in an alloy exceeds 12 wt%, segregation occurs. In the production, printing and firing procedures, this is not a likely scenario. From a production point of view the alloying is problematic. If alloying occurs due to diffusion of Al into the silicon and silicon into Al, the layer thickness is related to the temperature and the diffusion coefficient of Al in silicon (and as Al is much larger than silicon, this diffusion will be slow). The Al-Si layer is approximately 20 micrometers, which is too large a distance to be covered by diffusion in a matter of seconds. The details of the formation of this alloy are beyond the scope of this project but are interesting for future research.

The estimation of properties of the alloy between silicon and aluminium is difficult. In addition it is difficult to measure the properties of the Al-Si layer, separate from the aluminium and silicon layers. So instead of measuring, information on existing Al-Si alloys is used.

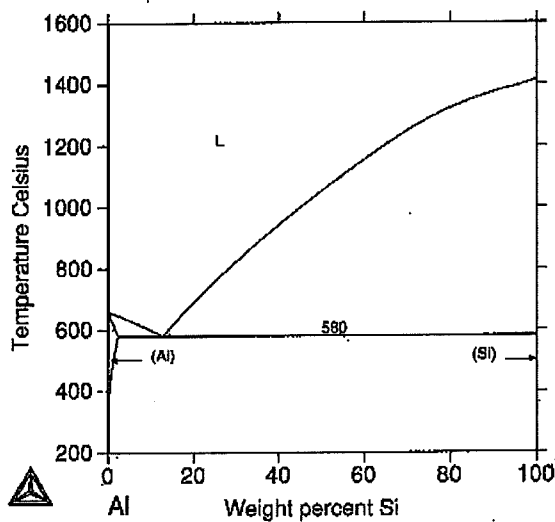


Figure 12. Phase diagram of aluminium and silicon.

## 2.2 Research questions

After the initial observations the research questions evolved accordingly. The cells are already severely curved before the soldering takes place. So from the initial questions the following have evolved:

### *Cell properties*

In what condition do the cells arrive at the connection step?

What are the properties of the layers applied before electrical connection?

What stresses are present in the materials?

Which cells survive the different process steps?

Which cells survive the soldering process?

### *Process influence*

At which step(s) is stress introduced into the cell?

Are steps present that reduce the stress?

How does the thickness of the wafer influence the degree of deformation?

Is the soldering process limited by the deformation that is present?

What are the similarities between cells that survive the soldering process versus those which do not?

What is the minimum thickness required for soldering (or other process steps)?

### *Fractures*

When and where does fracture actually occur?

Are (surface) cracks present in the materials?

What relation does the roughness of the surface have to the fracture?

## 2.3 Potential methods of stress measurements

The heat and mechanical input of the soldering process, together with stresses resulting from preceding process steps, and the location of fracture could reveal mechanical weaknesses in the cell design. If stress peaks are located in cells before soldering, it would be interesting to see at which of those peaks the cells fail, and what phenomena cause the stress peaks.

Before approaching the problem further, some experimental methods to determine the stress state of the cells as they enter the soldering process will be discussed.

### **2.3.1 Stress measurements**

Residual stresses of a silicon wafer have been measured in the past. If such a scan is precise enough it could be possible to show the effect of the metallisation pattern on the local stress distribution. Several techniques could be interesting for such an analysis, and are discussed and compared in this section.

As with force, stress cannot be measured directly but is usually inferred from measurements of strain and knowledge of elastic properties of the material. Examples of devices capable of measuring stress indirectly in this way are strain gauges and

piezoresistors. These tools are attached to the sample during the application of stress, due for example to the connection of the devices to the “outside world” to process the generated signal. Unfortunately, ovens and etching steps inhibit the proper functioning of simple devices for stress measurements.

Micro-Raman spectroscopy has been used by Kouteva-Arguirova<sup>19</sup> to measure stress distributions of block cast poly-crystalline silicon samples. In the literature this method is normally described as piezospectroscopy<sup>20</sup> or, when combined with optical microscopy, as optical fluorescence.<sup>21</sup> The stresses are calculated from the shift in frequency of the luminescence lines. In this research the residual stresses around grain boundaries were investigated. The residual stress detected in the silicon wafer is in the order of 50 MPa. An additional suggestion was that the crystal around the grain boundaries might be inferior because of dislocations or higher impurities levels. For poly-crystalline materials the assumption is often made that the crystallographic orientation is averaged out over the grains (this could be in error for large grains).<sup>22</sup> The depth to which measurements can be made is up to 500 micron below the surface. Stresses between 400 and 1000 MPa have been measured by Ma and Clarke.<sup>21</sup>

Infrared transmission polariscopes are also used to determine residual stresses in thin poly-crystalline silicon sheets.<sup>23</sup> Silicon is transparent to near infrared optical irradiation. Photoelastic parameters have been determined, allowing for the calculation of residual stress. For these calculations the wafer thickness has to be known. Unfortunately this technique has no results for cast poly-crystalline silicon thus far. ECN is now working with *GS Improve* (a company with experience in photoelastic measurements) to make measurements, however no results are available so far. Both the large grains and the presence of the anti-reflective film have a negative influence on the measurements.

Laboratory based X-ray diffraction (XRD) suffers from having a relatively small penetration depth (50 micron)<sup>29</sup> The basic theory of X-ray diffraction stress analysis is based on measurement of the lattice spacing of crystallites which satisfy the Bragg condition for a particular reflection. It is the atom spacing that is measured and related to the stress present in the material.<sup>18</sup>

Shadow-Moire Interferometry is an experimental technique that measures out-of-plane displacements (warpage), thereby detecting residual stresses. Unfortunately this technique gives no information about local stresses (it has a spatial resolution for measuring displacements of approximately 200  $\mu\text{m}$ ).<sup>24</sup>

Of these methods XRD and Raman spectroscopy are very promising for the detection of local stress distributions before soldering. The possibilities and challenges will be described in further detail.

### **2.3.2 X-ray diffraction**

The basic theory of X-ray diffraction stress measurement is based on the Bragg condition,<sup>18</sup> which states:

$$2d \sin \theta = n\lambda , \quad 2.1$$

and is illustrated by figure 13.  $d$  is the distance between atom planes,  $n$  is an integer and  $\lambda$  is the wavelength of the X-ray. Some of the X-rays will be reflected by the first layer, some by the next layer. By constructive interference, the reflected waves remain in phase if the difference in the path length of each wave is equal to an integer multiple of the wavelength. This is only valid for specific angles. Stress free crystals will show peaks of diffracted X-ray at those specific angles.

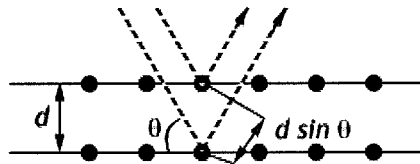


Figure 13. Schematic representation of diffraction calculation principles.

When the material is stressed this influences the interatomic distances between planes. The alteration of atom distances (strain) can cause both shifting and broadening of these peaks.<sup>25</sup>

XRD has been used in the past to measure stress distributions in poly-crystalline materials. A homogeneous distribution of grains and random orientation of the crystals is required, as is a small grain size.

The XRD equipment of the Materials Science and Engineering department in Delft was inadequate, because it was difficult to focus on only one crystal. Even if one crystal could be selected the interpretation would be questionable because the stress state of that particular grain might differ from other grains.

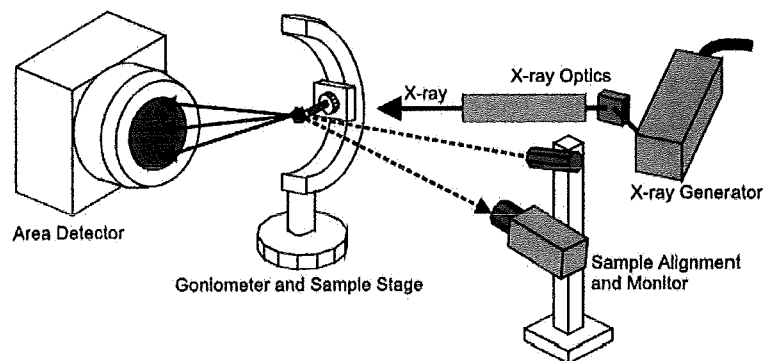


Figure 14. Set up of a 2D XRD apparatus.

A 2D XRD measurement of a poly-crystalline material gives Debye rings. These rings are generated by a large collection of individual reflections and known as the Debye Scherrer pattern (DBS pattern). Traditionally these images were created using a Debye Scherrer camera and film (the Straumanis method). Currently 2D XRD systems are available (see figure 14), which can measure Debye rings (or diffraction cones)<sup>26</sup> and do calculations on the rings. A relationship exists between the stress tensor and the diffraction cone distortion. 2D XRD on poly-crystalline solar cells

should be possible if the beam can be located on a single grain within the sample. If only one crystal is selected, the Debye ring will not be complete (see figure 15a), however if sufficient peaks can be observed Debye rings could be constructed mathematically from the visible peaks. When a material is stressed these rings deform, and from this deformation, the level of stress can be determined.

According to US patent nr 5,073,918, at least six peaks should be visible. This patent concerns a method to determine the crystallographic orientation of a single crystal silicon wafer, by using a 2D photosensor array. However, the one dimensional XRD pattern of silicon shows peaks belonging to the (111), (200) and (311) planes.<sup>27</sup> Of these peaks the (111) is the strongest.

The XRD equipment of the NanoStructured Materials group in Delft has a 2D detector, which theoretically could be used to measure multiple diffraction peaks. The issue of representative grains remains the same as it was for normal XRD, but it is possible to measure with a much higher speed than traditional XRD, allowing for a large number of grains to be measured.

Two different arrangements were used; the first belongs to the NanoStructured Materials group and is set up for transmission and the second belongs to Bruker AXS (the manufacturer) and is set up in reflection mode; similar equipment is currently in use by NRG<sup>d</sup>. The expectation was that the reflection configuration would suffer less from signal absorption and so give clearer results.

Both the TU Delft and the Bruker experiment only showed the (111) peak. This is insufficient to determine stresses. The position of the spot had some slight variation near a grain boundary in comparison to the bulk value. A representation is shown in figure 15b, in comparison to a single crystal measurement from which the stress could be calculated.<sup>28</sup> This variation in position of the spot can be due to variation in stress, but also to the dislocation density and the amount of impurities.

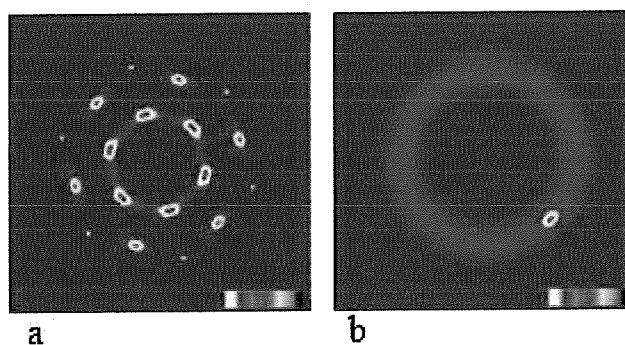


Figure 15. A comparison between a) a radial plot of x-ray diffraction of a single crystal from a block copolymer and b) a representation of the results from the silicon wafer measurement by the TU Delft. The faded blue circle is the silicon reference powder on top of the wafer.

<sup>d</sup> This set-up has a mono detector and a cradle system.

### 2.3.3 Raman spectroscopy

The Raman effect occurs when light impinges upon a molecule and interacts with the electron cloud of the bonds of that molecule. Energy is exchanged between the incident photons and the molecules. This exchange creates an energy difference between photons that enter the material and those that leave the material. The energy differences are equal to the differences of the vibrational and rotational energy-levels of the atom. Only specific photons, of which the solutions of the wave equations do not extinguish each other, are allowed by the periodic structures of crystals. So only for specific wavelengths will Raman scattering appear. Absorption of energy by an the atom is Stokes Raman scattering, the loss of energy is anti-Stokes Raman scattering, this is shown in figure 16. In Raman spectroscopy the frequency of light scattered from a molecule may be changed due to the molecular bonds and the presence of strain. A monochromatic light source (laser) is required for illumination, and a spectrogram of the scattered light then shows the deviations caused by state changes in the crystal. A shift in frequency can be observed due to stress in the material. An increase can be found with compressive stress and a decrease with tensile stress.

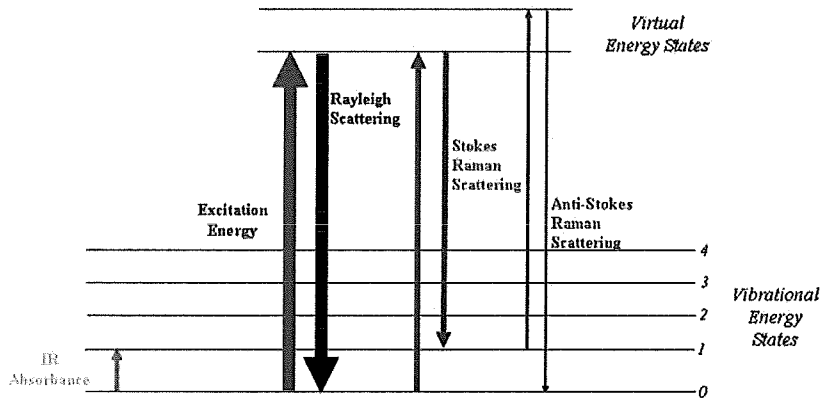


Figure 16. Raman spectroscopy is represented by the green line that connects energy states.

One of the requirements of Raman spectroscopy is transparency of the sample material. Metals are reflective materials, preventing the light from entering metal samples or samples with metal layers.

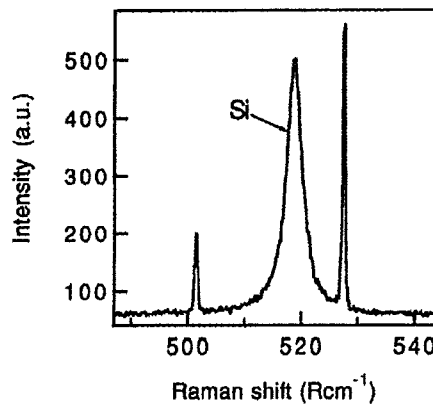


Figure 17. A Raman spectrum obtained from a (100) silicon wafer, using a 457,9 nm laser as excitation source.

For a stress measurement the material will have to be sensitive for Raman scattering, i.e. there should be a well-defined Raman peak in the spectrum. Silicon wafers exhibit a typical Raman signal; figure 17 shows this signal obtained in back scattering. In the absence of stress the silicon Raman peak is strong at a frequency of about  $520 \text{ Rcm}^{-1}$  (an inverse unit for wavelength). This value may change somewhat from experiment to experiment, depending on the calibration of the spectrometer and pre-monochromator.<sup>29</sup>

A peak shift of  $1 \text{ Rcm}^{-1}$  corresponds to a stress of about 500 MPa, for silicon under uniaxial stress in the [100] direction. In addition to the silicon Raman line, some other peaks are also visible in figure 17. These are plasma lines from the laser. These lines are Rayleigh scattered, and insensitive to stress in the material. For this reason, they can be used to compare the shift in stress measurements, without having to fully determining the inaccuracy of the measuring equipment.

Important to note is that the measured value is dependent on the calibration of the system. This means that relative shifts can be observed with great accuracy, but the absolute shift is not reliable as a stress measurement. The shift in the Raman spectrum can have several causes: stability of the laser and the Raman instrument can both have a rather severe influence.

### **2.3.4 Conclusions on stress measurement methods**

Methods like X-ray diffraction and Raman spectroscopy are not suited for complete cells.

X-ray diffraction was ineffective. If sensors become more sensitive at least two other peaks might become visible. However this might still be insufficient to perform stress measurements. The shift in peak position near the grain boundary could well indicate a change in stress level, unfortunately the presence of dislocation pile-ups, interstitials and impurities could also influence this measurement (and these do occur more near the grain boundaries). Two dimensional X-ray diffraction can be used to measure stress in materials with large grains other than silicon, if enough diffraction peak are present. The effect of the silver pattern on stress, not only the H-pattern, but also those related to PUM technology<sup>30, e</sup> could be examined by using a wafer of a different material. That material should be selected to provide sufficient diffraction peaks, or complete Debye rings.

Raman spectroscopy already found its application in solar technology. If the metallisation of the H-cells is adjusted, leaving enough areas free of metallisation, this technique could well be applicable. For this reason it should not be discarded as a technique for this type of wafer (before the metallisation is applied).

---

<sup>e</sup> PUM technology is another type of solar cells that uses the same materials as the H-pattern cells.

## **Chapter 3      Theory concerning stresses induced by processing steps**

In this chapter the effect of different process steps on the stresses in the solar cells is examined. The curvature of a cell can reveal tensions in the material, similar to the Shadow-Moire Interferometry describe in section 2.3.1. Curvature measurements are executed on the whole surface, and give an estimate of the tensions between several material layers.<sup>31</sup> The curvature can be measured in different ways, which include scanning along a certain line, and also simply measuring the height difference between centre and edges.

Not only measurements can indicate the degree of stress induced by a process step. Calculations of events that occur during a particular step can show the effect of that step on the wafer. Some modelling work on soldering has been done by ECN in the past. The measurements and calculations can be used in a complimentary manner to evaluate the process steps. For the calculations, the properties of the materials subjected to a particular process step should be known.

### **3.1    Material properties and dimensions**

Silicon is a brittle material, which is not used as a construction material. Properties have often been investigated from an electrical point of view. This has stimulated the research of mechanical and thermal properties of single crystal silicon, as this is used most in the semiconductor industry. Hull<sup>32</sup> has collected quite some data on the properties of single crystals. For fracture mechanics the fracture toughness  $K_{Ic}$  is important. This has been determined for different crystalline planes.  $0.93 \pm 0.3 \text{ MPa}\times\text{m}^{0.5}$  on (111) and  $0.89 \pm 0.3 \text{ MPa}\times\text{m}^{0.5}$  on (110). For comparison values for the fracture toughness of various materials are given in table 2.<sup>33</sup>

	Material	Fracture toughness
Metals :	Aluminium alloy	24-44 MPa (m) <sup>0.5</sup>
	Steel alloy	50 MPa (m) <sup>0.5</sup>
	Titanium alloy	55 MPa (m) <sup>0.5</sup>
Ceramics :	Aluminium oxide	2.7 -5 MPa (m) <sup>0.5</sup>
	Concrete	0.2-1.4 MPa (m) <sup>0.5</sup>
	Soda-lime-glass	0.7-0.8 MPa (m) <sup>0.5</sup>

Table 2. Examples of typical values for the fracture toughness of various materials.

Because the most fragile material in a solar cell (silicon) is brittle, the deformations occurring before fracture will only be elastic. If this is assumed for the cell in all production steps, the curving of the silicon after firing will not involve plastic deformation (this only holds for the silicon). The bowing of the solar cells has been described in the literature as a major problem for module manufacturing,<sup>34</sup> and occurs during metallisation. This phenomenon can be explained by the thermal stresses that are introduced after firing. The thermal expansion coefficients for Al and Ag are quite different from that of Si (see table 3).<sup>35</sup>

Material	Young's modulus [MPa]	Poisson's ratio	Thermal expansion coeff. [ $10^{-6} \text{ }^\circ\text{C}^{-1}$ ]
Si	110,000	0.218	2.6 <sup>f</sup>
Ag	72,300	0.37	19.2
Al	70,000	0.33	23.6
Al-Si	20	0.33	6.0
Cu	117,000	0.36	16.6

Table 3. Data that have been used in thermo-mechanical calculations by Van Hoesee, with the exception aluminium which was taken from Callister.<sup>33</sup>

One of the major problems in multi-crystalline silicon is the behaviour of structural defects. Dislocations, grain boundaries and impurities determine the properties of a solar cell. Due to the strong influence of dislocations and impurities on the performance of solar cells a lot of research has been done in this area. For a more detailed discussion on structural defects of multi-crystalline silicon references [36], [37] and [38] could be useful.

### 3.1.1 Porosity

The silver and aluminium metallisation layers are porous. Porous materials can be considered as composite materials, with air as the inclusions. Several properties of the layers are needed for the prediction of mechanical behaviour. Because the assumption is that the actual fracture occurs in the silicon, the Young's modulus seems a good place to start. Several methods to calculate the Young's modulus of composites are available. These are the slab model, the Eshelby model and the Tsai-Halpin model.<sup>39</sup>

The slab model has its origins in the calculation of the material stiffness for composites reinforced with continuous fibres loaded in the direction of the fibres. The slab model assumes the strain in the inclusion direction is uniform, so by the "rule of mixtures" it will predict the overall modulus in terms of the moduli of the constituent phases and their volume fractions.<sup>39</sup>

$$E_c = fE_i + (1 - f)E_m \quad 3.1$$

This is also known as the Voigt model, not to be mistaken with the Kelvin-Voigt model. In the Voigt model  $f$  is the volume fraction of the inclusions,  $E_c$  is the composite stiffness and  $E_i$  and  $E_m$  those of the inclusions and the matrix, respectively.

Perhaps the most popular model is an empirical one known as the Halpin-Tsai equation, which can be written in the form:<sup>39</sup>

$$E = \frac{E_m (1 + \xi \eta f)}{(1 - \eta f)} \quad \text{with} \quad 3.2$$

<sup>f</sup> The values used by Kramer van Hoesee, were 0.17 and  $4.2 \times 10^{-6} \text{ }^\circ\text{C}^{-1}$ , however use of the values published by Hull was advised.

$$\eta = \frac{\left( \frac{E_i}{E_m} - 1 \right)}{\left( \frac{E_i}{E_m} + \xi \right)} \quad 3.3$$

$\xi$  is an adjustable fitting parameter (usually in the order of unity). More details on these models can be found in references [40], [41] and [42].

### 3.2 Thermal stress calculations

In the production process, several thermal steps are included. The metallisation process is one of the most interesting, as this includes several material layers cooling down as it forms a new structure. For thermal stresses, simple calculations can be made to estimate the stresses induced by the influence of heat on a structure with different material properties.

The bowing tendency is indeed reduced by decreasing the firing temperature.<sup>43</sup> A bending moment can be caused by the difference in the elongation of two (or more) layers. A cross section of a solar cell can be viewed as two (or more)<sup>§</sup> parallel beams clamped to rigid plates with the rigid plates free to move in horizontal direction, as shown in figure 18.

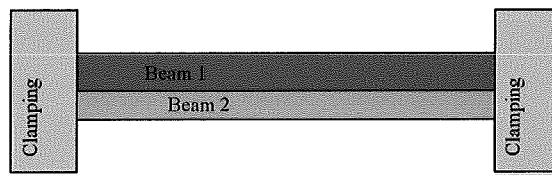


Figure 18. Two parallel beams clamped to rigid plates, the rigid plates are free to move in horizontal direction.

If a beam is subjected to a mechanical load, in this case a bending moment, it will deform. Several methods can be used to describe this problem, two of which are considered: Bernoulli-Euler and Kirchhoff. If the Bernoulli-Euler hypothesis is considered valid, a plane section that is perpendicular to the longitudinal axis of the beam before loading will remain plane and perpendicular to the axis after loading.

Unfortunately in this case, there is no perfect beam, but a thin plate. Traditionally the deflection of plates (due to stresses) is described using the plate bending theory known as the classical or Kirchhoff's plate theory. The fundamental assumptions of the linear, elastic, small-deflection theory of bending for thin plates may be stated as follows:

1. The material of the plate is elastic, homogeneous, and isotropic.
2. The plate is initially flat.
3. The deflection (the normal component of the displacement vector) of the midplane is small compared with the thickness of the plate. The slope of the

<sup>§</sup> The number of layers used in the calculation depends on layers present, and on which layers are assumed to have an influence on the bowing.

deflected surface is therefore very small and the square of the slope is a negligible quantity in comparison with unity.

4. The middle plane before bending, remains straight and normal to the middle surface during the deformation, and the length of such elements is not altered. This means that the vertical shear strains are negligible and the normal strain may also be omitted. This assumption is referred to as the hypothesis of straight normals.
5. The stress normal to the middle plane, is small compared with the other stress components and may be neglected in the stress–strain relations.
6. Since the displacements of a plate are small, it is assumed that the middle surface remains unstrained after bending.

Many of these assumptions, known as Kirchhoff’s hypotheses, are analogous to those associated with the simple bending theory of beams. These assumptions result in the reduction of a three-dimensional plate problem to a two-dimensional one. Consequently, the governing plate equation can be derived in a concise and straightforward manner.<sup>44</sup>

As many of the requirements for Kirchhoff’s hypotheses are not met, neither are those of the Bernoulli-Euler hypothesis, accurate assessments cannot be made.

Due to changing temperatures, the Young’s modulus is not necessarily constant for the different layers, nor is the deflection of the plate small in comparison to the thickness. The silver layer on the top surface is not homogeneous in geometry and the Al-Si, Al and Ag layers do not have homogeneous properties (neither does the silicon). Thermal stress calculations including these difficulties can be performed using computer models. For rough estimates either could be used, in this case the hypothesis Bernoulli-Euler is preferred because of its simplicity.<sup>31</sup>

A thermal stress in a plate, will result in a strain. The strain components will be  $\varepsilon_x$  and  $\varepsilon_y$ .

$$\varepsilon_x = \varepsilon_y = \varepsilon_0 + \frac{z}{\rho} , \quad 3.4$$

where  $\varepsilon_0$  and  $\rho$  are the in-plane strain and the radius of curvature of the neutral plane respectively and  $z$  is the distance (normal to the plate) from the neutral plane.

If thermal stresses occur in multi-layered composite beams, the dimensions and properties of the different materials can be incorporated in this system. Some models consider the effect of layers to be negligible, however, when researching thinner wafers, the relative importance of these layers greatly increases.

The concept of a thermal stress calculation is that two bars of the same length subjected to a temperature change will respond differently according to their Young’s moduli and thermal expansion composition. For a simple beam (without layers) the equation for the strain is the following:

$$\varepsilon = \frac{\sigma}{E} + \alpha(T_1 - T_0) = \frac{\sigma}{E} + \alpha\Delta T \quad 3.5$$

Here  $\alpha$  is the linear coefficient of thermal expansion for the material. The change in temperature will be denoted as  $\Delta T$  from now on.

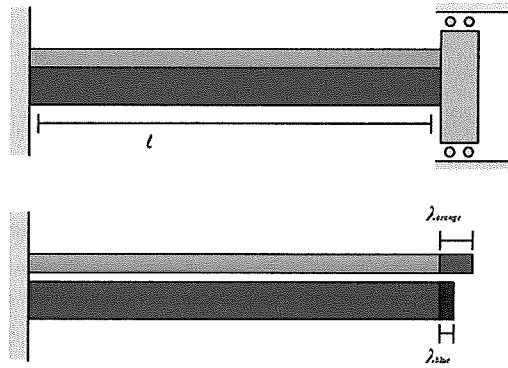


Figure 19.a) Two parallel beams clamped to rigid plates, the rigid plates are free to move in horizontal direction. b) The same beams, elongated by thermal expansion, when they are not clamped.

In a structure the whole object remains the same, even if the layer that built the structure behaves differently, assuming that no delamination occurs. A small sketch (figure 19) can demonstrate the effect that the layers will have on each other. As the layers are very much attached to each other, the elongation what would occur if they were free to move is translated to a compressive stress in the orange layer (the film) and a tensile stress in the blue one (the substrate).

$$\lambda_{\text{substrate}} = \alpha_{\text{substrate}} \Delta T l + \frac{\sigma_{\text{substrate}}}{E_{\text{substrate}}} l \quad 3.6$$

$$\lambda_{\text{film}} = \alpha_{\text{film}} \Delta T l + \frac{\sigma_{\text{film}}}{E_{\text{film}}} l \quad 3.7$$

$$l + \alpha_{\text{substrate}} \Delta T l + \frac{\sigma_{\text{substrate}}}{E_{\text{substrate}}} l = l + \alpha_{\text{film}} \Delta T l + \frac{\sigma_{\text{film}}}{E_{\text{film}}} l \quad 3.8$$

From these equations follows an elongation of the total structure,  $\lambda$ , which can be determined by an equilibrium of forces, using the area of a cross section of the layers and the pressure they exert.

$$\lambda = \lambda_{\text{substrate}} = \lambda_{\text{film}} = \frac{(\alpha_{\text{substrate}} E_{\text{substrate}} A_{\text{substrate}} + \alpha_{\text{film}} E_{\text{film}} A_{\text{film}}) \Delta T l}{A_{\text{substrate}} E_{\text{substrate}} + A_{\text{film}} E_{\text{film}}} \quad 3.9$$

This elongation causes stresses in the substrate and the film, respectively.

$$\sigma_{\text{substrate}} = \frac{E_{\text{substrate}} (\lambda - \alpha_{\text{substrate}} \Delta T l)}{l} \quad 3.10$$

$$\sigma_{\text{film}} = \frac{E_{\text{film}} (\lambda - \alpha_{\text{film}} \Delta T l)}{l} \quad 3.11$$

Due to the thermal stresses, a bowing of the structure can occur. An estimate of the macrostresses can be made using Stoney's equation.<sup>45</sup> Unfortunately several versions of this equation are in circulation. Bell Labs contradicts the equation used by Klein. In the derivation by Klein, the thicknesses vanish in the stress calculation. The equation by Bell Labs is used, as this equation is supported by a correct derivation.

$$\sigma = \frac{1}{6} \frac{E_{\text{substrate}}}{(1 - \nu_{\text{substrate}})} \frac{t_{\text{film}}^2}{t_{\text{substrate}}} \frac{1}{R}, \quad 3.12$$

is used to evaluate the macrostress  $\sigma$  in a layer on a thick substrate. This model uses only the material properties of the thickest layer, namely Poisson's ratio ( $\nu$ ) and the radius of the sample ( $R$ , and  $R_0$ , which is the initial situation). Of both layers the thickness is included as  $t_{\text{substrate}}$  and  $t_{\text{film}}$ . The formula applies only in the "thin-film approximation," that is, for coatings much thinner than the substrate. Stoney's equation does not cause serious errors for thickness ratios  $d < 0.1$ <sup>46</sup>, where  $d$  is defined as the film thickness divided by the substrate thickness). As the ratios of the aluminium versus the silicon vary from 0.2 to 0.33 this assumption is not correct. The approach could be used for an indication of the bowing that can occur due to the thermal stresses introduced by the production process, merely to estimate an order of magnitude. As solar cells become much thinner, the flexibility increases. Stoney's equation might prove a fast estimation when the conduction layer thickness greatly exceeds the photovoltaic layer. Philips research<sup>47</sup> has done a lot of work on the mechanics of flexible electronics, which is beyond the scope of this research but might be interesting for alternative solar cells.

### 3.3 Modelling

Computer models attempt to simulate a simplification of the reality of a particular system. Modelling can be done at several scales in both time and length. Molecular dynamics has often been applied in studying cracking behaviour. Holland and Marder have undertaken extensive research into modelling of silicon fracture.<sup>48 49</sup> Molecular dynamics simulations of brittle crack motion at the atomic scale have been done by Hauch, Holland, Marder, and Swinney in 1999 after initially researching ideal brittle fracture of silicon.<sup>50</sup> Their experiments and simulations disagree, showing that inter-atomic potentials are not yet well understood. It is stated on their website that they no longer believe that the inter-atomic potentials used in the research of 1998 are correct.<sup>h</sup> This is unfortunate, because the reliability of these data was a main reason for investigating silicon. From the investigations of this department it is clear that the theory concerning fracture at an atomic level is insufficient for a good agreement between reality and the molecular dynamics simulations.

For solar cells, a molecular dynamics model covers much too small a scale. One of the end goals of the ECN research is to model an entire module. Finite element analysis is an appropriate technique for such a large scale model.

ECN has previously made thermal models using the finite element approach. The simple model was made to describe the thermal input for soldering of a basic silicon

---

<sup>h</sup> <http://chaos.ph.utexas.edu/%7EEmarder/fracture/frac.html>

wafer with two copper ribbons (set contact area, plate thickness etc.). This model assumes that the silicon is stress free and the layers from the production process can be neglected, the construction is shown in figure 20. Two models have been made. The first one involves preheating of the cell: the copper ribbon and silicon wafer. The connecting of the ribbon to the wafer is over the complete length of 92 mm. Cooling down is done from the chuck temperature (the chuck is a block of material at the bottom of the cell, indicated by 3) to room temperature. In this model the focus was on the shear strength of the wafer. The second model is concerned with the melting time of the solder and the required energy. In this model the chuck (3) is at a predefined temperature. The top ribbon or tab (1) connects at six equal spaced points (18 mm apart) to the silicon wafer, which is the yellow area. In this model the solder can withstand temperatures between 200 to 1000 °C during the soldering process. The area of the solder surface is 4 mm<sup>2</sup>.

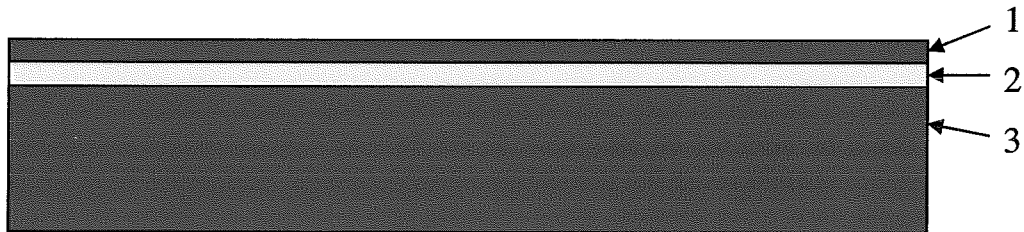


Figure 20. The ECN model consists of three parts: 1) copper ribbon. 2) silicon wafer. 3) chuck with predefined temperature.

Thermal stress calculations have also been made on one-cell modules by ECN.<sup>50</sup> This module was assumed to be tension free at room temperature. The calculations investigated the stress distribution at -40 and +85 °C. As mentioned previously, the assumption is that there is no tension in the wafer at room temperature. This is not the case and therefore this model might be too simple for the modelling of soldering on thinner wafers. The data that were been used for modelling, are shown in table 3.<sup>35</sup> These values are estimates. The precise nature of the Al-Si alloy is also unknown. The weighted mean of the Young's moduli of aluminium and silicon is 67.000 MPa, this was a rather coarse approximation and it does not include an alteration of the Young's modulus due to temperature dependence and porosity. The value was set at 0,02 GPa (an extremely low value and perhaps unlikely). When using this value, the influence of the Al-Si on the bending of the wafer was undetectable in the calculations. This result concurred with experiences from the production process.<sup>35</sup>

Not only processing steps, but also basic experimental data can be accompanied by models to increase understanding of the local stress distribution. Behnken et al. have examined several bending tests. The stress distributions connected with the applied forces have been simulated for six different bending test geometries, four of them are illustrated in figure 21. They differ in the number and the geometry of the supports and the punches to apply concentrated or line forces. The terminology used by Behnken is slightly different from the rest of this report, four point bending in the report will be similar to the four line bending described below.

- point bending: The force is induced at the centre of the wafer's top side, the three supports are positioned at the bottom side on a circle of radius 40 mm.

- biaxial point bending: The wafer is supported by a ring of radius 40 mm and the force acts at the wafer centre.
- double ring bending: The wafer support is again a ring of 40 mm radius and the force is transmitted by a ring of half diameter.
- 3-line bending (in this report named 3 point bending): The sample is supported by two parallel lines with distance  $d=80$  mm. The force is induced by a third line, centred between the supports.
- 4-line bending (in this report named 4 point bending): The forces are induced by two parallel lines ( $d=40$  mm) centred between the supports with  $d=80$  mm.
- twist test bending: The twist test is characterized by point supports on the wafer diagonal at 22 mm, 10 mm or 2 mm perpendicular distance to the wafer's edge.<sup>51</sup>

In these models, only one layer of elements was used to model the thickness, so the stress is represented in a sheet material, rather than a stiff wafer. However, for the comparison of different bending tests these models can still be used.

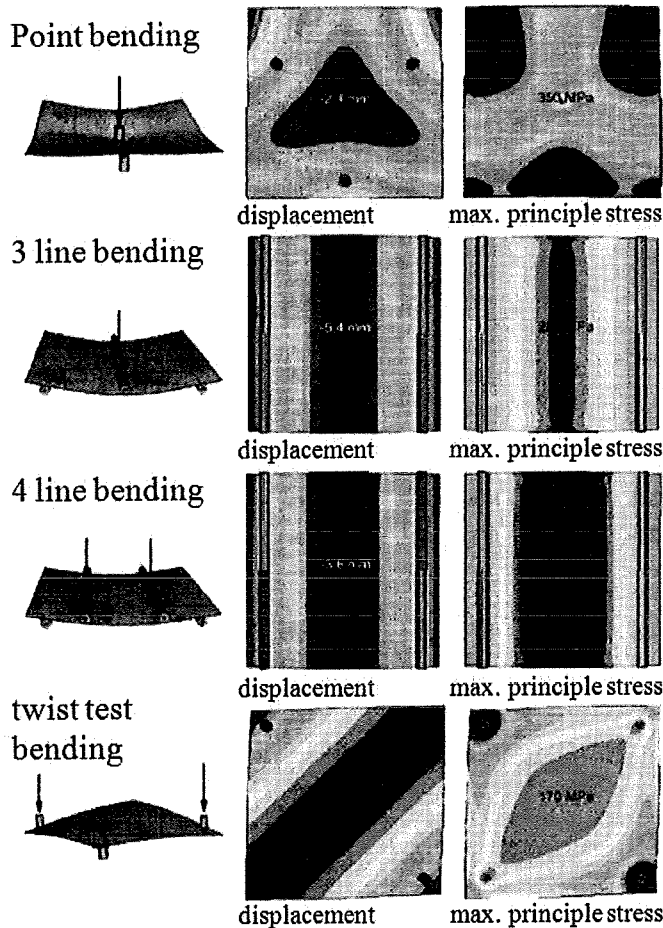


Figure 21. Test geometries of four bending tests and the respective contour plots of the displacements and the stresses on the respective wafer faces suffering from tensile stresses.

## **Chapter 4 Experiments concerning stresses induced by processing steps**

This chapter describes the experimental work concerning stresses at process steps. The presented experiments are curvature measurements, laser soldering experiment, calculations on thermal stresses and modelling of the bowing due to thermal stress. The results from the curvature measurements, calculations and modelling work are presented in chapter 5.

### **4.1 Curvature measurements**

A measure for the amount of deformation due to a process step is the degree in which the wafer is bent. By measuring the (new) curvature of the wafer the processing steps can be compared. Details on the samples can be found in sections 1.3 and 2.2.1.

Measuring the curvature can be done by lasers; in this technique light sensors register the reflection. This method is often applied especially in substrate research. Another option is using a mechanical sensor. In both cases either line or surface scans have to be performed. Using light is preferred because the force needed for the mechanical sensor can influence the values (press down the wafer) and cause some damage.

The available light sensor set-ups include a laser of 633 nm (Surfaces and Interface group TU Delft) and a 750 and 810 nm laser (Structure and Change group, TU Delft). The mechanical sensor (ECN) is a Mahr perthometer. With the perthometer line scans are made with a velocity of 3 mm/s. The surface damage can be examined by optical microscopy.

### **4.2 Modelling bowing and thermal stress**

In order to model the behaviour of the cell during soldering, the deformations inflicted in previous steps should be represented in some way. The calculation, which was carried out by Van Amstel,<sup>52</sup> is based on exposing a wafer to a simplified production process. The results of that “digital experiment” are compared to results from the curvature experiments and used for the follow-up experiments, which mimic four point bending on bowed cells. The most significant processing step, evaluated for the curvature, is the metallisation process. A schematic representation is shown below in figure 22. After the printing process is completed the wafer enters the oven. Because the connections between the silicon and the layers are created at high temperatures, the layers are considered to be added to the silicon at elevated temperatures as solids.

The model uses finite elements, in 3 dimensions, and both the silver and the aluminium are modelled. The Al-Si alloy is not included in this simple model. In order to get correct thermal and mechanical properties for the Al-Si alloy, the alloying should be included in the model.

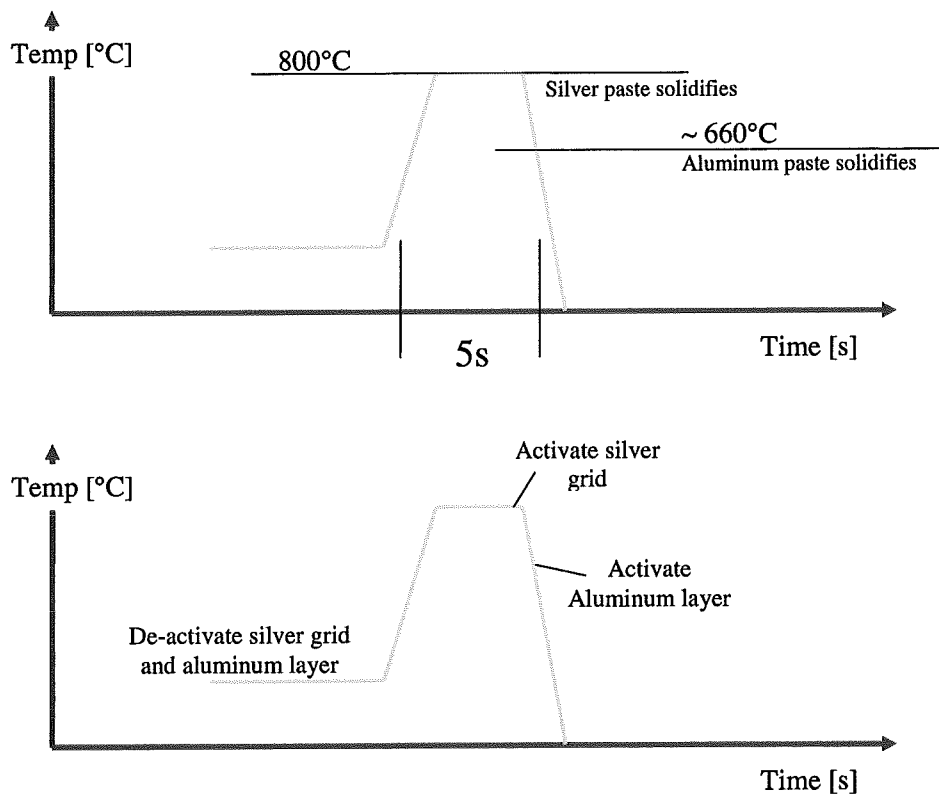


Figure 22. Representation of the steps included in the modelling of the metallisation process.

Parallel to the measurements, the finite element calculation was executed and compared with the values of the curvature measurements and the manual calculations. The layer properties used in the model are presented in table 4. More data that was used in the model can be found in appendix I.

The calculations can provide an estimate of the stresses that develop during the metallisation step. These calculations assume homogeneous materials and no alloys, as does the model. The reason is that interactions, like alloying and movements of interstitials, between the layers of aluminium and silicon are hard to quantify. The difficulty lies in determining the properties of the different layers and the alloying regions that can be formed between them.

<b>Aluminium layer</b>	
$\rho$ , density	2.7 g·cm <sup>-3</sup>
E, Young's modulus	20,000 MPa
$\nu$ , Poissons ratio	0.35 (no units)
$\alpha$ , Thermal expansion coefficient .	2·10 <sup>-5</sup> K <sup>-1</sup>
<b>Silicon</b>	
$\rho$ , density	2 g·cm <sup>-3</sup>
E, Young's modulus	150,000 MPa
$\nu$ , Poissons ratio	0.23 (no units)
$\alpha$ , Thermal expansion coefficient .	2.5·10 <sup>-6</sup> K <sup>-1</sup>
<b>Silver layer</b>	
$\rho$ , density	10.05 g·cm <sup>-3</sup>
E, Young's modulus	40,000 MPa
$\nu$ , Poissons ratio	0.37 (no units)
$\alpha$ , Thermal expansion coefficient .	1.92·10 <sup>-5</sup> K <sup>-1</sup>

Table 4 Data that have been used in digital experiment of the metallisation step.

### 4.3 Local heat input influence

One method of soldering is to use a laser beam. In this process a thermal stress is introduced in the material without mechanical contact between the sample and the heat source. For an industrial setup the laser is accompanied by a spring to press the ribbon and cell together. The TU set up is not equipped with such a clamping device, thus only enabling experiments with heat input, but without application of a local pressure, near the location of heating.

Laser soldering was executed in two series. The first series had the ribbon strapped over the busbar by adhesive tape at the ends of the ribbon. The tape was attached to the block beneath the solar cell. For the soldering a 3 kW Nd:YAG laser was used. In order to make a solder connection, several settings, ranging from 1 ms at 500 W to 10 ms at 1000 W were used.

Soldering done by laser soldering made good connections at a power of 750 W for 6 milliseconds. At higher power and time the laser blows little holes in the cell, at lower power and time the tabs do not connect to the silver. Using only heat input is not enough to crack a wafer. With increasing power silicon is sensitive to local heating, but a solder connection is established before this occurs. Therefore it seems reasonable to assume that the heat input alone is insufficient to cause fracture during soldering.

## Chapter 5 Results concerning stresses induced by processing steps

### 5.1 Curvatures

Curvature measurements show that buckling occurs, saddle shapes as well as twisting and bending distortions occur. The direction of bending is not the same for all cells. However, a bending distortion with a radius normal to the fingers is dominant. Also bending distortions parallel to the fingers and saddle forming are observed. As an example of these distortions, figure 23 shows curvature measurements parallel and normal to the direction of the busbars. The example is a 200 micron cell, displaying the bending as it most often occurs. The measurements of both curves are made from the lowest point, so in reality the top height of the blue curve is the place where the two curves meet.

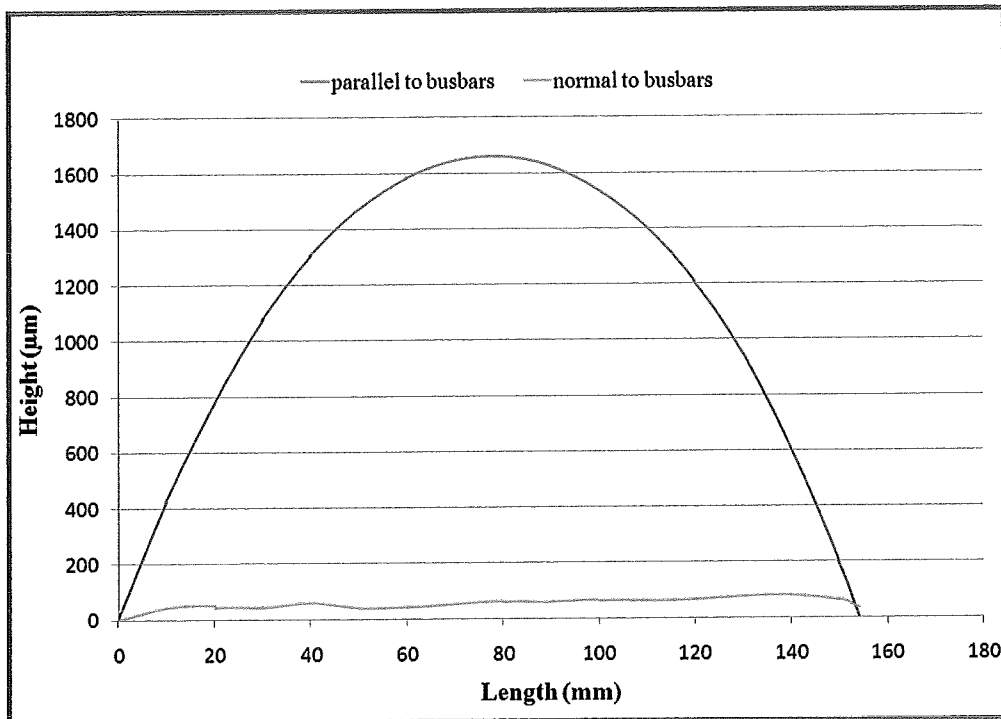


Figure 23. Results from representative curvature measurements of a 200 micron cell, parallel and normal to the busbars, blue and red, respectively.

The curves were measured with a mechanical sensor, the Mahr Perthometerconcept. The mechanical sensor had a severe influence on the bowing, the cell flattened under the pressure of the apparatus. The optical sensors did not flatten the cells. Unfortunately the signals of the optical sensors were absorbed by the solar cell, because of this the mechanical sensor was used.

The curvature measurements generate 420,000 points over a length of 154 mm. The curvatures shown in this section are constructed of 17 measurements. These points are selected to include measurements made on the silicon and not on the silver. The curvature measurements were made either normal or parallel to the busbars, in the direction where the curvature was most severe. In several cases it was impossible to measure along lines normal to the busbars and in almost all cases the deformation was most severe parallel to the busbars.

The spread in maximum height of the cells is large, but the differences between the different thicknesses are still obvious. The average values for the maximum height are shown in table 5. In addition to the values of maximum height, the number of cells that survived the production process and the average weight of the cell that survived have been included. These values indicate that the wafer cutting process is more reliable for thicker wafers than thinner ones, as is expected. The measured curves for the three thicknesses are shown in figure 24. The curves have been selected close to the average of cells of that thickness group.

Cell thickness	Survivals	Average weight (g)	Standard deviation of weight	Average maximum height ( $\mu\text{m}$ )	Standard deviation of height
120 micron	5/10	9.0	0.24	5143	842.1
160 micron	7/10	9.5	0.08	4119	559.5
200 micron	10/10	12.7	0.16	1807	122.1

Table 5. Results from the cells that survived the production process without visible damage.

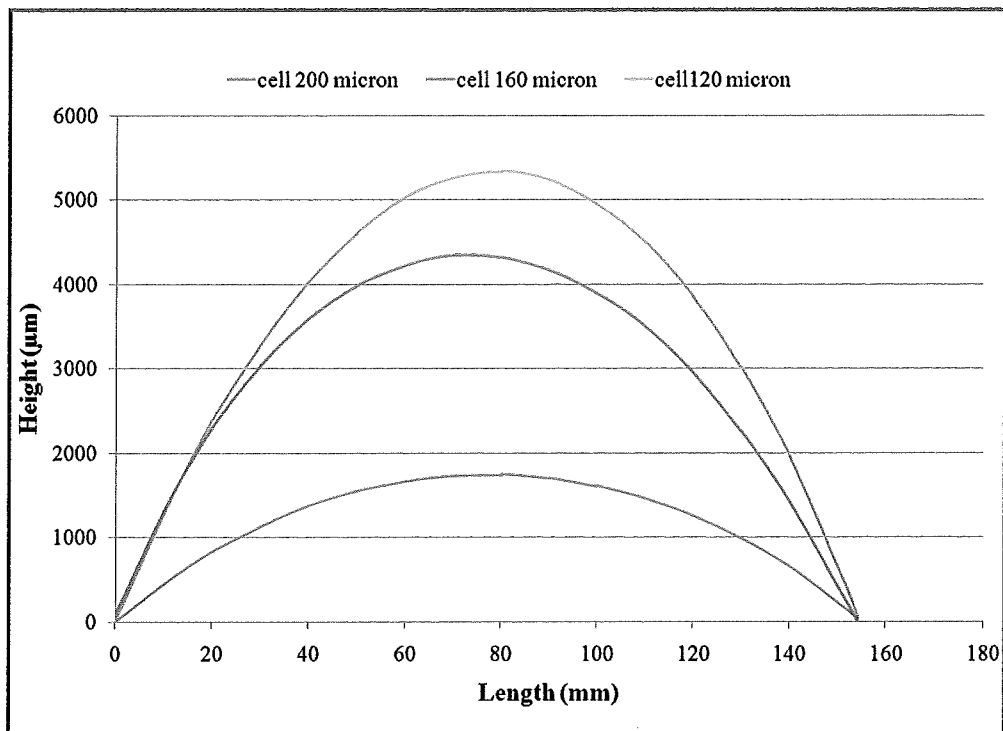


Figure 24. Results from representative curvature measurements over the centre of the specimens, parallel to the busbars, for three different thicknesses.

The difference between wafer and cell is evident and shown in figure 25 which illustrates the curvatures of four stages in the production process. The first three are similar to each other, the fourth, the complete cell, is severely deformed. The process step between the purple and the red line (PECVD and Cell) is the metallisation. A fair degree of distortion is introduced by this process step.

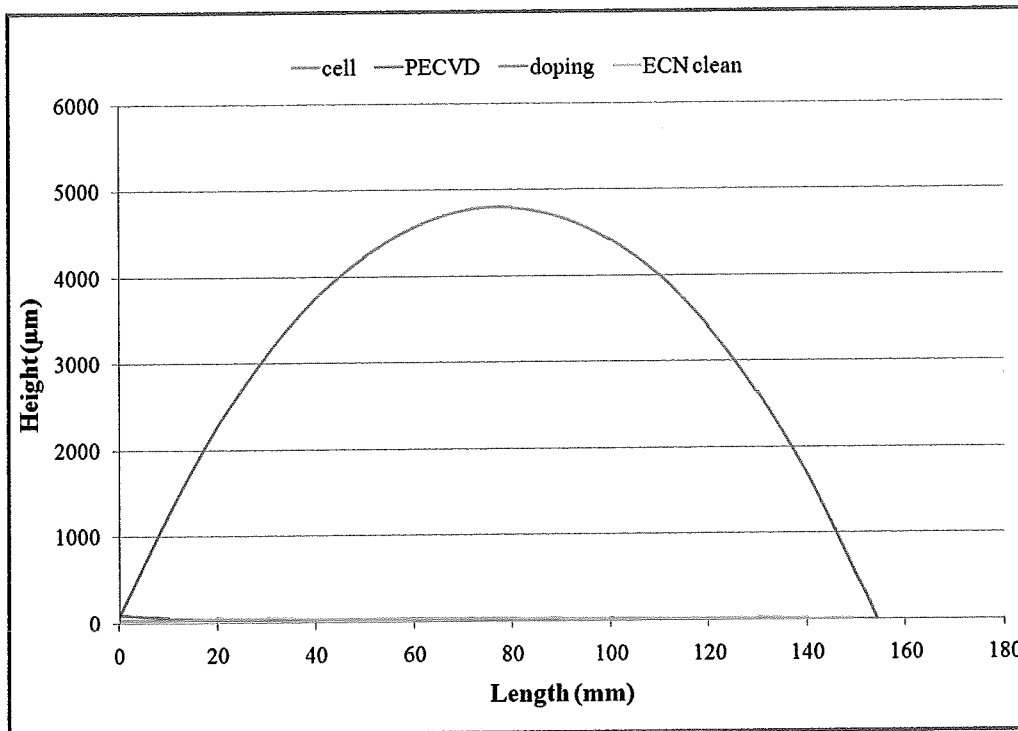


Figure 25. Results from different process steps, the green line is measured after the ECN clean, the blue line is taken after doping, the purple line is measured after the anti reflective coating is applied and the red line is of a complete cell. The lines are taken from neighbouring wafers, with exception of the complete solar cell.

## 5.2 Calculations of properties

The bowing of the cells can also be calculated, but these calculations require estimates of the material properties. Viewing a porous material as a composite is of course a rough estimation, therefore using a precise model to determine the properties of such a composite seems unnecessary. The simplest model available is the Slab model. For the silver and aluminium layer data on the extent of the porosity is needed. In research done by ECN for the Crystal Clear Project, the extent of porosity has been investigated.

The porosity of the silver was determined to be  $18.0 \pm 3.4$  % porous, for the crystal clear project.<sup>7</sup> The porosity of the aluminium layer was not determined, but photographs are available. From these photographs, a visual estimate can be made. Values for this first-sight estimation are: 25% porosity for aluminium. A more accurate method was evaluation by using a grid, where each block of the grid was designated air or aluminium. The evaluation using this grid gave a porosity of 27%.

Applying the simplest model, the Slab model, equation 3 gives the following information, assuming that the Young's modulus of inclusions that are air and/or organic solvents,  $E_i = 0$ . A summary of the calculated values can be found in table 6:

Material	Porosity	$E$ solid material	$E$ porous material
Silver	$18.0 \pm 3.4 \%$	72,300 MPa	59,286 MPa
Aluminium	27 %	70,000 MPa	51,100 MPa
Al-Si alloy		78,000 MPa	

Table 6 Estimates of the Young's moduli of the silver, aluminium and Al-Si layers in the solar cells.

In previous simulations the Young's modulus of Al-Si alloy was chosen between odd values, namely 17 GPa and 20 MPa. In engineering alloys the silicon content is below 12 wt%. These alloys have  $E \approx 75$  GPa.

Although the Slab model is unsuited for alloyed materials it gives the following values, for a mixture with 20% silicon:

$$E = 0.8 \times 70,000 + 0.2 \times 110,000 = 78,000 \text{ MPa}$$

This value is much closer to that of the engineering alloys than to the values used in previous models. However, the amount of silicon in the alloy has a gradient, which indicates that the layer should not be considered as homogeneous, both for mechanical and thermal properties. If this layer is used in the modelling of the metallisation process, the alloying of the aluminium and the silicon should be taken into account. Because of the difficulty in estimating the properties and the behaviour during the formation of the alloy, the entire layer is ignored in the thermal stress calculations.

### 5.3 Calculations of thermal stress

Silicon starts at room temperature as a  $156 \times 156 \text{ mm}^2$  wafer. At  $660 \text{ }^\circ\text{C}$  the wafer dimensions have increased. The elongation (or strain)

$$\varepsilon = a(T_1 - T_0) = 2.6 \cdot 10^{-6} \cdot (660 - 20), \quad 4.1$$

this give the new dimensions as  $156.26 \times 156.26 \text{ mm}^2$ .

The lengths of the two materials, are equal. Therefore equation 3.8 can be written as:

$$a_{Al} \Delta T + \frac{\sigma_{Al}}{E_{Al}} l = a_{Si} \Delta T + \frac{\sigma_{Si}}{E_{Si}} l, \quad 4.2$$

in which  $\Delta T$  is the temperature difference. Balance of forces requires  $\sigma_{Al} A_{Al} = -\sigma_{Si} A_{Si}$ . These equations lead to:

$$\sigma_{Al} = -K a_{Al} E_{Al} \Delta T A_{Al} \quad 4.3$$

$$\sigma_{Si} = -\sigma_{Al} \frac{A_{Al}}{A_{Si}}, \quad 4.4$$

where  $K$  is defined as:

$$K = \left(1 - \frac{a_{Si} \Delta T_{Si}}{a_{Al} \Delta T_{Al}}\right) / \left(1 + \frac{A_{Si} E_{Si}}{A_{Al} E_{Al}}\right) \quad 4.5$$

For aluminium of thickness 40 micron and the material properties calculated by the Slab model calculations have been made for the three wafer thicknesses. A tensile stress in the aluminium and a compressive stress in the silicon develops. As these materials are attached to each other, these stresses will most likely form gradients, with a similar state on the material boundary for both layers. The values are presented in table 7.

The stresses in the aluminium from the thermal stress calculations are used as input for Stoney's equation. A comparison between the cells of a different thickness can be made, without a strong match with the actual cell shapes.

Equation 3.12, results in an expression for the curvature  $R$

$$R = \frac{Et_{silicon}^2}{6\sigma(1-\nu)t_{aluminium}} \quad 4.6$$

It must be noted that  $\sigma$  is the stress on the outer surface of the silicon, which is assumed to be equal to that of the aluminium, in Stoney's equation. These results are included in table 7.

Thickness	Stress in silicon	Stress in aluminium	curvature based on stress in the aluminium
200 micron	126 MPa	628 MPa	37 $\mu\text{m}$
160 micron	154 MPa	615 MPa	24 $\mu\text{m}$
120 micron	198 MPa	595 MPa	14 $\mu\text{m}$

Table 7 Results of the thermal stress calculations for three cell thicknesses, as well as the curvatures calculated by Stoney's equation. The influence of the silver layer and the Al-Si alloy have been neglected.

It is interesting to note that the tensile stresses of aluminium and silicon are 90 MPa and 81,9 MPa respectively.<sup>33</sup> These values are much lower than the values predicted by the thermal calculations. The curvatures are also in strong disagreement with the measurements.

With this in mind the calculations can be applied the other way around. If the maximum height of the cells are used as input for Stoney's equation, the stress in the material could be calculated. Results of these calculations are shown in table 8.

Thickness	Radius of curvature	Stress in the aluminium layer
200 micron	1693 mm	13.8 MPa
160 micron	743 mm	20.2 MPa
120 micron	599 mm	14.1 MPa

Table 8 Results of the stress calculations, using the radius as input for Stoney's equation.

The radius of curvature is estimated from the curvature measurements in the following way: the height and half the length of the cell are used to determine angle  $\alpha$ . Half the distance between the highest and lowest point of the cell can be used in combination with angle  $\alpha$  to estimate the radius of curvature, which is indicated by the blue lines in figure 26.

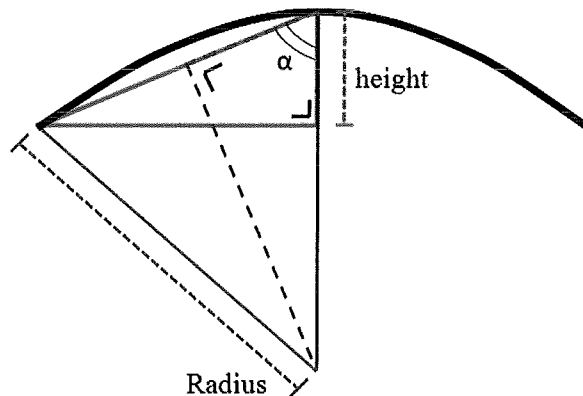


Figure 26. Sketch of the curvature estimation by two triangles.

The estimations of radii are shown in table 8. Fortunately the amount of stress calculated from the curvature are more realistic than the curvatures calculated using the thermal stress approach. The order of magnitude is sensible, as it does not exceed the tensile strength of the aluminium.

A problem with the estimation of the radius from curvature measurements is it that a circle does not truly describe the shape of the cell. The magnitude for stress for different wafer thicknesses, could still be approximated, despite of the difference between a true radius and the actual shape of bending. This is not the only approximation: the calculations are on the edge of the requirements to apply Stoney's equation, which could have a strong influence.

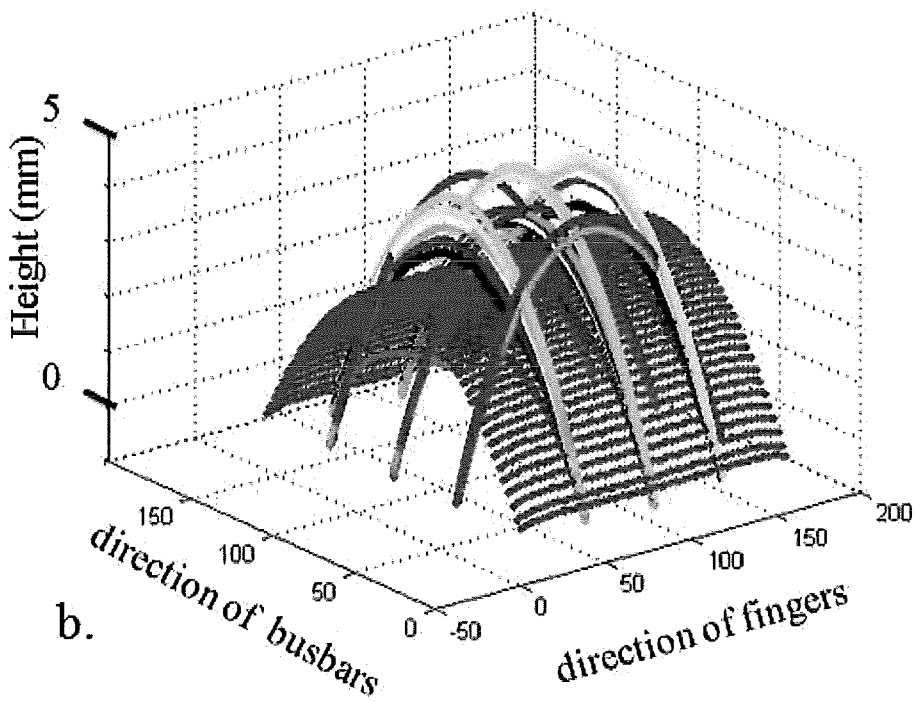
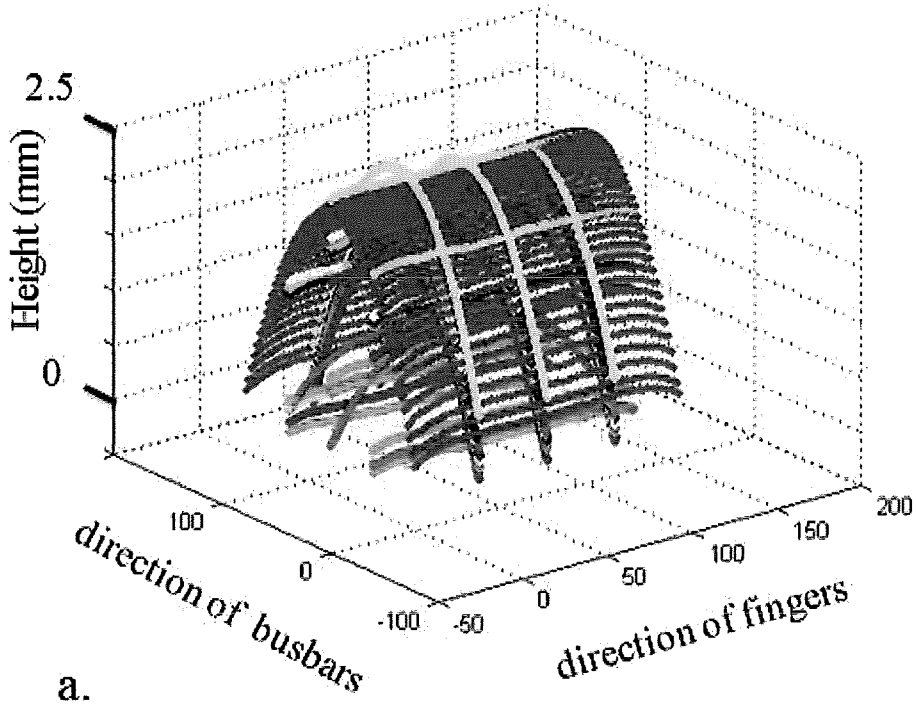
The results of the thermal stress and curvature calculations will be compared to the results from the finite element modelling in net next section.

## 5.4 Modelling

In figure 27 the digital experiment is displayed in blue lines (which indicate the silver-pattern). The silver side is on the top and the aluminium is at the bottom in this representation. The lines with different colours are curvature measurements. The stresses estimated for the most outer fibre of the silicon are in the order of 50 MPa

The accuracy of the model varies with the thickness of the silicon; however it seems to be in the right order of magnitude.

Similar digital experiments have been executed with both varying aluminium and silicon thickness. These agree with the trend, that with increase in the ratio between the thickness of aluminium and the thickness of silicon, the bowing increases.



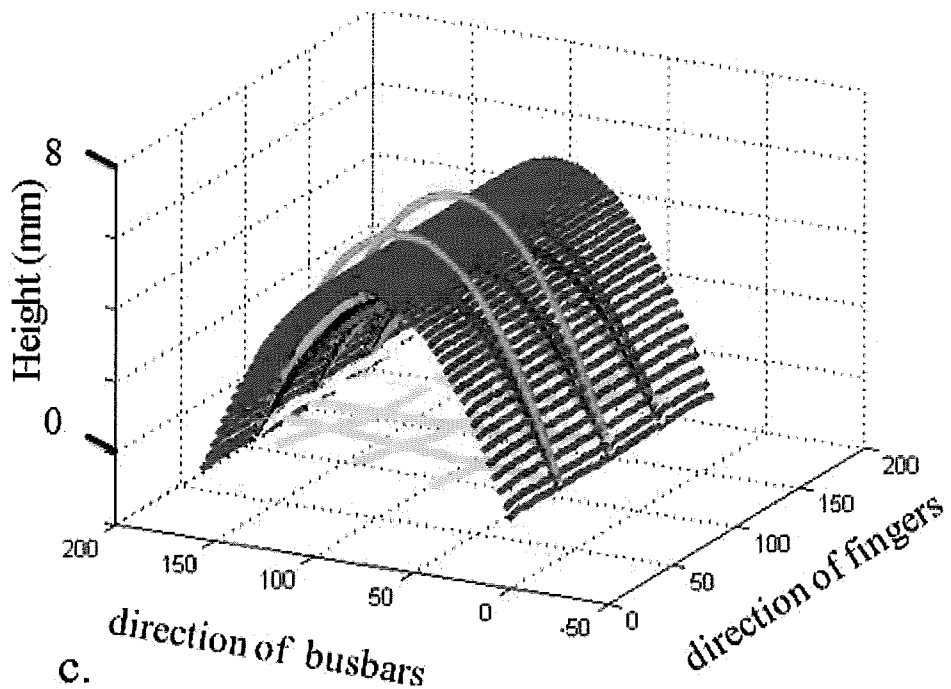


Figure 27 a, b, c. Results from the curvature measurements combined with the results from the computer simulations (represented by the blue grid).

## 5.5 Discussion

A serious difference in the mechanical state of the cells between process steps can be observed. Especially after the firing step severe distortions are observed. Thinner cells are more sensitive to bending, they require less stress to induce the same amount of bending than thicker cells. According to the thermal calculations, the stress in the silicon wafer due to metallisation must be greater for thinner wafers. Curvature measurements show that the maximum height of a 120 cell is approximately three times that of a 200 micron cell.

From the estimates used in the thermal stress calculations, the stresses in the aluminium should be around 600 MPa, which is completely unreasonable. The ways in which the material properties of this layer were estimated are probably insufficient to make a sound prediction. The formula's that were used are also very rough estimations.

The calculated stress for 200 micron cells, based on measured curvature, is in the right order of magnitude, being below the fracture stress of silicon. For the 120 micron cells, the same curvature gives much lower values for stress, but due to the increase in radius the stresses are in the same order of magnitude. It is interesting to note that the

thermal stress calculation, gives stresses for all three thicknesses to be close together, although the order of magnitude is incorrect. The values could be underestimated by Stoney's equation, most likely because the thin film criterion is not met. Indeed the values are lower than those of the modelling results. Neither of the results are close to the fracture strength of the silicon. The 50% loss in the production of the 120 micron cells could explain if the stresses were in the range of the fracture strength. The silver H-pattern is ignored in the simple estimate, this could lead to additional stress in the thermal stress calculations (which would be even farther from reality), but it could also lead to a reduction of the bowing of the wafers. If silver layer reduces the bowing, then the stresses calculated from the curvatures are too small, because these only include the influence of the aluminium layer. The computer simulations include both layers, the results are in a similar of magnitude as the stresses calculated from the curvatures.

Deformations could be occurring in the metallisation layers only, leaving the silicon elastically deformed between the silver and aluminium layers. The stresses could be undone by flattening the cell before soldering or lamination. If silicon is assumed to be brittle (and not plastically deformed) this representation should hold. However, the processing temperature extends beyond the ductile-brittle transition temperature of the material. The solidification of silver occurs above the ductile-brittle transition temperature of silicon. The aluminium solidification occurs below it. The degree of plastic and elastic deformation could be estimated by the solidification temperatures. The influence of the silver grid is then assumed to be limited to pure plastic deformation. The elastic deformation of the silicon is assumed to be caused by the aluminium layer. This idea supports the experience of cell manufacturers. Producing cells with open undersides reduces the extend of bowing.

More accurate characterisation of the mechanical properties of the layers and the exact sizes of the layers (also for the different process settings) are required. Including all information could lead to an over-complicated model, but the predictive possibilities of future models are largely dependent on this knowledge.

## Chapter 6 Theory concerning fracture

### 6.1 Introduction

In the previous chapter the focus was on the influence of different process steps on the stress state. In this part of the report, an attempt is made to elaborate on these influences. Based on these processing steps, the basics of fracture mechanics, acoustic emission and fracture will be examined as well as.

### 6.2 Fracture mechanics

Fracture mechanics is a quantitative analysis for evaluating structural behaviour in terms of applied stress, crack length, and specimen geometry. This field can be divided into several sections. The first is linear elastic fracture mechanics (LEFM). LEFM assumes that the material is isotropic and linearly elastic. Based on this assumption, the stress field near the crack tip is calculated using the theory of elasticity. Since the stresses at the crack tip reach to infinity, parameters  $K$  and  $G$  are developed to indicate the critical applied stress level, at which the crack will grow.  $K$  and  $G$  will be discussed in the next paragraph. LEFM is valid only when the inelastic deformation is small compared to the size of the crack; small-scale yielding. If large zones of plastic deformation develop before the crack grows, Elastic Plastic Fracture Mechanics (EPFM) must be used.<sup>53</sup>

EPFM is the second description of fracture behaviour. This is a variation on the LEFM concepts made to cope with increased amounts of plasticity in the crack tip region. EPFM assumes isotropic and elastic-plastic material behaviour. One of the

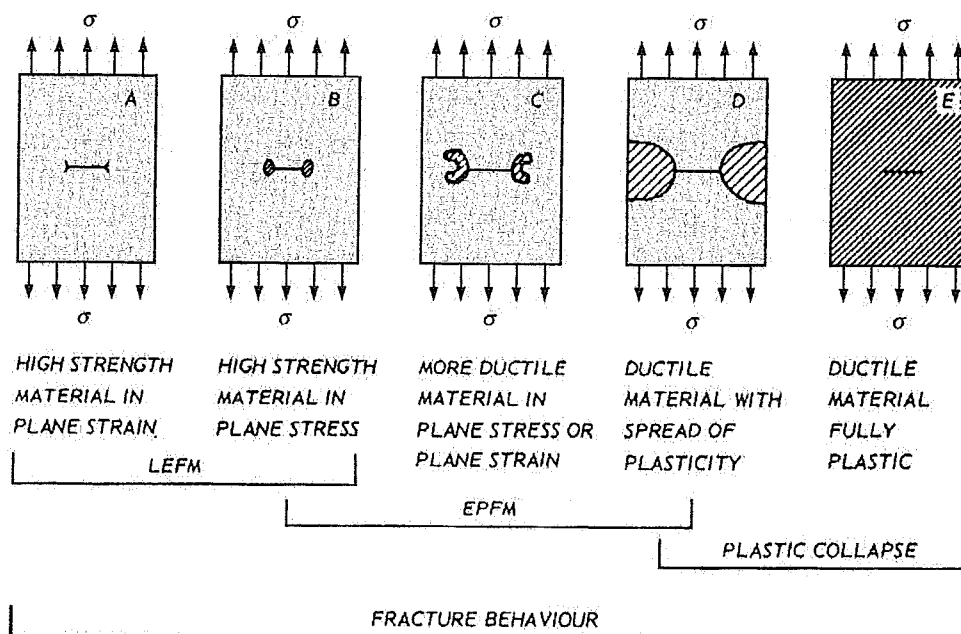


Figure 28. Overview of application area for different FM techniques.

parameters that can be used is the opening displacement at the crack tip. When this opening exceeds a critical value, the crack will grow.

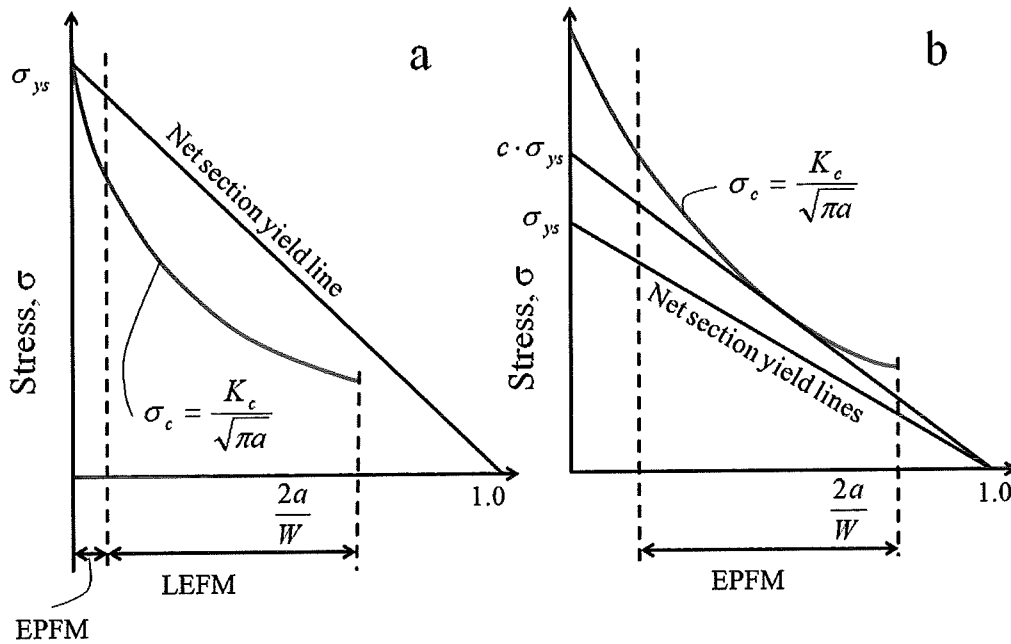


Figure 29. Comparison of residual strength diagrams for (a) relatively brittle and (b) relatively ductile materials.

LEFM can be applied when the nonlinear deformation of the material is confined to a small region near the crack tip, as is shown in figure 28. For brittle materials, it accurately establishes the criteria for catastrophic failure. However, limitations arise when large regions of the material are subject to plastic deformation before a crack propagates (see figure 29). Elastic Plastic Fracture Mechanics (EPFM) is proposed to analyse cases with large plastic zones, relative to the crack length. Note that for very short cracks in relatively brittle materials the plastic zone size is no longer relatively small, in these cases EPFM will have to be used also.<sup>54</sup>

### 6.2.1 Griffith and Irwin

Griffith formulated his theory of brittle fracture (in 1920), which is known as the Griffith Energy Balance Approach, using elastic strain energy concepts. If a crack is present in the material, in the area close to the crack flanks the stress will decrease. Inglis (1913) showed that for an infinite plate the elastic energy change due to a crack is  $U_a$  with  $\sigma$  as the applied stress,  $a$  as half the crack length and  $E$  is the Young's modulus.

$$U_a = -\frac{\pi\sigma^2 a^2}{E} \quad 6.1$$

The introduction of a crack is assumed to require energy to create a crack surface area.

$$U_\gamma = 4a\gamma_e \quad 6.2$$

From this basis an energy balance can be constructed. The equation basically state that a crack will propagate when the increase in the surface energy is less than the loss of strain energy. This is considered to be the primary equation to describe brittle fracture. Using the energy balance a criterion for crack extension can be obtained.

$$\frac{\pi\sigma^2 a}{E} > 2\gamma_e \quad 6.3$$

Irwin designated the energy release rate  $G$ , which is energy available per unit crack extension.  $R$  is the crack resistance, which represents the surface energy increase mentioned earlier. From the crack extension criterion it follows that  $G$  must exceed  $R$  for a crack to grow.

$$G = \frac{\pi\sigma^2 a}{E} > G_c = R = 2\gamma_e \quad 6.4$$

$G_c$  can be determined by measuring the critical stress for a specific crack size, or by measuring the critical crack size for a loaded plate. Irwin continued his work by developing the stress intensity approach. The stress intensity factor  $K$  is a measure for the magnitude of the elastic stress field:  $K = \sigma\sqrt{\pi a} * f(a/W)$ , where  $f(a/W)$  is a dimensionless parameter that depends on the geometries of the specimen and crack. For an infinitely large plate with a central crack of length  $2a$ ,  $K = \sigma\sqrt{\pi a}$ . In terms of  $K$ , the criterion for crack extension becomes:  $K = \sigma\sqrt{\pi a} > K_c$ . For tensile loading  $G_c$  and  $K_c$  are related.

$$G_c = \frac{K_c^2}{E} \quad 6.5$$

Linear-elastic fracture mechanics can only be applied if only limited plasticity is involved. Silicon is a brittle material, thus this theory can be applied to silicon. Probably this model is not suited for aluminium and silver, which are considered rather ductile materials. However for the solar cell as a whole, it might be suited if the silicon behaves as the “weakest link”.

### 6.3 Surface roughness

The sawing process damages the wafer locally across the surface and at the edges by the formation of cracks in the micrometer range. These microcracks reduce the fracture strength of the wafers considerably. Details of the sawing process and evidence of microcracks are recorder by Möller et al.<sup>37</sup>

The original roughness of the wafer is a consequence of the cutting process. The surface roughness of the silicon in later steps originates from the saw damage removal (ECN-clean) that is achieved by etching. After this step, no microcracks have been observed in the wafer. This does not mean that their presence is excluded, but even if they are not eliminated, the amount of microcracks are considerably reduced. The

ECN-clean not only has the purpose of damage removal, but also to create a surface roughness to reduce light reflections.

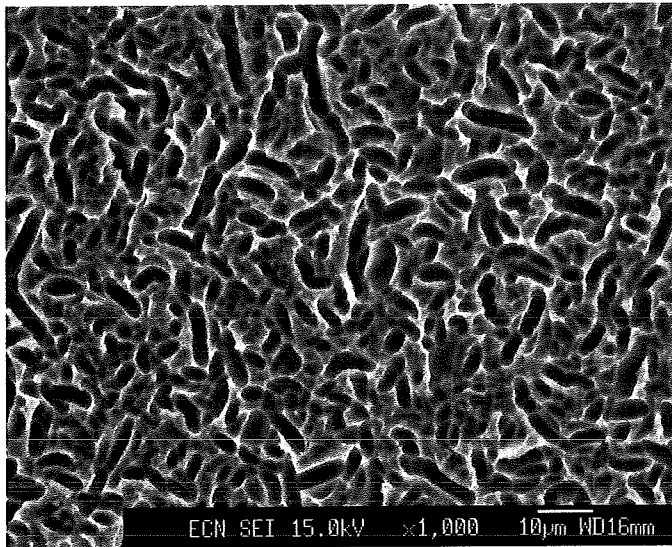


Figure 30. SEM scan of silicon surfaces after ECN clean.

Intermediate cleaning steps in the following processing steps include several etchings. Due to these etches, as well as the ECN-clean, the surface of the grains is not the only thing affected; etching often causes preferential influence around the grain boundaries. Surface roughness can be translated into the LEFM as an initial crack. In combination with the localised etching at grain boundaries a simple calculation should predict the behaviour of the silicon wafer accurately. By using the wafer roughness as input for LEFM, an estimate of the strength of the wafers has been made by Coletti<sup>54</sup> on wafers with different etch treatments. Unfortunately the calculations do not agree with the measured values acquired in the experiments that accompanied the calculations. In the experiments, fracture occurs at lower stresses than the calculation predicts. A reason for this could be the size of the surface cracks that are considered in the calculations. Of course the wafers are still suitable for comparison purposes rather than determinations of material properties. The research showed that wafers with the ECN clean treatment show an improved mechanical stability.

### 6.3.1 Measurements

Both optical microscopy and scanning electron microscopy can show surfaces. By making a section, the different layers can be seen. The Sensofar scanning confocal microscope of ECN is equipped with software and an apparatus to create both line scans and 3D images of the specimen surface. With this equipment the shape and size of the silver lines of the H-pattern can also be documented.

### 6.3.2 Results

The surface of the silicon, as observed by the confocal microscope of ECN, is shown in figure 30. The surface is irregular, as is confirmed by the line scan in figure 31. Scratches that are made in silicon to initiate cracking have sizes between 6 to 250  $\mu\text{m}$  for nanocleavage to microcleavage respectively.<sup>55 56</sup> The “valleys” measured here are

up to  $4\ \mu\text{m}$ , so they are still smaller than those used to induce cracks in brittle semiconductors.

A line scan was made of a silver finger. The height of the finger is  $15\ \mu\text{m}$ , with a width of  $110\ \mu\text{m}$ , approximately. For a better grasp of this geometry a 3D scan has been included below the line scan.

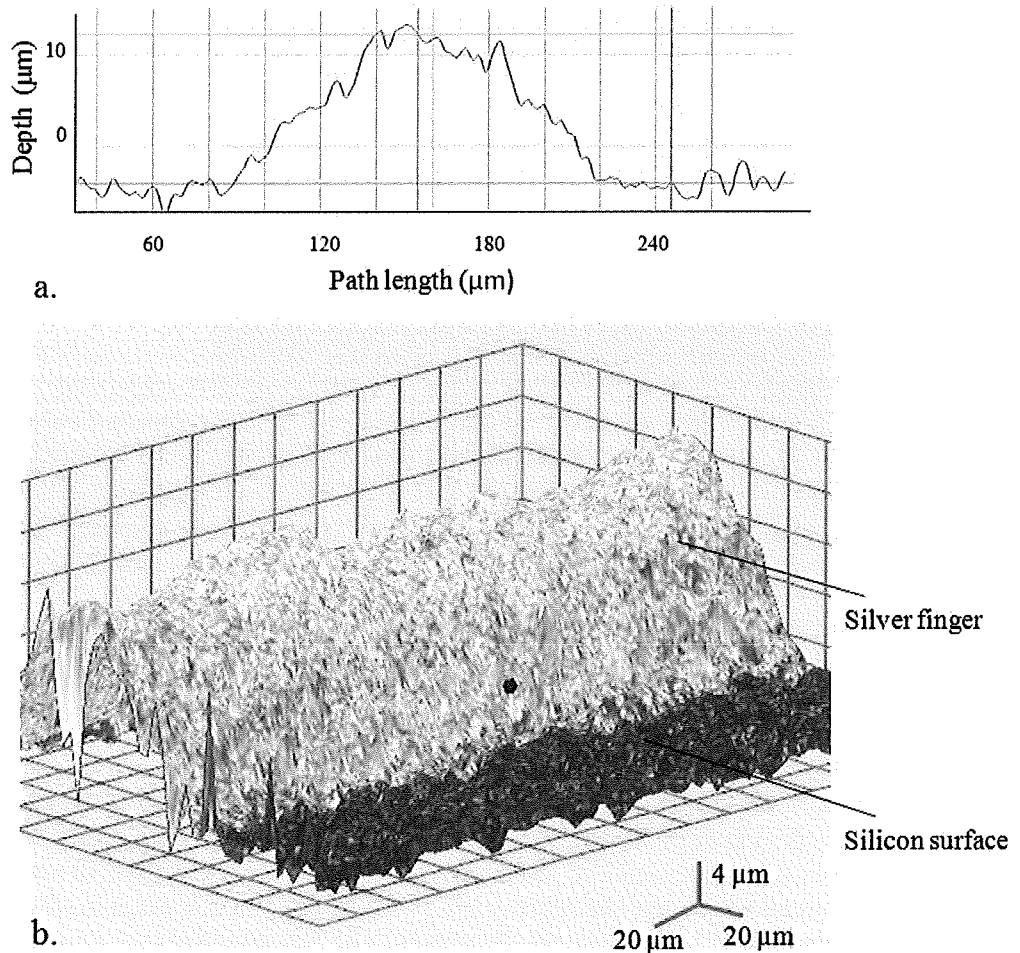


Figure 31. A confocal microscope line scan and 3D plot of a silicon cell with silver finger.

The value for fracture toughness  $K_{Ic}$  is  $0.91\ \text{MPa}\times\text{m}^{0.5}$ . This value is the average of the two values give in section 3.1. The length of the “valleys” as a measure for initial crack length. The fracture toughness combined with the crack length and formula’s 6.4 and 6.5 from the previous section, can give a fracture stress for the silicon. The critical stress for this roughness is  $229\ \text{MPa}$  if a single edge notched plate geometry<sup>54</sup> is assumed. The geometry of the set-up used to induce fracture (described in section 7.1) has a stronger resemblance to a single edge notched bend specimen geometry.<sup>54</sup> This geometry gives a critical force in the order of  $0.01\ \text{N}$ .

## 6.4 Acoustic emission

The term acoustic emission (AE) is used to describe both a technique and the phenomenon upon which the technique is based. If there is a sudden release of energy within a solid, caused for instance by the growth of a crack, then some of the energy is dissipated in the form of elastic waves. Of course part of that energy is released in the form of heat. This depends on the nature of the source, how localised it is and how rapidly the release takes place. Localised, rapid energy releases give rise to elastic waves in the ultrasonic frequency regime that can be detected by microphones or transducers attached to the surface of the specimen provided the waves are of sufficient amplitude.<sup>57</sup> In the solar cell industry, strings of cells are checked for initial cracks by manufacturers. This suggests that the initiation and propagation of cracks can be detected by acoustic emission, not the presence of “still” cracks.

Detection of cracks by transducers is currently used in the investigation of defect growth, crack advance, plastic deformation, inclusion or precipitate fracture, and disbonding of coatings, crystallographic phase transformations, melting or solidification, thermo-elastic effects and friction between surfaces. AE is used for monitoring of fabrication processes such as welding noise (including defects), rolling, forging etc..

Acoustic signals can be induced by many different events. Therefore it is important to know what to listen for. Often the number of acoustic events and the amplitude of the signal is examined,<sup>58</sup> but also the power and the frequency. Interpretation of these signal properties is problematic, and often assisted by other techniques, such as fractographic studies. In general the shape of the time-amplitude graph can be used to discriminate the occurrence of fracture, as is shown in figure 32.<sup>59</sup>

Source location is considered one of the main advantages of AE. If two sensors are at different distances from a source, the time it takes for the signal to arrive at the

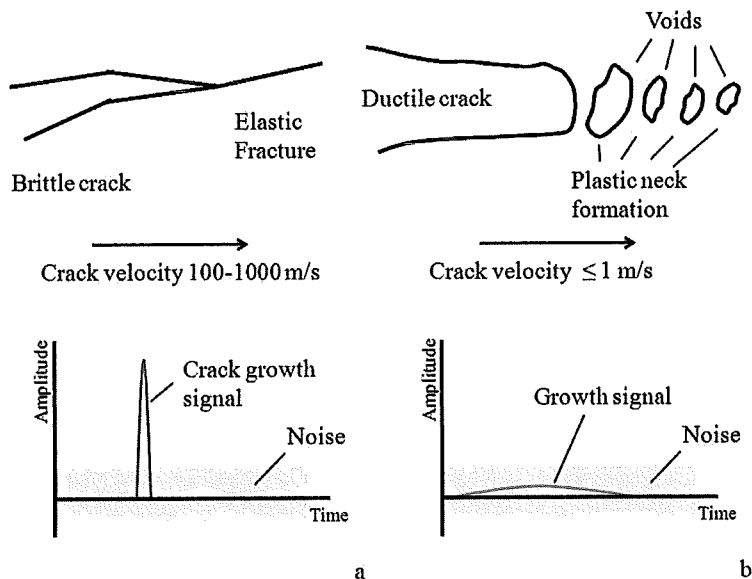


Figure 32. Drawing of (a) a fast brittle crack advancing (creating a detectable emission signal) and (b) a slow ductile loading (which could be undetectable).<sup>57</sup>

sensors will also be different. By measuring this difference, the area where the source events takes place can be determined.<sup>60</sup>

Other methods for crack detection include electroluminescence (which does not detect microcracks) and other acoustic techniques which discriminate by the alteration of a signal as it travels through the sample, rather than collecting signals produced by the sample itself.<sup>61</sup>

## 6.5 Brittle fracture, cleavage and fracture surfaces

The fracture of silicon could be best analysed by considering single crystal materials. The grain size in the wafer is rather large, especially considering the thickness of the material, making the propagation of the crack only slightly dependent on the grain boundaries it encounters. In the case of brittle fracture, the tip will be atomically sharp and the crack moves by breaking individual bonds between atoms.

Pérez and Gumbsch<sup>62</sup> have shown that if an initial crack is present along the  $\langle \bar{1}10 \rangle$  direction, that cracks propagate easily on (111) and (110) planes. With this in mind it is likely that the crack will alter direction at the grain boundary, choosing to propagate in a specific direction, the path which requires the least amount of energy.

As a crack propagates in a brittle material such as silicon, the energy is primarily released as surface energy. Since silicon has a diamond cubic structure, the crystallographic planes having the lowest surface energy are the (111) planes. Fracture should theoretically occur by cleavage along those planes. However, the loading geometry and boundary conditions can cause secondary cleavage planes to be activated, thereby increasing the complexity of the fracture surface as is demonstrated by Wilson *et al.* in experiments with micro cantilever silicon beams.<sup>63 57</sup> Models have been made concerning cleavage and controlled crack growth on brittle semiconductors with nanoscratches.<sup>56</sup> This research shows that for specific loading conditions the surface cracks determine the onset of crack propagation by linear elastic fracture mechanics (LEFM), which will be discussed further in section 8.4.

Fracture surfaces of brittle fracture can display information concerning the crack growth that has occurred. Investigation by atomic force microscopy shows that for low fracture energies the fracture surface is atomically flat, while at higher energies the surface has distinct features.<sup>49</sup>

The solar cells consist of “sintered” metals and multi crystalline silicon. For the electrical properties, a large grain size in the silicon is demanded. The material is cast in large ingots, which are slowly cooled to create these large grains.<sup>64</sup> It is important to note is that the cast structure of the ingot is not homogeneous. Around the outer surfaces and through the length of the ingot, impurity levels, grain size and grain distributions may vary. The crystallisation process of the materials is responsible for the development of different defect structures, which determine and limit the solar cell efficiency. The crystallographic orientation of the grain is not fixed, as it is in mono-crystalline wafers. This is important because silicon has preferential fracture planes.

## Chapter 7 Experiments concerning fracture

This chapter describes the experimental work concerning fracture. The experiments describe in the chapter are the four point bending test and acoustic emission measurements. The fractures induced by the four point bending are examined by optical and electron microscopy. The results from the fracture, acoustic and microscopy experiments are presented in chapter 8.

### 7.1 Four point bending

Comparing the different processing steps can be done by curvature measurements, and also by examining at what force (or displacement) fracture of the wafer occurs. Because the cells are bent before soldering, it is interesting to know what magnitude of force is needed to flatten the cell during or before soldering or lamination.

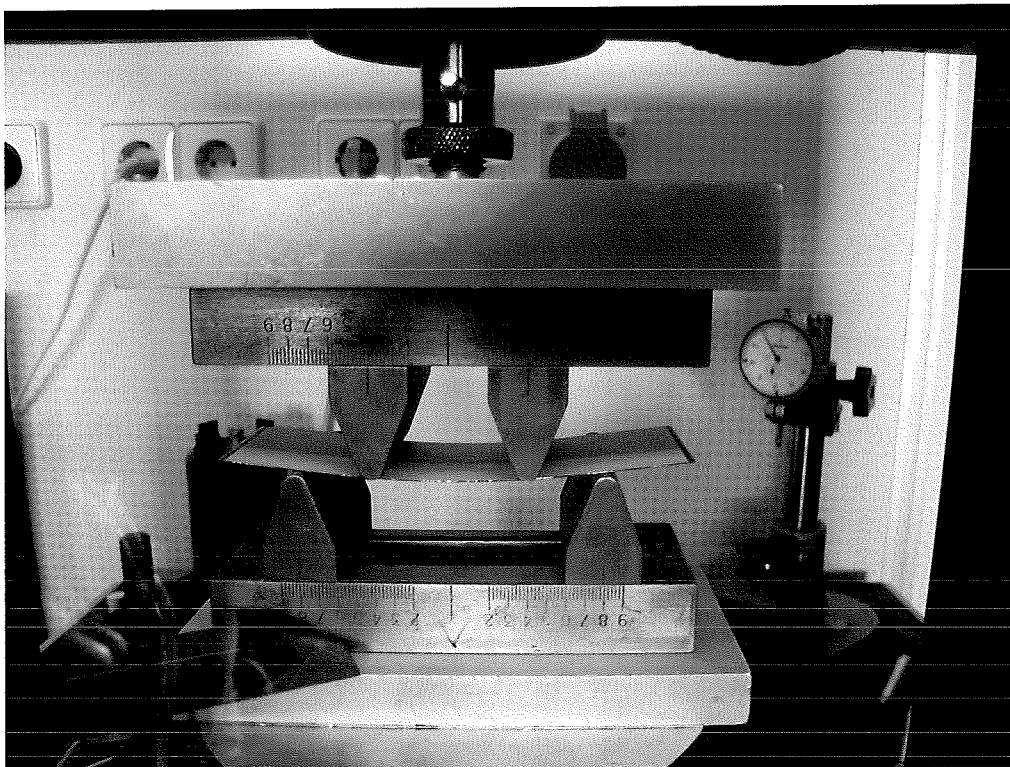


Figure 33. The four point bending set up with a sample placed up-side-down.

Mechanical strength measurements of poly-crystalline Si wafers have been carried out using a ring-on-ring test geometry by Coletti *et.al.*<sup>55</sup> These measurements were originally taken to compare the mechanical impact of surface treatments. Surface treatments were shown to have a great influence on the damage present on the wafers. Various bending test facilities have been considered to study the bending strength of wafers, figure 33 shows the set-up that was used in the present work. During the tests the applied forces and the displacements are recorded. From this the outer fibre stress and strain follows and material properties, such as Young's modulus and bending

strength, can be calculated. In the four point bending the force and displacements of the rods are registered. The fracture stress and strain can be calculated from these values by the following formula's, based on the ASTM C 1341-00 norm for this step-up:

$$\sigma = \frac{3Fl}{4wt^2} \quad 7.1$$

$$\sigma = \frac{48 \cdot td}{11 \cdot l^2} \quad 7.2$$

In these equation  $F$  is the force,  $w$  is the width of the sample,  $t$  is the thickness of the sample,  $l$  is the distance between the lower rods and  $d$  is the displacement of the upper rods.

Unfortunately it is still difficult to determine the stress distribution in the wafer (especially during the production steps). By creating a larger area with a similar stress state, mechanical weaknesses within that area can be localised. In addition testing to fracture can be used to determine the sensitivity to fracture of the wafers or cells after process steps.

Initially, tests were tried out on samples of 125 x 40 mm<sup>2</sup>. The samples had a complete busbar facing down and were cut halfway through using a laser, and subsequently snapped. This was done to see if the machine was suited for the experiment and if the data was not too diverse. The load cell used has a capacity of 100 kN. Fortunately the output is stable up to 0.01 N. The velocity of the machine was set as a constant and the displacement was recorded and stable to at least 0.01 mm.

The first two feasibility runs were done with a speed of 0.1 mm/minute, the remaining tests were done at 0.2 mm/minute. The results are shown in figure 34. The test results show some spread in the amount of bending and stress before fracture, but the order of magnitude is the same for all samples. The values for fracture stress and strain from the feasibility runs are included in figure 34.

The cells at several different processing steps were subsequently tested at a rate of 0.2 mm/minute. The tested groups of cells are described in section 2.1.1. In addition to these samples, three mono-crystalline silicon wafers were subjected to the same test.

A high speed camera was used to monitor a few samples of different process steps. The hope existed that perhaps some preliminary cracking could be observed during these recordings. No damage could be seen before the wafer or cell completely breaks.

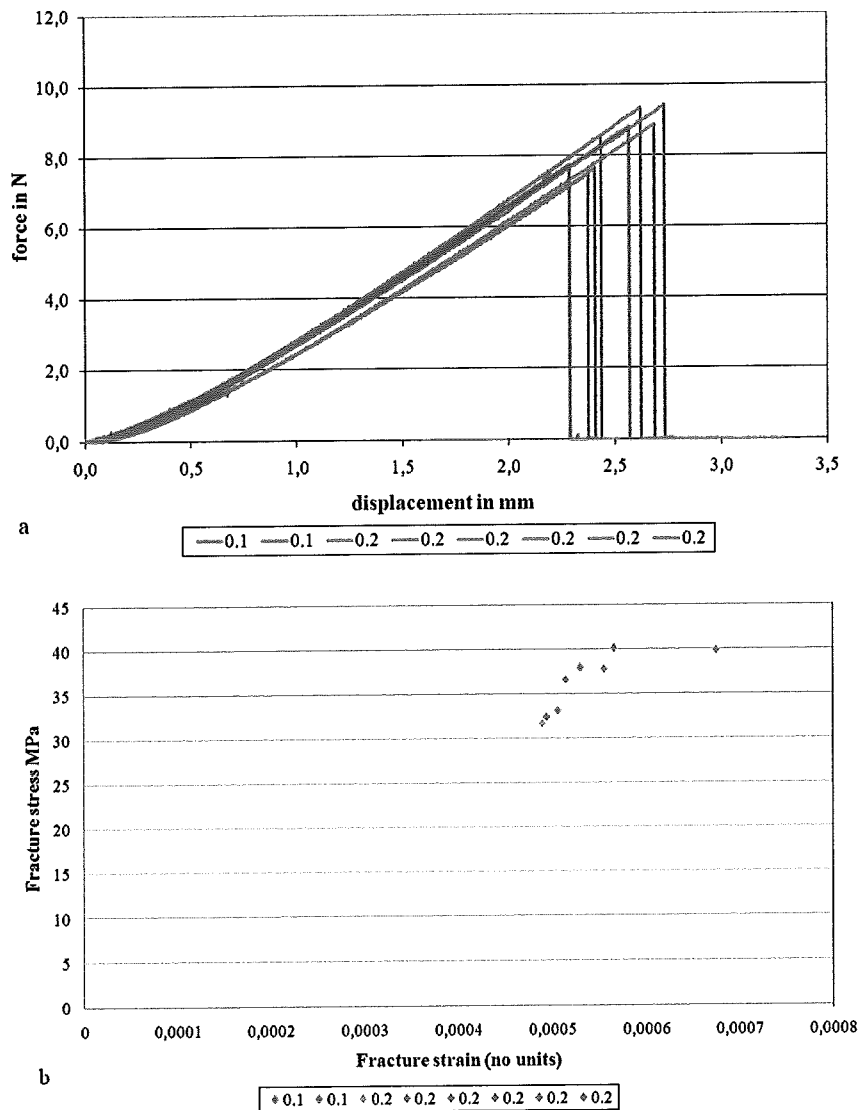


Figure 34. The results of the four point bending feasibility runs taken at 2 different velocities, 0.1 mm/minute for the red lines and 0.2 mm/minute for the blue lines. a) The force and displacement during the test. b) The values for the fracture stress and strain.

## 7.2 Acoustic emission

Acoustic emission measurements were taken during the four point bending experiment and the soldering process. Details about the experiments are discussed below and the results are presented in the next chapter.

### 7.2.1 Four point bending

Acoustic sensors were placed on the rods (which press down the wafers) to measure the emission, during four point bending. An amplification of 60 dB and an entrance

threshold of 50 dB were applied. During four point bending it is already obvious when complete fracture occurs; the acoustic emission is there to see if microcracking precedes the mechanical failure of the cell. To ensure a good connection between the metal surface and the sensors, a wax-type coupling gel was used between these surfaces.

### **7.2.2 Soldering**

For the soldering experiments, acoustic sensors were placed directly upon the cell to measure the acoustic emission. The signal is used to determine if fracture occurs during soldering, and if so, at which stage of the soldering process. The cell remains cold enough to touch, no heating effects of the sample or the sensor gel are taken into account.

For the solar cell soldering the ECN set-up was used. The soldering procedure starts with the positioning of the solder tip, this presses down onto the cell and tab from the top. The solder tip is heated to 320 °C and is kept at approximately this temperature for 1.4 seconds, after which the cell is released. The solder tip is a cylinder with a 2.3 mm diameter.

To determine whether sound is generated in the tab, instead of the cell, additional experiments were done. The first was soldering without placing the tab. This process was executed in exactly the same way as the other solar cells. If a signal occurred during this process, it must have been from either the solder tip or the solar cell, and not from the tab. In a second experiment the solar cell was replaced by a copper plate of 300 micron. For the copper plate soldering a handheld solder machine was used. This machine had a maximum temperature of 450 °C. The heating by this machine was slower (order of minutes rather than seconds) than the ECN set up. This way the signals that appear in the tab, and the solder could be examined independently of that of the solar cell.

## Chapter 8 Results concerning fracture

### 8.1 Four point bending

In all experiments groups of neighbouring cells have been used, as is explained in section 2.2.1. The points of fracture, induced by four point bending, show indeed a difference between groups of wafers from different blocks. Figure 35 illustrates the differences between block of a similar thickness. The blue and green markers indicate wafers of 200 micron and the red and orange markers wafers of 160 micron.

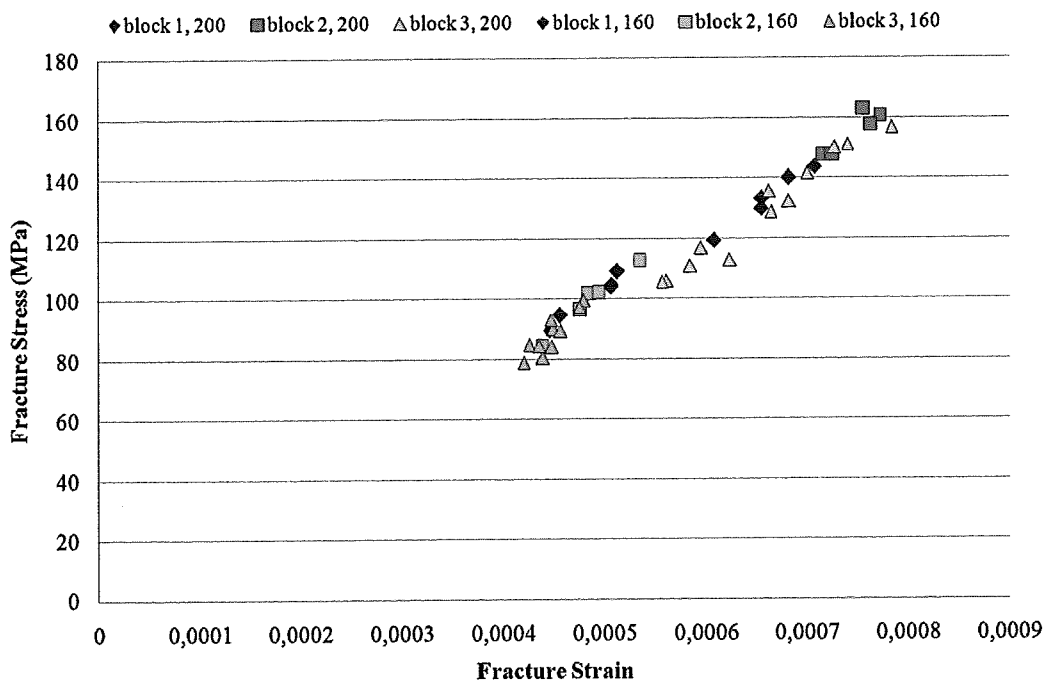


Figure 35. Stress strain plot of fracture points for clean wafers of 200 micron and 160 micron. Each group contains wafers from one separate block of the cast ingot.

The stress strain points are all approximately in one line. This indicates that the Young's moduli of wafers with a similar thickness are constant and independent of the block the wafers were cut from. It is obvious that the four point bending test cannot determine the Young's moduli for all the layers in the materials. The average of the Young's moduli for different wafer blocks is shown in table 9. Because the values for the Young's modulus are not in the same order of magnitude as the material constant for silicon, the ratio between stress and strain will be referred to as the experimental E. A difference in noticeable between fracture stress and strain for wafers from different thicknesses. A difference in the experimental E between thicknesses exists, but it is only slight.

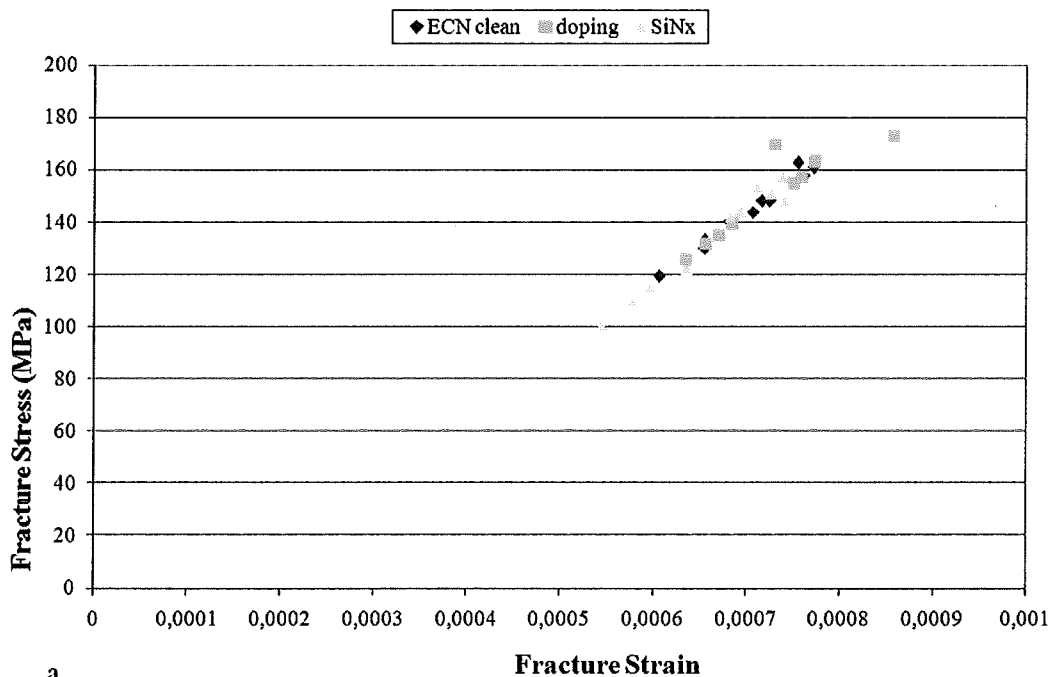
The different process steps can be compared by the four point bending. As the handling of the wafers and cells is a problem the fragility of the different stages is

important for a production line. Because of problems with the production of the samples, the complete solar cells are made of neighbours of “block 3” of figure 35.

The neighbours of blocks 1 and 2 are processed until two process steps, the doping and the silicon nitride deposition. As the curvature measurements already indicated, all processing steps preceding the metallisation have a minor influence on the mechanical state of the cell. In the following the results for 200 micron cells are shown as an example; the cells of other thicknesses showed similar behaviour. This is confirmed by the stress-strain plot in figure 36, in which the points of fracture are indicated. The relation between stress and strain is linear for all cases, therefore it is not included in the graph.

		experimental E (GPa)	standard deviation (GPa)
200 micron	block 1	201	3.471
ECN Clean	block 2	208	3.985
	block 3	195	7.673
	<b>complete group</b>	<b>200</b>	<b>8.027</b>
160 micron	block 1	206	3.829
ECN Clean	block 2	204	6.831
	block 3	196	8.293
	<b>complete group</b>	<b>201</b>	<b>8.386</b>
120 micron	block 1	219	38.444
ECN Clean	block 2	215	1.754
	block 3	200	4.619
	<b>complete group</b>	<b>208</b>	<b>19.538</b>

Table 9. Values of Youngs Modulus, calculated from the stress and strain values of the four point bending test, for clean wafers of 200, 160 and 120 micron. The values for the complete groups are calculated from the wafers of all three blocks.



a

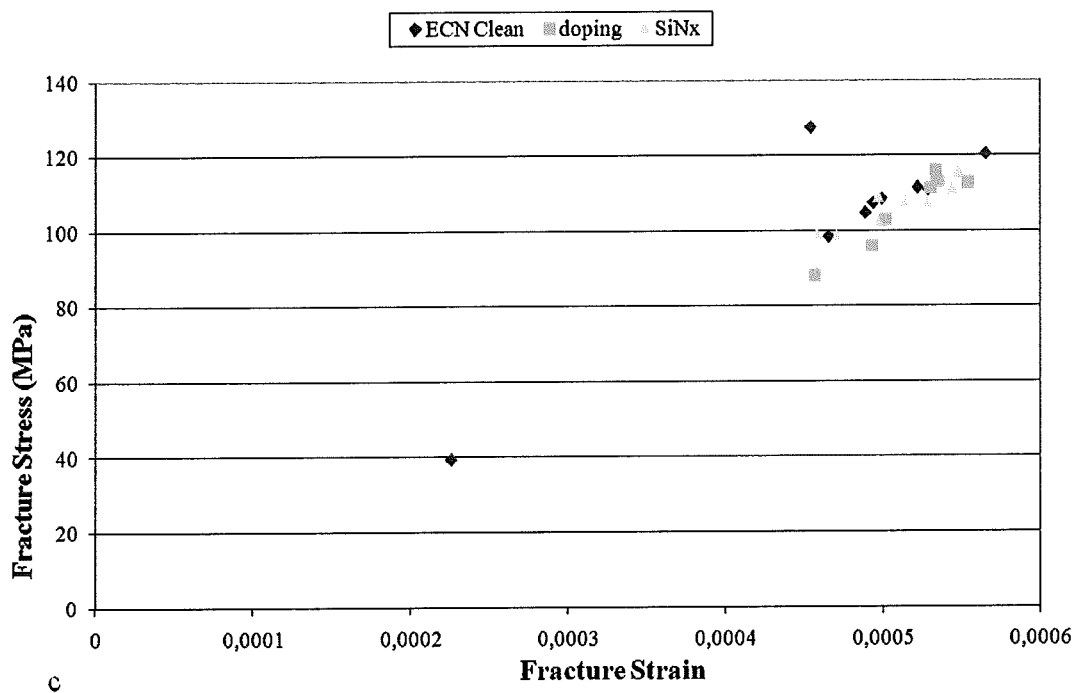
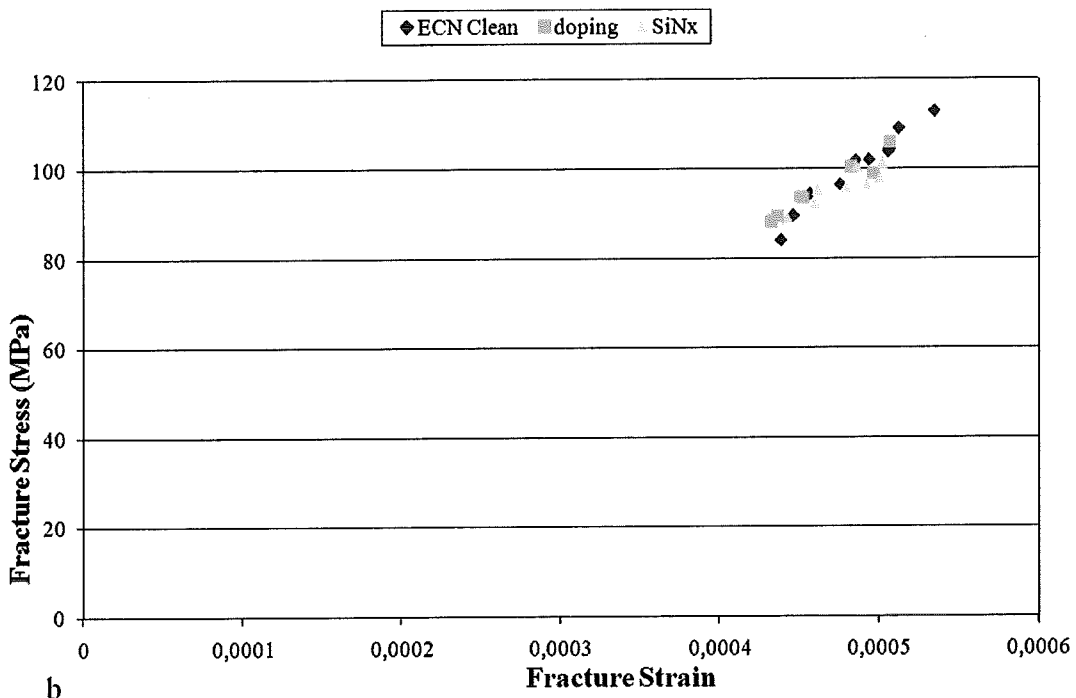


Figure 36. Stress strain plot of fracture points for 3 stages in the cell production: blue is ECN-clean, purple is after doping and yellow is after SiN<sub>x</sub> deposition. a) 200 micron wafers, b) 160 micron wafers and c) 120 micron wafers.

The blue symbols represent the wafers after the ECN-clean, the yellow symbols those before the silicon nitride deposition and the purple symbols are wafers with the silicon nitride.

Table 10 shows the experimental E for the consecutive process steps. For the experimental E of the 200 and 160 micron wafers (after ECN Clean), the averages of the three blocks are taken. The experimental E of block 3 varies from block 1 and 2 for 120 micron wafers, therefore the average of only block 1 and 2 is used in this comparison.

		experimental E (GPa)	standard deviation (GPa)
200 micron	After ECN Clean	205	5.090
	After doping	206	9.723
	After SiNx	201	10.365
160 micron	After ECN Clean	205	5.625
	After doping	205	3.169
	After SiNx	201	3.684
120 micron	After ECN Clean	217	25.740
	After doping	205	8.242
	After SiNx	209	4.757

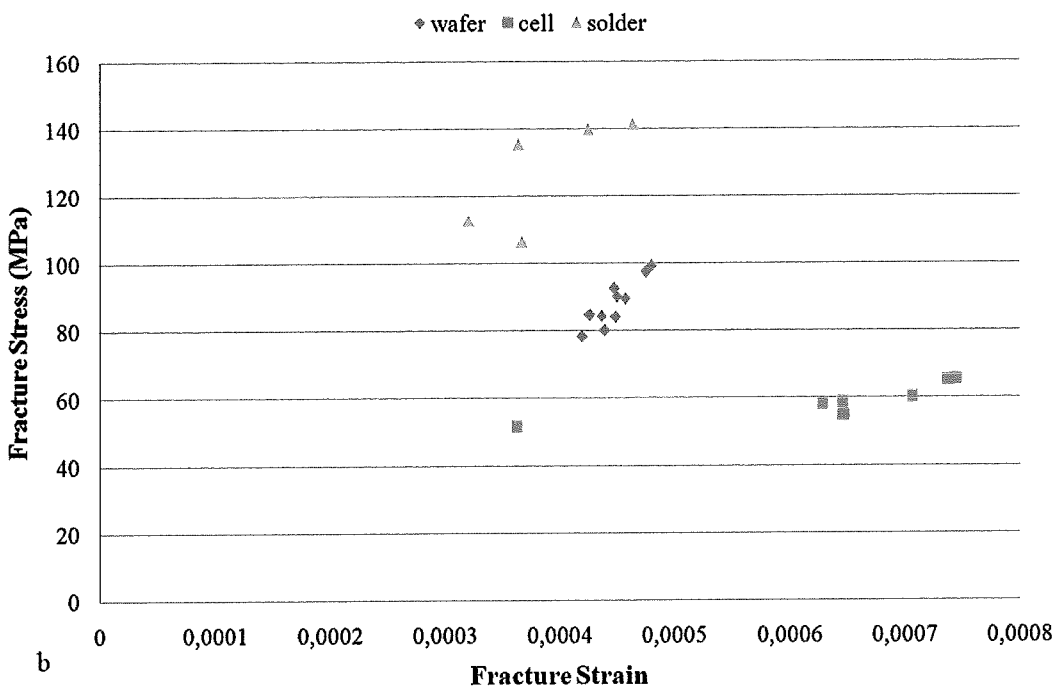
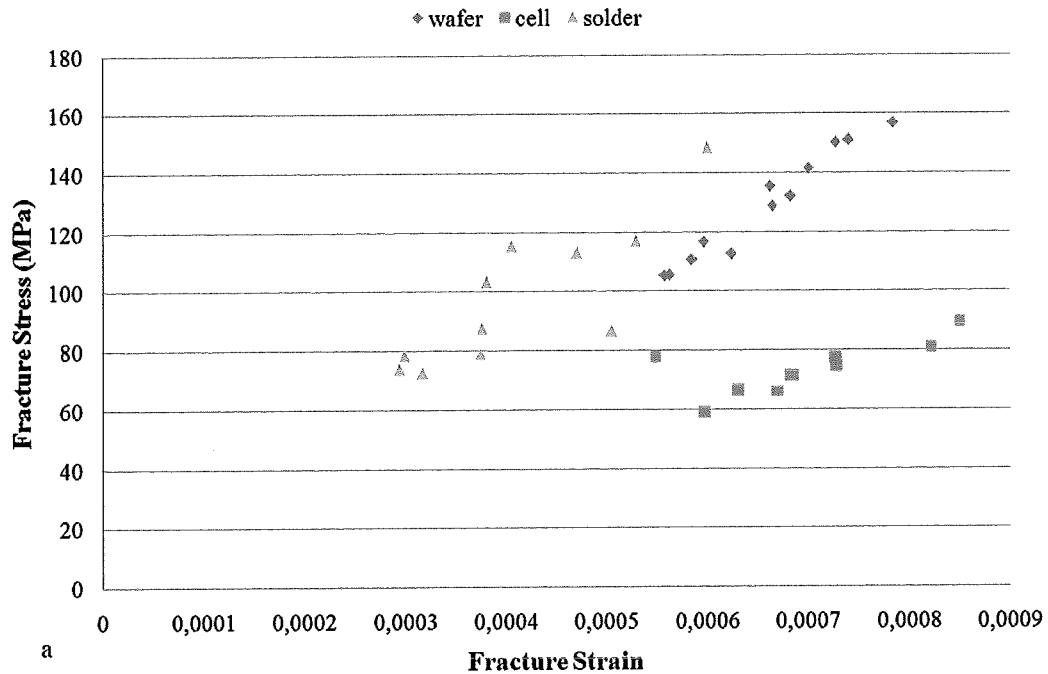
Table 10. Values of the experimental E for 200, 160 and 120 micron wafers, processed to three different stages. The measured wafers are neighbouring with the exception of the “After ECN Clean”-step for 160 and 200 micron.

The comparison of the cells at stages, “wafer after ECN-clean”, “complete cell”, and “after soldering” is shown in figure 37. The cells in these stages are neighbouring (indicated as block 3 in table 8). The moment of fracture of the cells after soldering is represented by green symbols, complete cells are red symbols and ECN-clean wafers are blue symbols. The strength of the wafer is reduced by the production steps that make it into a solar cell. The tabs themselves seem to strengthen the cells and increase the stiffness of the structure. The ratio between stress and strain of these stages is presented in table 11.

		experimental E (GPa)	standard deviation (GPa)
200 micron	After ECN Clean	195	7.673
	Complete cells	107	12.141
	After soldering	240	23.550
160 micron	After ECN Clean	196	8.293
	Complete cells	96	18.892
	After soldering	329	29.747
120 micron	After ECN Clean	200	4.619
	Complete cells	86	6.992
	After soldering	-	-

Table 11. Values of the experimental E for 200, 160 and 120 micron wafers, cells and soldered cells. The calculations only include cells and wafers without visible damage. The measured wafers are neighbouring with the exception of the “After ECN Clean”-step for 160 and 200 micron.

For the experimental E of the 120 micron wafers (after ECN Clean) only block 3, from table 8, is used. For the moduli of the 200 and 160 wafers the average of three blocks is used. In figure 37, soldered cells that had chips or small crack were included, in table 11 these are not included, this is why there are no values for 120 micron cells after soldering.



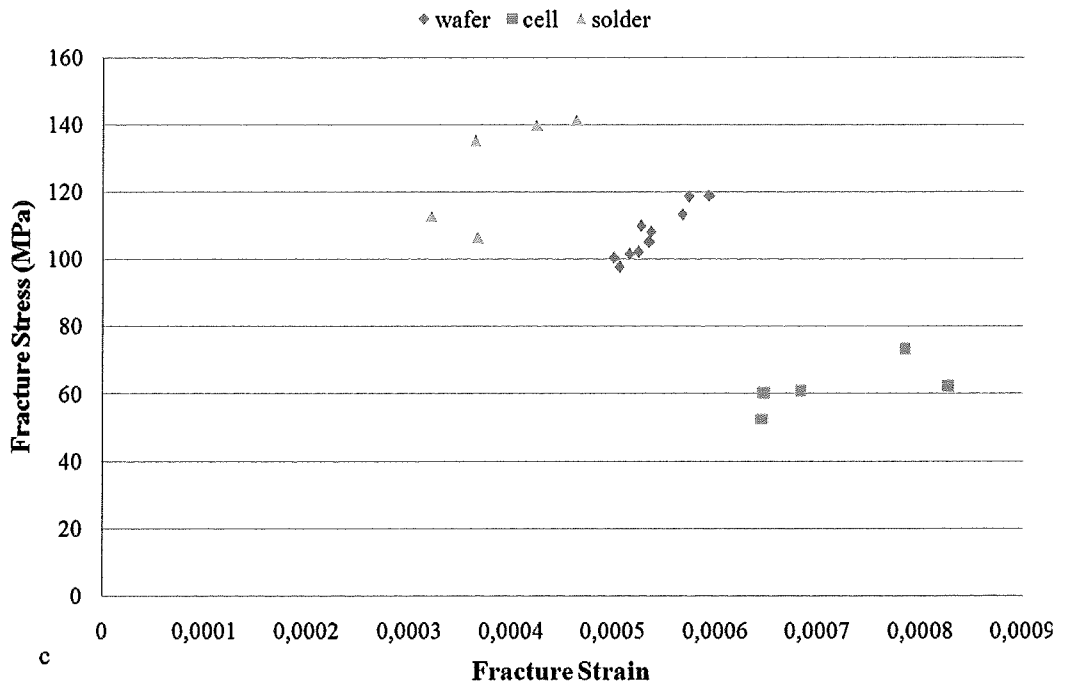


Figure 37. Stress strain plot of fracture points for 3 stages in the cell production: blue is ECN-clean, red is complete cell and green is after soldering. a) 200 micron cells, b) 160 micron cells, c) 120 micron cells.

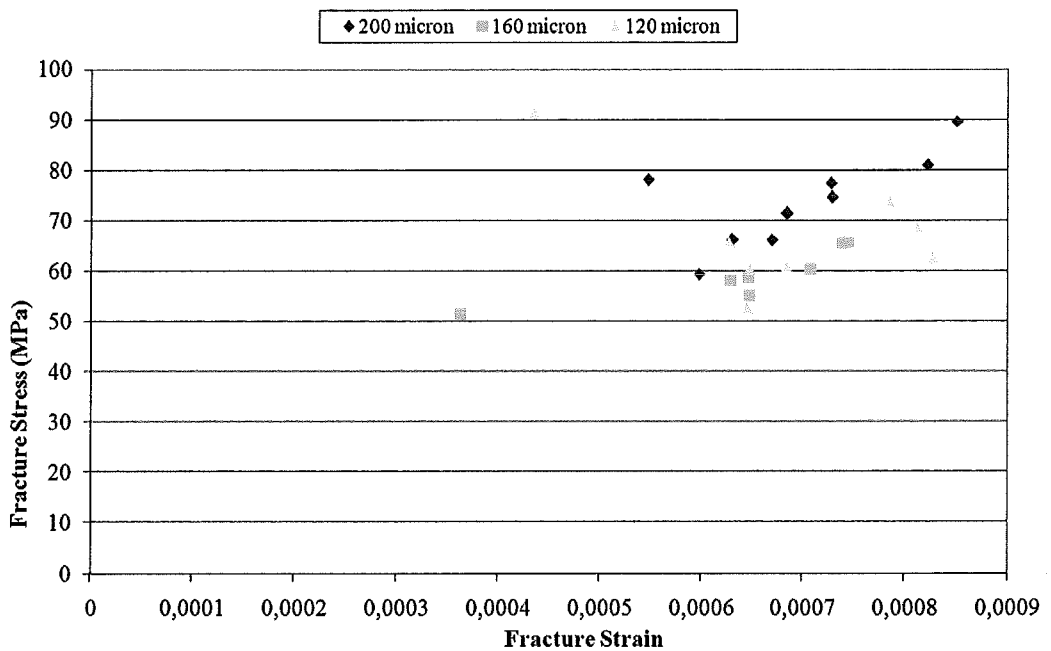


Figure 38. Stress strain plot of fracture points for complete cells of a different thickness, yellow is 120 micron, purple is 160 micron and blue is 200 micron.

Cells from the stages “ECN Clean”, “complete cell” and “soldered cell” show a stiffness that is specific for that stage in processing. These results are table 11 and figure 37.

When comparing finished cells and wafers of different thicknesses, the stiffness and fracture values of the thinner cells are more scattered. This is shown in figure 38. The fracture stresses of the cells of different thicknesses are alike, whereas the fracture stresses of the wafers vary for different thicknesses. The fracture stresses are presented in table 12. For the values of the wafers, only the “after ECN Clean” wafers from block 3 are included.

		experimental fracture stress (MPa)	standard deviation (MPa)
wafers	120 micron	<b>108</b>	<b>7.11</b>
	160 micron	<b>88</b>	<b>6.58</b>
	200 micron	<b>129</b>	<b>17.72</b>
<hr/>			
cells	120 micron	<b>67</b>	<b>10.85</b>
	160 micron	<b>59</b>	<b>4.80</b>
	200 micron	<b>73</b>	<b>8.21</b>

Table 12. Values of the experimental fracture stress for 200, 160 and 120 micron wafers and cells

Interesting to see is the actual force displacement curve of the soldered specimens. These all show a slight peak in the beginning of the curve (see figure 39). While the acoustic measurements show no difference between soldered and unsoldered specimen.

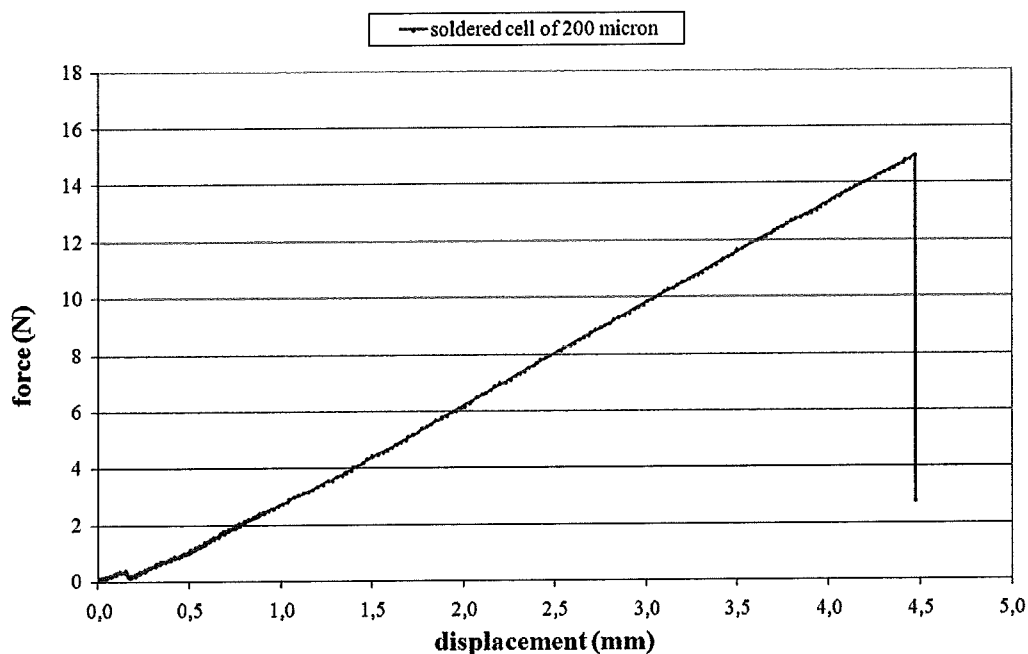


Figure 39. Force displacement plot of the four point bending of a soldered cell of 200 micron. It displays a specific peak in the beginning of the plot. The line drops completely after fracture.

## 8.2 Acoustic emission

During the four point bending experiments, acoustic emission measurements were made. The soldering of samples was also monitored by acoustic emission. Details about the experimental set-up can be found in section 7.2.

### 8.2.1 Four point bending

The fracture of the wafer occurs at approximately 480 seconds after the recording started, this can be seen in figure 40. As mentioned in the previous chapter on AE, brittle fracture is visible in AE by a peak in energy (or in this case amplitude).

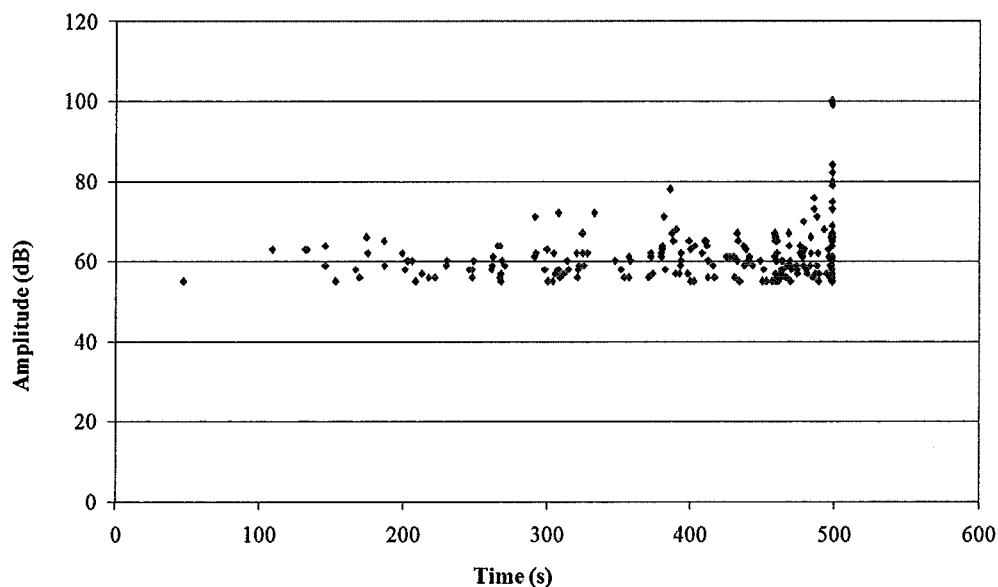


Figure 40. AE results for a four point bending test; fracture occurred at the final peak.

Taking this observation into account, one could argue that some crack propagation might also occur at 410 seconds. At the moment of fracture in all cases (different processing steps and different wafer thicknesses) a steep peak of about 100 dB is visible in the AE amplitude plot.

### 8.2.2 Soldering

In the signal produced by the soldering often two peaks per solder point can be identified. These peaks occur simultaneously with the heating up and cooling down of the solder tip (and the solder point). This signal is shown in figure 41. The results of the soldering experiment are very variable, but this variation is present for all the cell thicknesses.

During the soldering process on the copper plate, AE-signals between 60 and 80 dB (even up to 100) appeared, when either the plate, the tab or the solder machine moved.

As the experiments are done manually, these movements are less controlled than during the automated soldering of the cells.

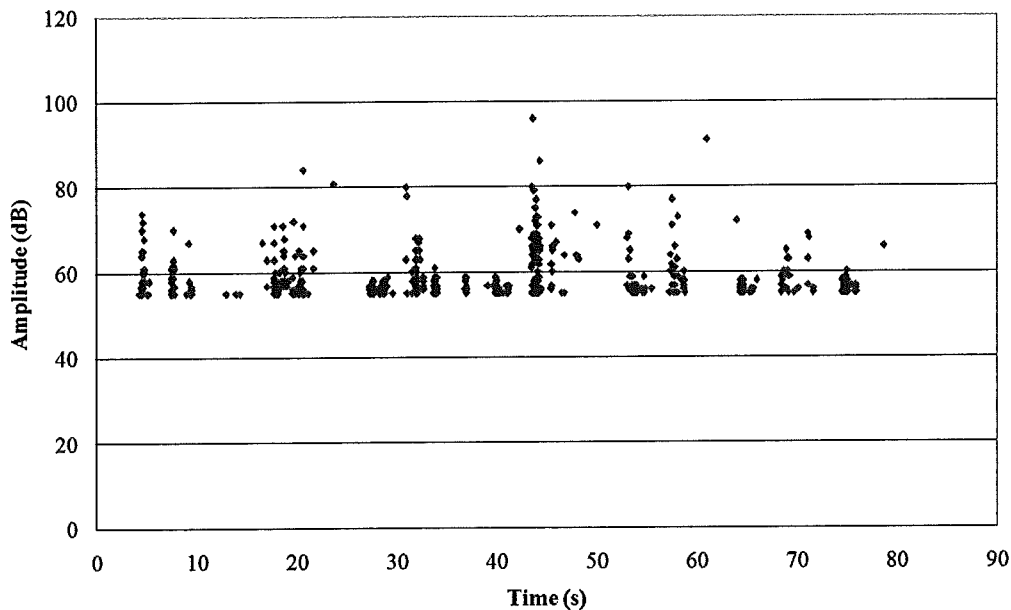


Figure 41. AE results for a series of seven solder points, no fracture occurred.

An interesting observation was that for quite a few (but definitely not all) cells the third and/or fourth solder point of the first tab on the top side of the cell gave a noise. This noise did not occur at the pressing down of the solder tip, but after the initial heat increase of this tip.

The soldering sequence described in chapter 3 is used on all the solder samples, except the first one. In this method the bending of the cells increases slightly during soldering of the first two tabs. The bending is decreased by soldering the last two tabs, but the cell remains in the same buckling mode. To see if a different sequence would have a significant effect, the sequence was changed for one cell. The buckling mode of the cell to changed from a bendt to saddle shaped.

### 8.3 Fractures

A difference in fracture behaviour was observed between different processing steps (the observation is the same for different thicknesses). Cells without the metallisation fracture in a large number of pieces with rough edges, those with metallisation break in two to four pieces.

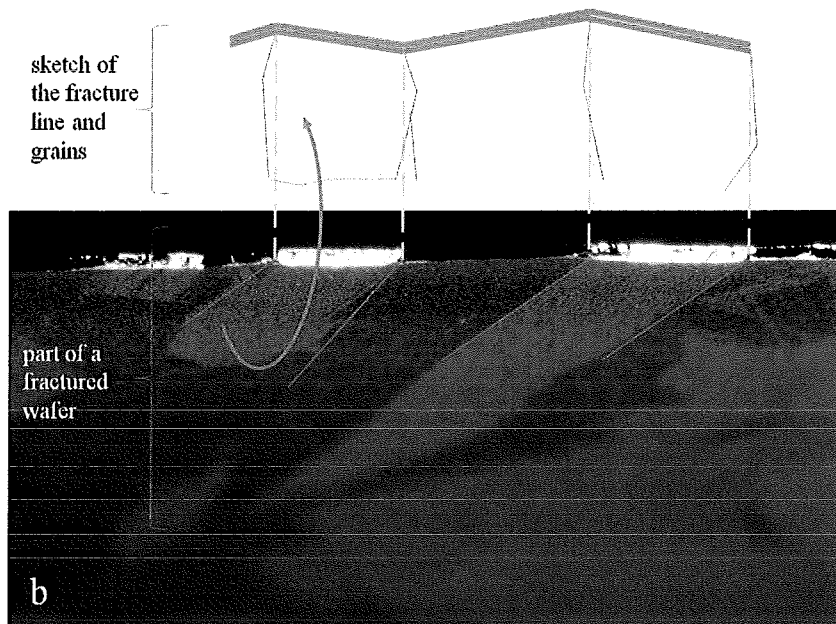
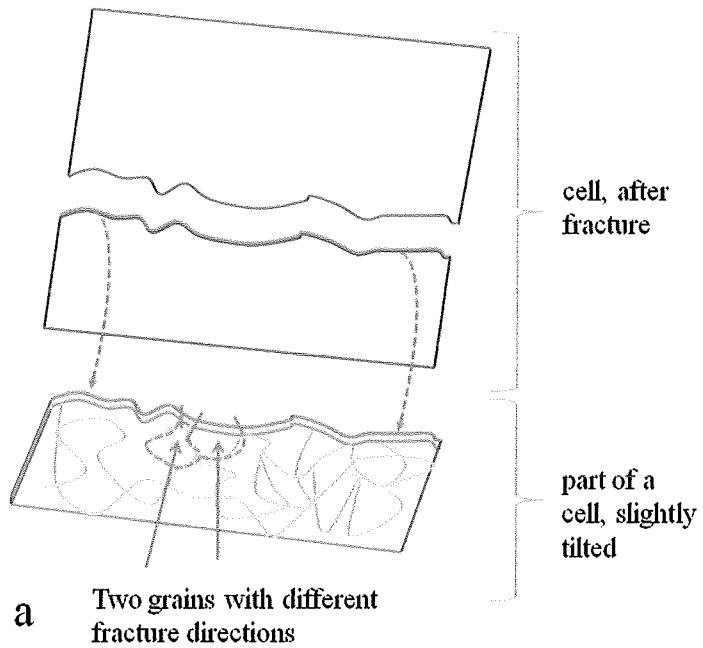


Figure 42 a, b. a) Sketch of the fractured cell and the approximate angle at which the optical microscopy picture was taken. b) Optical photograph and sketches of the fracture surface as it varies with the grain structure, wafer thickness is 200 micron.

The direction of the cracks was roughly parallel to the bending rods. The direction of the fracture alters slightly when a grain boundary is encountered. This can be seen in

figure 42, the fracture surfaces in a different direction in each grain, but steady throughout that particular grain.

The mono-crystalline wafers break in many fragments, which are rather equi-axed. For these wafers, the macro direction of the cracks seems to be parallel to the rods as well. At a smaller scale, the direction could be defined as a zigzag pattern. The zigzag is at the top of the wafer (the compressive side), the bottom surface shows a much smoother line. This can be seen in figure 43.

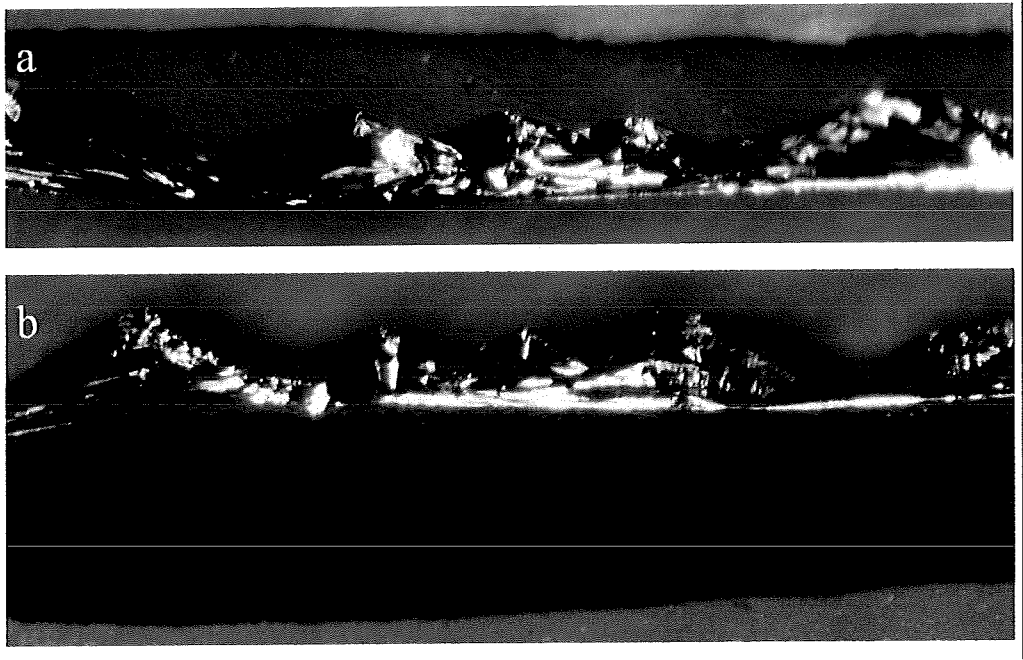


Figure 43 a and b. Optical photographs of the fracture surface of mono-crystalline wafers (of 300 micron)

The SEM pictures, figure 45 and 46, show relatively smooth surfaces, except where the fracture surface crosses a grain boundary. These results will be discussed in section 8.4.

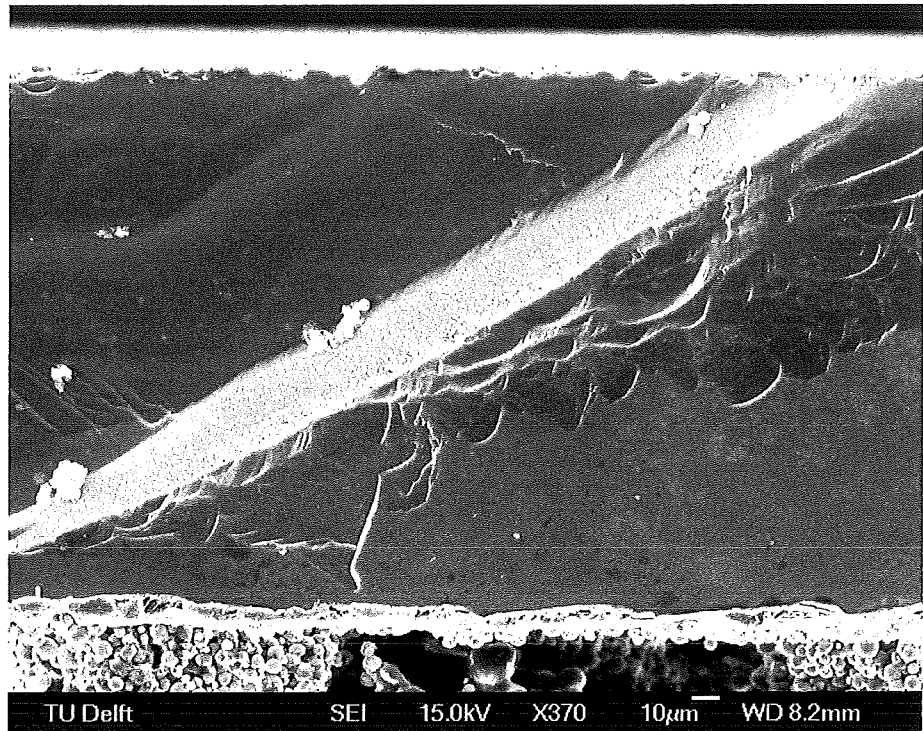


Figure 44. SEM image of a fracture surface at a grain boundary.

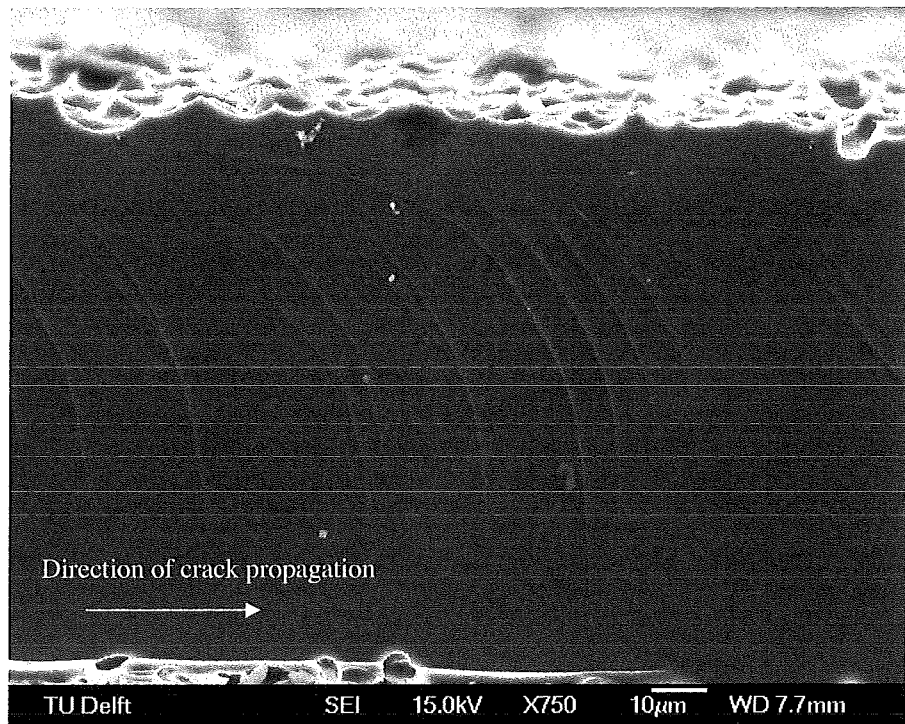


Figure 45. SEM image of a smooth fracture surface, the surface does show some lines due to the propagation of the crack.

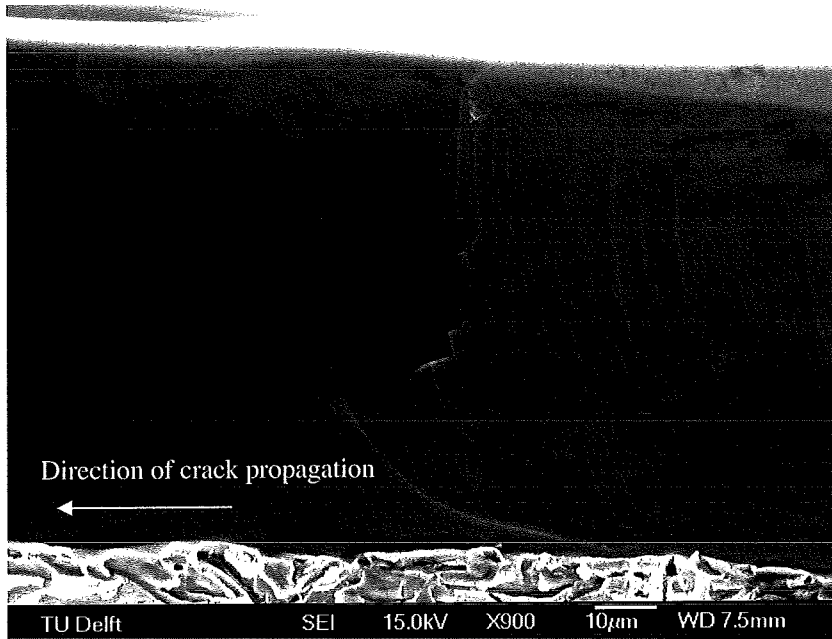


Figure 46. SEM image of a smooth fracture surface, the surface does show some lines due to the propagation of the crack.

On the smooth fracture surfaces, lines can be seen by both optical microscopy and by SEM. The lines on the fracture surfaces are curved, this curvature changes along the surface. On one side the curvature is as shown in figure 45, the other curvature is shown in figure 46.

The change in the direction of the radius can be traced back to a point shown in figure 47, This suggests that this point is the origin of the fracture. This point of origin is located at the transition of aluminium to silver at the underside of the solar cell. Until this point the aluminium was considered to fully cover the surface of the silicon, for soldering purposes the aluminium is locally replaced by silver.

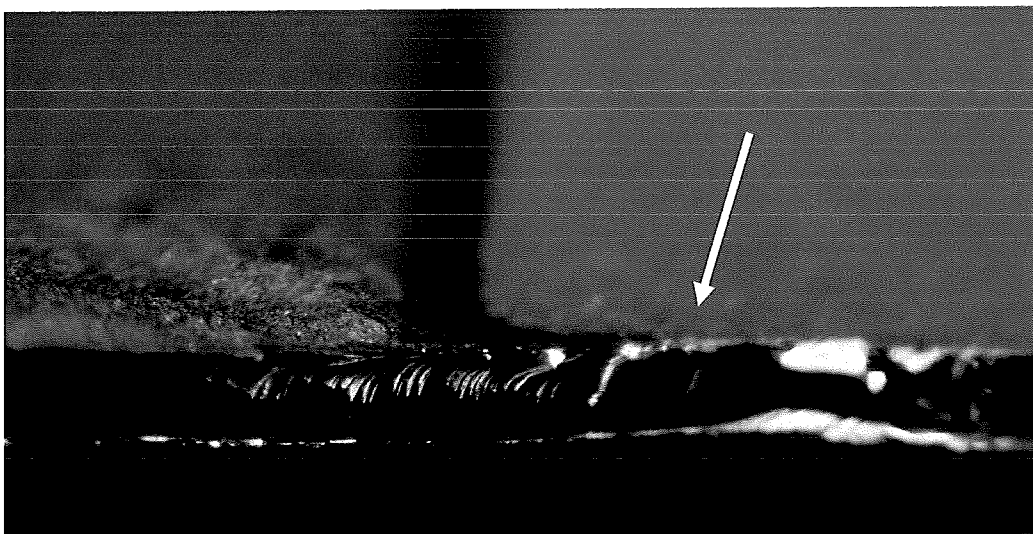


Figure 47. Photograph of the region of fracture initiation.

## 8.4 Discussion

### *Four point bending*

The variation of stiffness of the 120 micron cells can be attributed to the error in the approximations in stress and strain due to the thickness of the materials. For these cells the thickness of the silicon was not determined by weight as it was for the “after ECN Clean” wafers. The average thickness of the wafers was used to estimate the thickness of the cells. More severe bending occurs with thinner cells, the high degree of bending gives a greater error in the stress strain calculations. Corrections might be necessary for quantitative values. However, the results are of the same order of magnitude, so without correction they are also comparable, as the shift between process steps follows the same direction for all three groups of different thickness.

The critical stress for this roughness was calculated to be 229 MPa if a single edge notched plate geometry<sup>54</sup> is assumed. The ratio between the wafers and the surface roughness is small. Because of this small ratio, the critical stress is the same for wafers of different thickness. Experimental results show that this is not the case. Actual, the fracture stress is lowest for the 160 micron wafers. A reason for this could be the quality of the silicon, as all three thicknesses came from different producers. The 160 was of a lesser quality, but the 120 and 200 were of similar quality. So this still indicated that the fracture stress for the 120 micron wafer is less. As fracture toughness is a material property, this should not be the case. A slight difference in silicon quality or the surface properties of the 120 micron, could explain this difference. The values is based on the fracture toughness given by Hull<sup>32</sup>, this is much higher than the fracture stress that is given by the same author. The experimental fracture stresses are in between those given by Hull and those calculated by fracture mechanics.

### *Fracture*

As the material fractures, it takes the path of least resistance, this is likely to be a preferred crystallographic direction. This explains the zigzag fractures that are observed for the mono-crystalline wafers. Also the change in fracture direction that occurs at the grain boundaries is dependent on the crystallographic orientation of the grains. The fractures will have a preferred direction with respect to the crystal orientation. Most likely this will be along a low energy surface, the (111) or (110) planes (as explained in section 6.5).

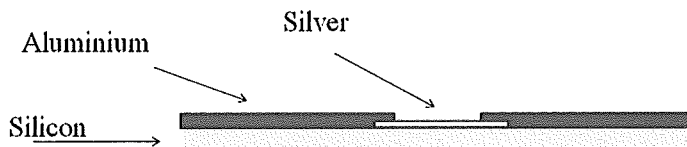


Figure 48. Sketch of the silver aluminium overlap that occurs at the rear side of the cell.

The location of the initiation of fracture is comprehensible, because of the four point bending set up and the sample geometry. The set up creates a large region with a similar stress state. Unfortunately the bending is beyond that of traditional plate theory. The area which is most influenced by the excessive bending is likely to be at

the centre of the plate, this could result in a larger stress for this area. Also the bottom layer (of aluminium) is not a full layer, but an overlap of the silver and the aluminium is present, which causes a localisation of the stress at the bottom of the cell. A detail of the overlap is shown in figure 48.

The place where these two “weaknesses” meet is an obvious place for fracture to occur. To predict the location of fracture during the use of the solar cell, this might not be the weakest point. The four point bending experiment is not representative because such bending does not occur during use.

The preferred atomic planes of fracture are interesting for molecular dynamics modelling, but not so relevant for the production procedure of these solar cells. Perhaps the orientation of mono crystalline wafers can be chosen for optimal strength. For the modelling of multi-crystalline silicon wafers, the directions of the grains (as they form in the casting process) should be known. Using an electron backscattered diffraction (EBSD) map, orientations can be measured. The EBSD technique is used in combination with a scanning electron microscope. The acquisition of an EBSD image is generally based on a CCD (Charge Coupled Device) camera with an image processing system. A diffraction pattern from a point can be obtained by focusing an electron beam on that area of the specimen. A series of patterns is acquired by moving the beam over a stationary specimen (beam scanning) or moving the specimen while keeping the beam stationary (stage scanning). With this technique both line scans and area scans can be made, in order to detect grains (and their orientation).<sup>65</sup> Unfortunately EBSD is beyond the scope of this preliminary research. In the future this technique could be used to examine the crystallographic directions of the fractures as well as the grain orientations.

### *Soldering*

The soldering process did not fracture any of the samples, which was contrary to expectations. The metallisation process could have functioned as a natural selection method, eliminating the cells that had small flaws due to cutting or other processes and transport steps. Another explanation could be that the stresses of heating cause local relaxation (both the silver and aluminium are in tensile stress and the silicon in compressive stress). During cooling down the metal layers have room available to deform, perhaps changing the porosity of the metal layers.

The layers could also have a strong influence on the performance of the total device. The temperature cycles to which a solar panel is exposed during 30 years, should not cause fatigue in brittle materials. The glass and the silicon that are used should be unaffected by these cycles, but the metallisation and the tabs might be affected by fatigue. This means that the stress state of the entire structure can alter during the lifetime of this product.

### *Acoustic emission*

The acoustic emission signals can be caused by so many movements in a material, like the thermal expansion of the solder tip, expansion of the cell or parts of the cell, twinning of the tin solder and friction with the material that is supporting the cell. Because of this it is not possible to determine the origin of the signal with complete certainty. Elimination of possible causes is the surest way to identify the origin of the signal. For this reason the soldering experiment without the tabs, and the experiment

with a copper plate instead of a solar cell are interesting, as no signal appears due to the heating of the tin. The signals suggest that the high peaks start in the cell. The shape of the signal does not allow for the exclusion of crack formation. Verification that these cracks indeed exist near the solder points is extremely difficult. Acoustic techniques are most certainly suitable to study the cells, as they emit signals. Specific frequencies could be associated with the cracking, but the crystallographic direction of the crack could be of importance. Experiments attempting to prove the event of cracking through acoustic techniques should take grain orientations (or cell orientations for single crystal wafers) into account. Because of the complicated interpretation of the acoustic signal, knowledge of both AE and crystallography is compulsory. Methods based on the removal of extremely thin layers, like ion bombardment, should have a minimal influence on the propagation of possible cracks, and still make observation possible.

## **Chapter 9 Discussion and conclusions**

### **9.1 Discussion**

The research questions presented in section 2.2 are divided into three groups, concerning solar cell properties, processing step influences and cell fracture. The following discussion relates closely to the research questions, but the order is different from that listed in section 2.2. The focus points are highlighted before discussing the results of the research.

Firstly, "cell properties" are considered. These are concerned with the general physical condition of the cells through the different process steps, including the mechanical properties of the layers and the survival rates during the production of the cells.

The second group concerns "process influences" which focus on the critical steps in the production process. Factors that limit the success of soldering, such as the degree of bowing and the wafer thickness, are addressed.

Finally, the mechanical "fracture" failure of cells is considered. Relevant questions relate to the presence, origin and mechanisms of fracture.

Because all these questions are interrelated the following discussion first considers the presence, initiation and propagation of cracks in relation to acoustic measurements, fracture experiments and the soldering process. This is followed by a consideration of the influence of process steps during cell production, including heat input, bowing and soldering. Stress measuring techniques are also discussed in this section.

#### **9.1.1 Soldering & cells**

Surface cracks have not been observed using either optical or scanning electron microscopy. One of the concepts presented in this work is the existence of microcracks beneath the solder point. The current idea is that these cracks only occur when both a mechanical and thermal input are present. The possibility of cracks is considered because the shape of the acoustic signal during soldering is similar to the signal associated with cracking. However, the presence of cracks has not been proven by direct observations. Only optical methods were used to evaluate the damage that occurs by heat input alone. Microcracks beneath the tabs cannot be observed by the microscope. Detecting the presence of these cracks is a challenge, as well as detecting those beneath the metallisation layer, even without the tabs connected. Methods based on the removal of extremely thin layers, like ion bombardment, should have a minimal influence on the propagation of possible cracks, and still make observation possible. Heat input alone (by laser) is insufficient to cause any visible fractures. This does not eliminate the possibility that laser soldering is free of microcracking. There could be microcracks below the solder points that were not visible. If AE is used during laser soldering this suspicion could be eliminated.

If the AE signal is indeed coming from microcracks beneath the tabs or metallisation, it only indicates activity. This activity could be the initiation of cracks, but it could also mean that the cracks that are present are growing during the soldering. If the acoustic signals of the four point bending are examined, the signal before fracture shows activity. This activity is scattered, without any distinguishable peaks, nothing that indicates cracks are occurring. Even the acoustic signals of the soldered specimens show no indication of cracks present in the material preceding mechanical failure. This contradicts the expectation that the microcracks, present after soldering, will grow during the four point bending. It could be argued that the peak that occurs for all soldered cells in the force displacement curve indicates a crack. The acoustic signal does not concur with this idea, and another explanation is available. The peak in the force displacement curve can simply occur due to a change in buckling mode. This is likely because the buckling mode of the cells was also changing during the soldering process. When the order of connecting the solder tabs was changed this effect was even more visible.

### ***9.1.2 Influence of metallisation and other process steps***

The steps preceding the soldering were analysed with respect to the degree of bowing and the results of the four point bending tests. Both were used to evaluate the mechanical state of the wafers and cells during the production process. The mechanical influence of the steps preceding the metallisation appears to be negligible. During the metallisation alloying between the silicon and the aluminium rear side occurs. The elemental composition of this alloy is not constant and the mechanical and thermal properties are not known and are difficult to measure.

The stress levels are estimated based on calculations using rough estimates for the properties and presence of the silver and aluminium layers and alloys, which could be an oversimplification. During the soldering process no visible fracture occurred.

The heat input of the soldering process is insufficient to cause visible fracture, but microcracks could be present. Surface cracks have not been observed using either optical and scanning electron microscopy. The soldering process is limited by the deformation that is present, because the machine has to press the cell flat (in a region), with a different arrangement this might not be a problem until the lamination step. As the wafers get thinner the flexibility increases, as does the degree of bowing.

Altering the metallisation pattern seems inevitable for cells thinner than 200 microns. New designs for metallisation on poly-crystalline cells are made every day. The effect of these metallisations on the stress distribution of the cell can be modelled by finite element methods. To verify the models, stress measurements are required. Stress measurements on solar cells are difficult and scans over the entire cells are not possible at the moments (details are presented in section 2.3).

The metallisation can be evaluated if the wafer material is suitable for two dimensional X-ray diffraction. Silicon is not suitable, as is explained in section 2.3.2 and 2.3.4. As verification of the modelling work is still required, the silicon wafer in both the modelling and the physical experiment could be replaced with a wafer of a different material. For this method the wafer should withstand the metallisation and firing process without suffering from excessive bowing. If bowing occurs, the

scanning of the wafer is much more complicated. The wafer can be poly-crystalline if the grains are small and homogenously distributed. Mono-crystalline wafers can also be used, if sufficient diffraction peaks are generated to calculate the Debye rings.

## 9.2 Conclusions

As the wafers become thinner, fewer survive the metallisation process. The losses amounted to 50% for the 120 micron wafers, whereas for the 200 micron wafers, all survived.

### *Process influence*

- Thinner cells have more problems surviving the process steps, some of which were due to the metallisation process, some of which were due to handling. As the wafers get thinner and more bowing occurs the handling problem increases
- The deposition of silicon nitride influences the bowing only slightly, steps preceding this deposition step have not exhibited very little influence. In fact, the mechanical influence of all of these steps is negligible compared to the metallisation. The metallisation largely determines the mechanical state of the cells before soldering. The metallisation introduces the most bending into the cells, this is a measure for the amount of stress in the cells. The strong influence of the metallisation step during production is confirmed by the four point bending experiments.
- The amount of bowing can be estimated reasonably well by a finite element model, including the silver and aluminium pattern, without including the alloying between the layers.
- The order in which the solder tabs are attached to the cell, influences the buckling mode of the cell.

### *Fractures and cracks*

- Surface cracks have not been observed using either optical or scanning electron microscopy.
- Acoustic emission measurements during soldering suggest that after soldering microcracks could exist beneath or close to the solder points. The increased strength and modulus of the soldered cells can be explained by the absence of such cracks in combination with an increase in stiffness due to the additional tab material.
- Fracture of crystalline silicon occurs along preferred crystallographic planes.
- Fracture analysis after four point bending suggest that the transition between aluminium and silver is a weak area in this solar cell design.

## 9.3 Recommendations

### *Research*

The next step in identifying problems concerning the interconnection of solar cells, could well be the confirmation of the presence of microcracks by using other research methods. Atomic force microscopy to examine surface even closer and specifically evaluate the etching around the grains. In addition to locating cracks, the crystallographic orientation of the grains with respect to the loading conditions could be examined.

Determining the actual properties and composition of the silver, the aluminium and the Si-Al layer might shed some light on the alloying that occurs. It could also increase the accuracy of the modelling process.

### *Product design*

Currently new designs for the rear side of solar cells are being developed. The prediction of the mechanical influence of these designs by means of a computer model is simply an extension of the current models. Finding a material that is suited for 2D XRD stress measurements can be useful tool to verify modelling work.

Cells thinner than 200 micron have difficulty in surviving the metallisation step. This is confirmed by thermal shock experiments.<sup>66</sup> To make thinner cells, with this technique, will give problems in line-production set-ups. Adjustments to the cell design could keep the majority of the process steps similar, and create the possibility for thinner cells.

Using the silver grid to reinforce the cell, might be possible, but it largely depends on the mechanical properties of this layer. Another option is to deform the cell, before they enter the firing stage, leaving flat cells after the firing step.

## Acknowledgments

As a newcomer in the solar cell world, Paul de Jong and everyone in the module group of ECN, have received me as a welcome guest. Ian Bennett has encouraged me to pursue all possible measuring techniques that I could think of. Ingrid Romijn has offer assistance through out the enormous task of sample production, as have all the people from the silicon group.

Many people assisted me in trying out ideas. For the XRD measurements and discussions, I would like to thank Amarante Bottger, Niek van de Pers, Stephen Picken, Eduardo Mendes, Rob Delhez, Diederik Ellerbroek and Leo Woning. It was a delight to have so much knowledge and equipment available for my tests.

For the mechanical testing I would like to thank, Coletti, Marcel Hermans and everyone at E&S especially Marcel Bregman and Nico Jan. The acoustic measurements set-up and the high speed camera were explained to me by Marcel Hermans. Marcel Schoorlemmer aided in the interpretation of the acoustic signals. The modelling work was an enormous task, Tim van Amstel has allowed me to take advantage of his modelling skills.

On text editing as well as on a personal level, I have gotten incredible support from Janneke, Heleen and Wouter. Keeping my head on straight during this project was aided by my house (Villa 67), my friends, my family and especially my sister Mieke.

Last but not least, my supervisors deserve special thanks. In my examination of the results and my miserable writing attempts, their spent hours on my work. I want to thank Ian Richardson, Michael Janssen and Ian Bennett again. Their dedication and effort have brought all the little pieces of this work together.

## References

- <sup>1</sup> U.S. department of Energy, 2002. The history of solar. [Online] Available at [http://www1.eere.energy.gov/solar/pdfs/solar\\_timeline.pdf](http://www1.eere.energy.gov/solar/pdfs/solar_timeline.pdf) [accessed on 14 January 2008]
- <sup>2</sup> Goetzberger, A. & Hebling, C., 2000. Photovoltaic materials, past, present and future. *Solar Energy Materials & Solar Cells*, 62(1-2), p.1-19.
- <sup>3</sup> Goetzberger, A., Hebling, C. & Schock, H.W., 2003. Photovoltaic materials, history, status and outlook. *Materials Science and Engineering: R: Reports*, 40(1), p.1-46.
- <sup>4</sup> Solymar, L. & Walsh, D., 2004. *Electrical properties of materials*. 7<sup>th</sup> ed. New York: Oxford University Press.
- <sup>5</sup> Khattak, C.P., Joyce, D.B. & Schmid, F., 2002. Production of low-cost solar grade (SoG) silicon feedstock. *The 29<sup>th</sup> Photovoltaic Specialists Conference*. New Orleans, USA, 19-24 May 2002.
- <sup>6</sup> Coletti, G., Tool, C.J.J. & Geerligs, L.J., 2005. Mechanical strength of silicon wafers and its modelling. In, ECN (Energy research Centre of the Netherlands), *15<sup>th</sup> Workshop on Crystalline Silicon Solar Cells & Modules: Materials and Processes*. Vail Colorado, USA 7-10 August 2005.
- <sup>7</sup> Hooijmans, J.W., 2005. *Crystalclear22, thickness and porosity measurements*. November 2005. [Text document] Petten: Energy research Centre of the Netherlands.
- <sup>8</sup> De Jong, P.C. et al., Low stress interconnections for solar cells. In, ECN (Energy research Centre of the Netherlands), *20<sup>th</sup> European Photovoltaic Solar Energy Conference and Exhibition*. Barcelona, Spain, 6-10 June 2005.
- <sup>9</sup> Dixit, M.S. et al., 1993. *Gas microstrip detectors on resistive plastic substrates*. Nuclear Instruments and Methods in Physics Research Section A, 348 (2-3), p.365-371.
- <sup>10</sup> Honsberg, C. & Bowden, S., 1999. *Photovoltaics: Devices, systems and applications, PVCDROM 1.0*. 1999 [cd-rom] Sydney, Australia: University of New South Wales.
- <sup>11</sup> Weeber, A.W. et al., 2004. *Process specifications ECN mc-Si cell processing ECN-CX 04-119*. October 2004 [report] Petten, The Netherlands: Energy research Centre of the Netherlands.
- <sup>12</sup> Romijn, I., 2007 probable decade. *Temperature stability tests PECVD*. [Text document] Petten: Energy research Centre of the Netherlands.
- <sup>13</sup> Brice, J.C., 1987. Melting point of Si. *Properties of silicon EMIS data reviews series no. 4*. London, UK: INSPEC. p.52
- <sup>14</sup> Rybicki, G.C. & Pirouz, P., 1988. Indentation Plasticity and Fracture in Silicon. *NASA Technical Paper*. 2863, Scientific and technical information division. Cleveland Ohio, USA.
- <sup>15</sup> Schneider, A. et al., Bow reducing factors for thin screen printed MC-Si solar cells with Al BSF. In, ECN (Energy research Centre of the Netherlands), *29<sup>th</sup> Institute of Electrical and Electronics Engineers Photovoltaic Specialists Conference (IEEE PVSC)*. New Orleans, USA 20-24 May 2002.
- <sup>16</sup> Huster, F., Aluminium-back surface field: bow investigation and elimination. *20<sup>th</sup> European Photovoltaic Solar Energy Conference (EPSC)*. Barcelona, Spain 6-10 June 2005.
- <sup>17</sup> Van Mourik, P. & Van Dam, J., 2001. *Materiaalkunde voor ontwerper en constructeurs*. 3<sup>rd</sup> ed. Delft, The Netherlands: VSSD.
- <sup>18</sup> Brandon, D. & Kaplan, W.D., 1999. *Microstructural characterisation of materials*. Chichester, UK: John Wiley & Sons.
- <sup>19</sup> Kouteva-Arguirova, S., Seifert, W., Kittler, M. & Reif, J., 2003. Raman measurement of stress distribution in multicrystalline silicon materials. *Materials Science and Engineering B*, 102(1-3) p.37-42.
- <sup>20</sup> Shillington, E.A.G. & Clarke, D.R., 1999. Spalling failure of a thermal barrier coating associated with aluminium depletion in the bond-coat. *Acta Materialia*, 47(4) p.1297.
- <sup>21</sup> Ma, Q. & Clarke, D.R., 1993. Measurement of residual stresses in sapphire fiber composites using optical fluorescence. *Acta Metallurgica et Materialia*, 41(6) p.1817-1823.
- <sup>22</sup> Ma, Q. & Clarke, D.R., 1993. Stress measurement in single-crystal and polycrystalline ceramics using their optical fluorescence. *Journal of the American Ceramic Society*, 76(6) p1433-1440.
- <sup>23</sup> He, S., Danyluk, S. & Ostapenko, S., 2003. Residual stress characterization for solar cells by infrared polariscopy. *National Center for Photovoltaics (NCPV) and Solar Program Review Meeting*, 24-26 March 2003.
- <sup>24</sup> He, S., 2005. *Near infrared photoelasticity of polycrystalline silicon and it's relation to in-plane residual stresses*. MSc. Georgia Institute of Technology.
- <sup>25</sup> Hoekstra, S.A.I., Groenewegen, J.P.M., Böttger, A.J., 2005. *An introduction to X-ray diffraction: excerpts from elements of x-ray diffraction by B.D. Cullity*. [Leaflet] Delft, The Netherlands: Delft University of Technology.

- <sup>26</sup> He, B.B., 2003. Introduction to two-dimensional X-ray diffraction. *Powder Diffraction*, 18(2) p.71-85.
- <sup>27</sup> Seifarth, H. et al., 1998. Preparation of SiO<sub>2</sub> films with embedded Si nanocrystals by reactive r.f. magnetron sputtering. *Thin Solid Films*, 330(2) p.202-205
- <sup>28</sup> Stein, G.E., Kramer, E.J., Li, X. & Wang, J., 2007. Single-crystal diffraction from two-dimensional block copolymer arrays. *Physical Review Letters*, 98, 086101
- <sup>29</sup> De Wolf, I., 1996. Micro-Raman spectroscopy to study local mechanical stress in silicon integrated circuits. *Semiconductor Science and Technology*, 11 p.139-154.
- <sup>30</sup> Bultman, J.H., 2000. Pin Up Module: A design for higher efficiency, easy module manufacturing and attractive appearance. In, ECN (Energy research Centre of the Netherlands). *16<sup>th</sup> EC Photovoltaic Solar Energy Conference*. Glasgow, UK 1-5 May 2000.
- <sup>31</sup> Noda, N., Hetnarski, R.B. & Tanigawa, Y., 2002. *Thermal stresses*. 2<sup>nd</sup> edition, New York, USA: Taylor and Francis.
- <sup>32</sup> Hull, R., 1999. *Properties of crystalline silicon*. London, UK: INSPEC The institution of Electrical Engineers.
- <sup>33</sup> Callister, W.D., 2000. *Materials Science and Engineering: an Introduction*. 5<sup>th</sup> edition, New York, USA: John Wiley & Sons
- <sup>34</sup> Duerinckx, F. et al., 2004. Improved screen printing process for very thin multicrystalline silicon solar cells. *19<sup>th</sup> European Photovoltaic Solar Energy Conference*. Paris, France 7-11 June 2004
- <sup>35</sup> Van Hoegee, K.J.F.L., 2003. Flower Power Module bij -40°C en +85°C. [text document] ECN-Zon Memo-03-016 December 2003. Petten: Energy research Centre of the Netherlands.
- <sup>36</sup> Benmohamed, Z. & Remram, M., 2006. Effect of Dislocation Density on Multicrystalline Silicon Solar Cells Efficiency. [Online] University of Constantine, Algeria. Available at: [http://www.materialscience.pwr.wroc.pl/ap/articles/ms\\_2006\\_028.pdf](http://www.materialscience.pwr.wroc.pl/ap/articles/ms_2006_028.pdf) [accessed on 2 January 2008]
- <sup>37</sup> Möller, H.J., Funke, C., Rinio, M. & Scholz, S., 2005. Multicrystalline silicon for solar cells. *Thin Solid Films*, 487(1-2) p.179-187.
- <sup>38</sup> Martinuzzi, S. & Stemmer, M., 1994. Mapping of defects and their recombination strength by a light-beam induced current in silicon wafers. *Materials Science and Engineering B, Advanced Functional Solid-State Materials*, 24(1-3) p.152-158.
- <sup>39</sup> Van Malsen, J., 2003. *The effect of reinforcement particles on mechanical properties in metal matrix composites*. [literature report] Delft, The Netherlands: Delft University of Technology.
- <sup>40</sup> J.D. Eshelby, The determination of the elastic field of an ellipsoidal inclusion and related problems, *Proc R Soc London A* 241 (1957), pp. 376-396.
- <sup>41</sup> Clyne, T.W., 1990. A compressibility-based derivation of simple expressions for the transverse Poisson's ratio and shear modulus of an aligned long fibre composite. *Journal of Materials Science Letters*, 9 p336-339.
- <sup>42</sup> Ji, B. & Gao, H., 2006. Elastic properties of nanocomposite structure of bone. *Composites Science and Technology*, 66(9) p1212-1218.
- <sup>43</sup> Carroll, A.F. et al. Advances in PV metallisation technology. *20<sup>th</sup> European Photovoltaic Solar Energy Conference*. Barcelona, Spain 6.-10 June 2005.
- <sup>44</sup> Ventsel, E. & Krauthammer, T., 2001. *Thin plates and shells : theory, analysis, and applications*. New York : Dekker.
- <sup>45</sup> Chu, S.N.G., 1998. Elastic bending of semiconductor wafer revisited and comments on Stoney's Equation. *Journal of Electrochemical Society*, 145(10) p.3621-3627.
- <sup>46</sup> Klein, C.A., 2000. How accurate are Stoney's equation and recent modifications. *Journal of applied physics*, 88(9) p.5487-5489.
- <sup>47</sup> Van Eijk, S., 2006. *An analytical and experimental evaluation of the EPLaR Process for Flexible Displays*. MSc, Delft University of Technology.
- <sup>48</sup> Hauch, J.A., Holland, D., Marder, M.P. & Swinney, H.L., 1999. Dynamic fracture in single crystal silicon. *Physical Review Letters*. 82 p.3823 - 3826.
- <sup>49</sup> Holland, D. & Marder, M., 1998. Ideal brittle fracture of silicon studied with molecular dynamics. *physical review letters*, 80(4) p.746 - 749.
- <sup>50</sup> Broek, K.M., 2005. *Modelling thermal input during soldering, ECN-CX 05-081*. September 2005 [report] Petten, The Netherlands: Energy research Centre of the Netherlands.
- <sup>51</sup> Behnken, H., Apel, M. & Franke, D., 2003. Simulation of mechanical stress during bending tests for crystalline wafers. *3<sup>rd</sup> World Conference on Photovoltaic Energy Conversion*. Osaka, Japan 11-18 May 2003.
- <sup>52</sup> Van Amstel, T., 2007. [Presentation and discussion on modelling] (personal communication 14 August 2007).

- <sup>53</sup> Janssen, M., Zuidema, J. & Wanhill, R.J.H., 2002. *Fracture Mechanics*. 2<sup>nd</sup> edition. Delft, The Netherlands: VSSD.
- <sup>54</sup> Coletti, G., Van Der Borg, N.J.C.M., S. De Iuliis, s., Tool, C.J.J. & Geerligs, L.J., 2005. Mechanical strength of silicon wafers depending on wafer thickness and surface treatment. In ECN (Energy research Centre of the Netherlands), *21st European Photovoltaic Solar Energy Conference and Exhibition*. Dresden, Germany, 4-8 september 2006.
- <sup>55</sup> Wasmer, K. et al, 2005. Cleavage fracture of brittle semiconductors from the nanometre to the centimetre scale. *Advanced Engineering Materials*, 7(5) p.309-317.
- <sup>56</sup> Hirsch, P.B., Booth, A.S., Ellis, M. & Roberts, S.G., 1992. Dislocation-driven stable crack growth by microcleavage in semi-brittle crystals. *Scripta metallurgica et materialia*, 27(12) p.1723-1728.
- <sup>57</sup> Scruby, C.B., 1987. An introduction to acoustic emission. *Journal of Physics E - Scientific Instruments*, 20 p.945-953.
- <sup>58</sup> Niklas, A., Froyen, L., Wevers, M. & Delaey, L., 1995. Acoustic emission during fatigue crack propagation in SiC particle reinforced Al matrix composites. *Metallurgical and materials transactions A*, 26(A) p.3183-3189.
- <sup>59</sup> Schoorlemmer, H., 2007. [Discussion on acoustic emission and acoustic emission software] (personal communication 20 June 2007).
- <sup>60</sup> Surgeon, M. & Wevers, M., 1999. Modal analysis of acoustic emission signals from CRFP laminates. *NDT&E International (NonDestructive Testing and Evaluation International)*, 32 p311-322.
- <sup>61</sup> M. Gabor A.M. et al, 2006. Soldering induced damage to thin Si solar cells and detection of cracked cells in modules. *21<sup>st</sup> European Photovoltaic Solar Energy Conference*. Dresden, Germany 4-8 September 2006.
- <sup>62</sup> Pérez, R. & Gumbsch, P., 2000. Directional Anisotropy in the Cleavage Fracture of Silicon. *Physical Review Letters*, 84(23) p.5347 – 5350.
- <sup>63</sup> Wilson, C. J., Ormeggi, A. & Narbutovskih, M., 1996. Fracture testing of silicon microcantilever beams. *Journal of Applied Physics*, 79(5) p.2386-2393.
- <sup>64</sup> Kawamura, R., Sasatani, K., Onizuka, T., & Kaneko, K., 1994. Operation and crystalline properties of electro-magnetic casting. *24<sup>th</sup> Institute of Electrical and Electronics Engineers Photovoltaic Specialists Conference*. Waikoloa, USA 5-9 December 1994.
- <sup>65</sup> F.J. Humphreys, F.J., 1998. Quantitative metallography by electron backscattered diffraction, *Journal of Microscopy*, 195(3) p.170-185.
- <sup>66</sup> Sopori B. et al., 2007. Studies on fundamental mechanisms in a fire-through contact metallization of Si solar cells. *22<sup>nd</sup> European Photovoltaic Solar Energy Conference*. Milan, Italy 3-7 September 2007

## Appendix I

Because of the temperature changes during the metallisation, a table was made for the values of stress and the presence of plastic strain, determined for specific temperature levels.

For aluminium this was:

Yield stress (MPa)	Plastic strain included	Temperature (°C)
40	no	25
60	yes	25
20	no	450
40	yes	450

For silver this was:

Yield stress (MPa)	Plastic strain included	Temperature (°C)
60	no	25
130	yes	25
18	no	900
70	yes	900

These values are used in the finite element model of the metallisation process, along with other data. The data and the set-up of the model are presented in section 4.2.

